CELLULAR AND NETWORK MECHANISMS FOR GENERATING INHIBITION IN THE MOUSE DORSAL COCHLEAR NUCLEUS

By

Pierre F. Apostolides

A DISSERTATION

Presented to the Vollum Institute Neuroscience Graduate Program and the Oregon Health & Science University School of Medicine in partial fulfillment of the requirements for the degree of Doctor of Philosophy

December 2013

School of Medicine

Oregon Health & Science University

CERTIFICATE OF APPROVAL

This is to certify that the Ph.D. dissertation of

PIERRE APOSTOLIDES

has been approved on December 13th, 2013

Advisor, Laurence Trussell, PhD

Member and Chair, Craig Jahr, PhD

Member, John Williams, PhD

Member, Eric Gouaux, PhD

Member, William Taylor, PhD

TABLE OF CONTENTS

ACKNOWLEDGEMENTS

First and foremost I thank Larry Trussell. It is thanks to him that these projects were possible in the first place. Larry taught me everything I know about science. Furthermore, he always stressed to think "outside the synapse" and constantly pushed me out of my comfort zone, emphasizing the greater implications of scientific results with regards to physiological function and ultimately, sensory perception.

Thank you to my former labmates Kevin Bender, Sidney Kuo and Michael Roberts, who were always there to lend a helping hand, and for their extreme patience as I traversed through the confusing (and sometimes frustrating) world of patch-clamp electrophysiology. I thank current lab members Carolina Borges-Merjane, Hai Huang, Hsin-Wei Lu, Jeffrey Tang, Marie Wang, and Daniel Yaeger for their support, advice, and important feedback on the work presented here. Furthermore, thank you to Michael Bateschell and Ruby Larisch: "Amazing technical assistance" is an understatement. I am also indebted to Dr. Roger Nicoll for offering me a job as a lab tech in 2006: This experience introduced me to cellular neurophysiology and directly resulted in my desire to apply to grad school and study synaptic transmission.

I thank the current and former members of my thesis commitee: Matthew Frerking, Eric Gouaux, Craig Jahr, Patrick Roberts, Rowland Taylor and John Williams for their questions, comments, and unconditionally good-natured concern for the direction of my work.

Thank you to my friends Tirdad Chaharlengi, Bryan Manning, and Karen Tran for providing almost daily entertainment and laughs over the past five years, as well as moral support through the hardest times. Finally I thank my parents, Jean-Marie Apostolidès and Danielle Trudeau, for encouraging me to pursue my interest in science, and never once telling me "be realistic, you can't do that." They were truly role models for me in that respect, as they followed their interests and passions.

This thesis is dedicated to my grand-parents, Jeannine Dumouchel & Yvon Trudeau; Geneviève Mazeron & Dr. Paul Apostolidès.

ABSTRACT

Sensory information is the basis of an integrated perception of reality and allows an organism to make informed decisions based upon events occurring in its surroundings. Mammals are equipped with five sensory modalities to sample the physical and chemical phenomena of the outside world. However, the cellular mechanisms underlying basic sensory processing in the brain are poorly understood. Particularly, an outstanding question is how do heterogeneous groups of cells, e.g. neuronal microcircuits, function in concert to extract and relay meaningful information about sensory inputs? This thesis focuses on a mammalian auditory brainstem region known as the dorsal cochlear nucleus (DCN). Using whole-cell patch clamp electrophysiology and multi-photon imaging in acute brain slices from mouse DCN, the experiments herein focus on inhibition mediated by the neurotransmitters glycine and GABA. Chapter 1 addresses outstanding issues related to the molecular mechanisms involved in the packaging of inhibitory neurotransmitters into synaptic vesicles. Chapters 2-4 focus on the synaptic inputs that control the activity of a previously unstudied inhibitory interneuron in the DCN, the superficial stellate cell. In particular, Chapter 3 describes a novel pathway in the DCN microcircuit that allows excitatory projection neurons to control the activity of stellate cells via gap junction (electrical) coupling. Chapter 4 demonstrates that synaptic inhibition in stellate cells is mediated not only by glycine and GABA, but can be mediated by synaptically-released glutamate deactivating a resting cation conductance in the dendrites of electrically-coupled neurons. These findings are discussed in the context of auditory perception and current theories regarding neuronal microcircuits.

INTRODUCTION

Sound information is processed by parallel pathways in the brain.

Deflections in sound pressure, which form the physical basis of auditory stimuli, are transformed into electrical impulses in the ear via a tonotopically-organized array of mechanosensitive inner hair cells (Gillespie and Müller, 2009). This "labeled-line" organization divides harmonically-rich acoustic stimuli into distinct frequency bands, with the amplitude of each band encoded as a graded change in glutamate release from the hair cell onto spiral ganglion neurons (Glowatzki et al., 2008). Auditory information is subsequently relayed to the brain via excitatory auditory nerve fibers (8^{th} cranial nerve) arising from the spiral ganglia, thereby maintaining the tonotopic organization of the inner ear in the efferent projections to the brain.

A key aspect of the central auditory system is that sound information is funneled through parallel neural pathways specialized in extracting distinct components of auditory stimuli, while nevertheless maintaining a tonotopic organization across distinct neuronal populations (Kandler et al., 2009). This division of auditory information into parallel streams occurs at the initial stages of auditory processing, where auditory nerve fibers terminate in two specific brain regions: The ipsilateral dorsal and ventral cochlear nuclei (Oertel and Young, 2004; Kandler et al., 2009). A tonotopic organization is established because the principal neurons of these nuclei receive excitatory synapses from a limited number of isofrequency auditory nerve fibers, thus restricting the auditory response properties of any given neuron to a narrow frequency range.

Cellular anatomy of the DCN microcircuit

Whereas neurons of the ventral cochlear nucleus are specialized to extract distinct features of acoustic stimuli, the dorsal cochlear nucleus (DCN) is unique in the auditory brainstem in that its principal efferent neurons (fusiform/giant cells) integrate excitatory inputs from auditory and non-auditory sources (Oertel and Young, 2004). Furthermore, the large number of inhibitory interneurons in the DCN, e.g. cells that project their axons locally, suggests that this circuit is involved in more than simply relaying information from the ear to higher order brain regions.

The DCN circuit is typically divided into three distinct layers: molecular, cell body, and deep layers (Figure 1). Glutamatergic auditory nerve fibers course through the deep layer and synapse on the basal dendrites of fusiform cells as well as glycinergic interneurons termed vertical cells. Non-auditory information from proprioceptive, vestibular, and higher-order brain areas (Shore and Zhou, 2006) enters via a cerebellum-like system of excitatory mossy fibers that innervate local granule cells (Oertel and Young, 2004; Bell et al., 2008). The granule cells subsequently project

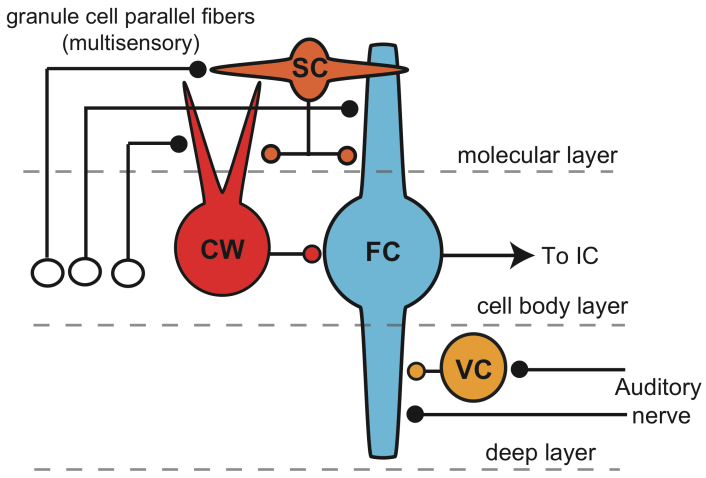

Figure 1: Simplified diagram of the DCN circuit. The principal output neurons (fusiform cells; FC) integrate auditory nerve input with multisensory input from a cerebellum-like system of granule cell parallel fibers. In addition, the auditory pathway recruits inhibitory vertical cells (VC), whereas the multisensory pathway contacts cartwheel (CW) and stellate (SC) cell interneurons. However, no interneuron integrates auditory and multisensory input, suggesting that the two pathways are processed independently.

glutamatergic parallel fiber axons through the molecular layer and synapse on the apical dendrites of fusiform cells. Parallel fibers also excite two types of inhibitory interneurons: Cartwheel cells, which provide strong, mixed glycinergic/GABAergic inhibition to fusiform and other cartwheel cells, and stellate cells which are thought to release GABA and inhibit the distal dendrites of fusiform and cartwheel cells. Thus, auditory and non-auditory inputs are integrated at the level of fusiform cells, and each pathway recruits non-overlapping sets of inhibitory interneurons.

Function of the DCN in sound localization.

The specific role of the DCN in auditory perception is poorly understood. Electrolytic lesions of the DCN or the dorsal acoustic stria do not seem to interfere with sound *perception*, but instead cause subtle deficits in sound *localization* in the vertical plane (May, 2000). These data, along with anatomical studies showing that DCN neurons integrate auditory and non-auditory information, suggest that the DCN may compute information regarding the location of a sound source relative to the animal's body position (Oertel and Young, 2004; Bell et al., 2008; Requarth and Sawtell, 2011). In agreement with a significant non-auditory input to the DCN, fusiform cells recorded *in vivo* respond to auditory and somatosensory stimuli (Young et al., 1995) and somatosensory stimuli can modify the auditory response properties of fusiform cells (Shore, 2005; Koehler et al., 2011).

What is the functional significance of the DCN's integration of somatosensory and auditory signals, and why does this integration occur at the earliest stages of central

auditory processing? One prominent hypothesis is that the DCN is involved in detecting notches in the frequency spectrum of harmonically rich sounds (Reiss and Young, 2005). Spectral notch detection is important because the outer ear creates distortions in auditory stimuli characterized by a gain reduction in a specific frequency band (e.g., the head-related transfer function, Hebrank and Wright, 1974). The central frequency of this pinna-based notch filtering changes depending on the location of the sound source, and previous studies suggest that the frequency of the spectral notch provides a cue for detecting the vertical location of a sound source (Middlebrooks, 1992; May, 2000). In agreement with a role for the DCN in spectral notch detection, fusiform cells recorded in cats respond best to harmonically-rich sounds where the rising edge of a spectral notch is positioned near that cell's characteristic frequency (Reiss and Young, 2005). These data, along with the previously mentioned lesion studies (May, 2000), suggest that the DCN may play a role in detecting the elevation of a sound source (Oertel and Young, 2004). Thus, the prominent somatosensory input to the DCN could provide necessary cues as to the location of the animal's head during incoming auditory stimuli.

Local inhibition controls the response properties of DCN fusiform cells.

Regardless of the precise role of the DCN in auditory perception, previous studies demonstrate that inhibitory interneurons determine the response properties of fusiform cells *in vivo*. Single unit recordings show that many fusiform cells display non-linear tuning curves in response to sound: The prototypical response of fusiform cells recorded in unanaesthetized cats (Type IV responses) displays characteristic frequency tuning,

whereby specific frequencies increase the neuron's firing rate as a function of sound amplitude (Spirou and Young, 1991; Davis and Young, 2000). However, increasing the amplitude beyond a certain point typically causes inhibitory responses (reduction in spontaneous firing), and sounds tuned above or below the characteristic frequency similarly decrease spontaneous firing rate at most amplitudes (Davis and Young, 2000). Thus, fusiform cells, at least in cats, are characterized by frequency *and* amplitude-tuning. Interestingly, pharmacological block of glycine receptors broadens the tuning curve of fusiform cells, implying that local glycinergic inhibition shapes the inhibitory sidebands. On the contrary, blocking $GABA_A$ receptors actually sharpens the tuning curves, suggestive of a GABAergic inhibition of glycinergic interneurons (Davis and Young, 2000).

Downregulation of local inhibition in the DCN may play a role in tinnitus.

Tinnitus is a condition defined by a pervasive ringing in the ears in absence of auditory stimuli. This phantom percept of sound affects between 8-20% of people over age 60 but can be induced in individuals of any age, particularly after traumatic exposure to loud noises (Roberts et al., 2010). Although tinnitus is not life threatening, it can have a significant effect on the quality of life and may be co-morbid with depression (Kaltenbach, 2006a).

Converging lines of evidence suggest that tinnitus may be mediated by hyperactivity in the central auditory system, particularly in the DCN (Kaltenbach, 2006b). Specifically, denervation of the auditory nerve does not abolish tinnitus in most cases (Berliner et al.,

1992), suggesting a central locus for the expression of tinnitus percepts. Furthermore, the pitch and amplitude of tinnitus are modulated by head orientation and muscle movements (particularly jaw and neck muscles; Cherian et al., 2013). Given that the DCN is the first brain region in the auditory pathway that integrates auditory and somatosensory information, recent studies have focused on maladaptive plasticity in the DCN circuit as a potential basis for tinnitus (Brozoski et al., 2002; Kaltenbach, 2006a; Kaltenbach, 2006b; Roberts et al., 2010; Middleton et al., 2011). Particularly, evidence shows that fusiform cells become hyperactive in animal models of tinnitus, and that this may be partially due to a downregulation of inhibitory transmission (Brozoski et al., 2002; Wang et al., 2011). Furthermore, a recent study showed that the DCN hyperactivity associated with behavioral expression of tinnitus in mice is due to a specific reduction in feedforward GABAergic inhibition in the parallel fiber pathway (Middleton et al., 2011). Taken together with the *in vivo* data showing that local inhibition controls the response properties of DCN neurons (Davis and Young, 2000), these studies converge upon the idea that local inhibitory circuits tightly control the excitability of fusiform cells, and that pathological hyperactivity of fusiform cells, due to downregulation of GABAergic and/or glycinergic inhibition, may underlie certain aspects of tinnitus (Kaltenbach, 2006b; Roberts et al., 2010; Wang et al., 2011). Thus, identifying the mechanisms that generate local inhibition in the DCN may drive the development of novel treatments for tinnitus.

Vesicular packaging and synaptic release of inhibitory neurotransmitters

Although it is accepted that synaptic inhibition is crucial for shaping the response properties of auditory neurons in the DCN and beyond, the cellular mechanisms that determine the strength of inhibitory synapses remain poorly understood. Fast inhibitory transmission in the nervous system is mediated by the release of glycine and GABA. Interestingly, both neurotransmitters are packaged into synaptic vesicles by the same vesicular transporter (VGAT), and thus can be co-released from the same vesicles (Jonas et al., 1998; Wojcik et al., 2006; Lu et al., 2008). However, the mechanisms controlling the rate of refilling, as well as the amount of glycine or GABA inside presynaptic vesicles remain unclear. Understanding these features of synaptic transmission is important, as previous studies show that the amount of neurotransmitter inside synaptic vesicles is a key determinant of synaptic strength (Edwards, 2007). Thus, the experiments in Chapter 1 were designed to answer the following questions.

1) How fast can synaptic vesicles re-equilibrate upon acute changes in cytosolic transmitter availability? Do synaptic vesicles retain their transmitter content after filling, or do vesicles leak neurotransmitter independently of exocytosis?

2) What molecules at presynaptic terminals are responsible for generating the neurotransmitter available for uptake into synaptic vesicles?

3) What is the concentration of free neurotransmitter inside the presynaptic cytosol?

We approached these issues by recording from synaptically-coupled pairs of cartwheel interneurons in acute DCN brain slices. We found that 1) Synaptic vesicles are not static after refilling. Instead, synaptic vesicle content can be bi-directionally regulated

independently of exocytosis. 2) The plasma membrane transporter GlyT2 and the intracellular enzyme glutamate decarboxylase are the main determinants of the moment-to-moment supply of glycine and GABA, respectively. 3) The effective concentration of cytosolic glycine or GABA available for uptake into synaptic vesicles is 5 to 7 mM. The results of Chapter 1 show that vesicular transmitter content is labile and can be regulated on a minutes time-scale, and suggest that cytosolic transmitter availability represents a key locus for the control of inhibitory synaptic strength.

Adaptive filtering in cerebellum-like structures.

A conundrum regarding sensory perception is that an animal must differentiate between sensory stimuli that are generated by its own behavior and those that originate from the outside world; the nervous system of all creatures must therefore be equipped with mechanisms to adaptively filter self-generated or irrelevant sensory input (Bell et al., 2008; Requarth and Sawtell, 2011). A canonical example of such adaptive filtering comes from studies in weakly electric fish (*mormyrid* and other species). These fish recognize objects in their environment by generating an electric field and sensing the perturbations caused by nearby objects. However, the electroreceptors on the fish's skin do not differentiate between electric field perturbations generated by the fish's own movement versus that of extrinsic objects, and movements of the fish's tail can cause fluctuations in the electric field that are much larger than those caused by ethologically-relevant stimuli (Bell et al., 2008). Thus, the fish's nervous system must be equipped with mechanisms to cancel out the electric field perturbations arising from self-generated movement. To this

end, the efferent neurons in the electrosensory lobe (ELL) integrate two types of excitatory synapses from different sensory modalities: An "instructive" input carrying information about the activity of electroreceptors on the skin, and a "predictive" input that relays information regarding ongoing motor commands and the fish's behavior (Bell et al., 2008; Requarth and Sawtell, 2011). Whereas the instructive sensory input is relayed by electroreceptor afferent fibers, predictive inputs are transmitted by a set of granule cell parallel fibers similar to those found in the DCN and the cerebellum.

Anti-Hebbian synaptic plasticity has been proposed as simple mechanism that may contribute to adaptive filtering of predictable sensory input: Pairing of parallel fiber activity followed by instructive electroreceptor activity causes a long-term depression of the active parallel fiber synapses, whereas parallel fiber inputs that are anti-correlated with electrosensory stimuli become strengthened. Thus, electrosensory stimuli occurring in tandem with motor commands (e.g., self generated sensory input) reduce the strength of the active excitatory parallel fiber synapses, whereas stimuli that are unpaired with sensory stimuli increase the strength of parallel fiber inputs. As such, repetitive pairing of motor commands with electrosensory stimuli leads to a pattern of activity in ELL neurons that resembles highly-specific "negative images" of the activity which occurred during the pairing protocol (Han et al., 2000; Bell et al., 2008; Sawtell and Williams, 2008).

The DCN as an auditory, cerebellum-like structure: Adaptive filtering of self-generated sounds?

The DCN bears considerable homology to cerebellum-like structures such as the ELL. For example, similar to efferent neurons of the ELL, DCN fusiform cells integrate information from predictive and instructive sensory pathways. Predictive motor commands are relayed to fusiform cells via granule cell parallel fibers, whereas auditory nerve inputs are suggested to function as the instructive signal (Requarth and Sawtell, 2011). Furthermore, the local circuitry of the ELL and DCN are quite similar: Parallel fibers in the ELL recruit Purkinje-like medium ganglion cells and small GABAergic stellate cells that are strikingly similar to DCN cartwheel and superficial stellate cells, respectively (Bell et al., 2008). Thus, the DCN may similarly function as an adaptive filter, either via short-term or long-term plasticity mechanisms, to mitigate the salience of self-generated sounds such as chewing, breathing, or vocalizations, just as the ELL is suggested to generate "negative images" of self-generated electrosensory input in electric fish. However, specific data in support of the adaptive filter hypothesis of DCN function are lacking. More generally, the cellular mechanisms underlying the integration of predictive and instructive signals in the DCN are poorly understood.

Similar to other cerebellum-like structures, the DCN circuitry is divided into two separate sensory processing domains that ultimately converge upon efferent neurons (Figure 1). This segregation is exemplified by the fact that the auditory nerve and parallel fiber pathways recruit distinct types of interneurons. Thus, no interneuron in the DCN receives input from both sensory streams, implying that auditory and non-auditory information are processed by distinct local circuits and integrated only at the level of the

fusiform cell. However, this anatomical segregation is at odds with physiology data showing that neurons contacted solely by parallel fibers can nevertheless be excited or inhibited by auditory stimuli (e.g., cartwheel cells: Davis and Young, 2000; Portfors and Roberts, 2007). These data suggest either that a significant amount of auditory information is funneled through the parallel fiber pathway, or that previously undiscovered pathways in the DCN allow for integration of auditory and non-auditory inputs in local interneurons. This poses two outstanding questions regarding the activation of DCN interneurons:

1) What are the synaptic conductances involved in regulating the excitability of local interneurons?

2) Are there previously undiscovered pathways that allow for the integration of auditory nerve and parallel fiber inputs in local interneurons?

Superficial Stellate cells of the DCN: Molecular layer interneurons providing GABAergic (and glycinergic) inhibition.

Chapters 2-4 focus on the cellular physiology of the superficial stellate cell, a previously unstudied inhibitory interneuron in the DCN molecular layer. Previous anatomy studies have suggested that stellate cells perform a similar function in the DCN circuit as the stellate and basket cells of the cerebellar cortex (Wouterlood et al., 1984). For example, DCN stellate cells express markers of GABAergic neurons (Mugnaini, 1985) and are suggested to be electrically-coupled via dendro-dendritic gap junctions similar to cerebellar molecular layer interneurons (Wouterlood et al., 1984; Mugnaini,

1985; Mann-Metzer and Yarom, 1999). Given that even single stellate cells in the cerebellum can control the firing patterns of Purkinje cells (Oldfield et al., 2010), DCN stellate cells may provide strong GABAergic inhibition to the Purkinje-like cartwheel cells, and also perhaps to the apical dendrites of the fusiform cells. However, nothing is known regarding the synaptic inputs or even the postsynaptic targets of DCN stellate cells: Anatomy studies using Golgi stains were unable to discern the morphology of their myelinated axon (Wouterlood et al., 1984). Furthermore, there are literally only two published recordings from putative stellate cells (Zhang and Oertel, 1993; Golding and Oertel, 1997), which provide little information beyond a demonstration that these neurons fire action potentials and receive excitatory synaptic inputs.

The experiments of Chapter 2 examine the synaptic inputs to DCN stellate cells and compare them to the previously reported properties of cerebellar stellate and basket cells. We find that excitatory transmission is mediated by Ca^{2+}-permeable AMPA receptors with sub-millisecond kinetics, similar to what has been reported in the cerebellum (Liu and Cull-Candy, 2000; Jackson and Nicoll, 2011). Furthermore, single parallel fibers are sufficient to activate synaptic NMDA receptors that provide large, slow synaptic currents. Surprisingly, stellate cells were found to co-release glycine alongside GABA. This finding was unexpected, highlighting a strong functional divergence from the GABA-only stellate/basket cells of the cerebellum. Thus, co-release of fast inhibitory transmitters is a common feature of molecular layer interneurons in the DCN.

Electrical coupling between fusiform and stellate cells allows for cross-modal integration in DCN interneurons.

Electrical coupling is a common phenomenon in the brain, and allows populations of neurons to synchronize their activity (Alvarez et al., 2002; Bennett and Zukin, 2004; Vervaeke et al., 2010). However, electrical coupling is predominantly observed between inhibitory neurons of the same anatomical class; thus it is typically accepted that electrical synapses synchronize activity across populations of neurons that serve a similar function, instead of acting as mechanism to transmit information across different cell populations (Bennett and Zukin, 2004; Hestrin and Galarreta, 2005). By contrast, we find that the inhibitory stellate cells of the DCN are electrically-coupled to the excitatory fusiform cells via dendro-dendritic gap junctions. This discovery was not predicted by previous anatomy studies and significantly revises the circuitry of the DCN. Chapter 3 presents data showing that electrical coupling with fusiform cells is strong, persists throughout development, and allows the auditory nerve pathway to control the excitability of stellate cells independently of a direct projection into the DCN molecular layer. Furthermore, activating fusiform cells is sufficient to generate GABAergic inhibition in the DCN via this novel gap junction pathway. These findings represent a major revision of the DCN circuitry and provide a mechanistic basis for rapid, cross-modal signaling at the earliest stages of auditory processing.

Subthreshold activation of dendritic Na^+ channels and deactivation of I_h in fusiform cells generates an excitatory/inhibitory response sequence in stellate cells.

Synaptic transmission in the central nervous system is typically mediated by the release of neurotransmitters acting on ligand-gated receptors. However, the excitability of neurons is also heavily influenced by the activity of voltage-gated ion channels at the postsynaptic membrane. Given the voltage-dependence of these channels, synaptic inputs that modulate membrane voltage are predicted to have a significant effect on the activation of voltage-gated channels. Indeed, previous studies have shown that glutamate release can depolarize neurons and activate voltage-dependent Ca^{2+}, Na^+, and K^+ channels located in dendrites (Stuart and Sakmann, 1995; Hoffman et al., 1997; Losonczy et al., 2008; Harnett et al., 2013). These results imply that interactions between chemical synapses and voltage-gated ion channels shape information transfer in the brain.

A cation conductance commonly found in neurons is I_h. Originally described in cardiac tissue (Barbuti and DiFrancesco, 2008), I_h is paradoxically activated by hyperpolarizing the membrane potential away from spike threshold, and deactivated at more positive potentials. Unsurprisingly, I_h has been implicated in the genesis of pacemaker activity (Bal and McCormick, 1997; Barbuti and DiFrancesco, 2008) and rebound spiking in the brain (Kopp-Scheinpflug et al., 2011). Furthermore, previous studies show that the dendrites of hippocampal CA1 neurons contain a high concentration of HCN channels (Bittner et al., 2012), and synaptic glutamate release deactivates I_h by depolarizing dendrites (Magee, 1999). The deactivation of a resting cation conductance results in a net outward current that limits the amplitude and time course of excitatory postsynaptic potentials (Magee, 1999).

Previous studies show that the resting membrane potential of fusiform cells is determined by an interplay between a resting I_h conductance, inward rectifying K^+ channels, and a persistent Na^+ conductance (Leao et al., 2012; Rusznák et al., 2013). These results suggest that fusiform cell dendrites contain all three of these active conductances, and that that sub- or supra-threshold depolarizations generated by EPSPs or spike trains can activate Na^+ channels and deactivate the resting I_h conductance, as has been observed in other brain regions (Stuart and Sakmann, 1995; Magee, 1999). The experiments in Chapter 4 test the hypothesis that glutamatergic synapses onto fusiform cells activate a persistent Na^+ conductance and also deactivate the resting I_h conductance.

We find that the half-width and amplitude of parallel fiber EPSPs in fusiform cells is strongly controlled by a persistent Na^+ current. Furthermore, subthreshold EPSPs as well as spike trains in fusiform cells deactivated the resting I_h conductance, thereby causing the fusiform cell membrane potential to transiently drop below its baseline and generate an after-hyperpolarization (AHP) at the end of a depolarizing event. Surprisingly, the persistent Na^+ conductance activated by subthreshold EPSPs in fusiform cells propagated to electrically-coupled stellate cells, and this gap junction current comprised 70% of the total charge from parallel fiber->stellate cell transmission. Furthermore, the I_h-mediated AHP in fusiform cells generated robust inhibition in the interneurons that lasted several hundred milliseconds. Together, these results show that synaptic release of glutamate activates Na^+ channels and deactivates I_h in fusiform cells, thereby generating an excitatory/inhibitory sequence that propagates through an electrically-coupled network.

CHAPTER 1: RAPID, ACTIVITY-INDEPENDENT TURNOVER OF VESICULAR TRANSMITTER CONTENT AT A MIXED GLYCINE/GABA SYNAPSE.

Pierre F. Apostolides[1,2] and Laurence O. Trussell [2]

[1]Neuroscience Graduate Program

[2]Vollum Institute & Oregon Hearing Research Center, Oregon Health & Science University. Portland, Oregon, 97239, USA.

This chapter appeared as an article in *Journal of Neuroscience* (March 13, 2013; 33(11): 4768-81)

Abstract

The release of neurotransmitter via the fusion of transmitter-filled, presynaptic vesicles is the primary means by which neurons relay information. However, little is known regarding the molecular mechanisms that supply neurotransmitter destined for vesicle filling, the endogenous transmitter concentrations inside presynaptic nerve terminals or the dynamics of vesicle refilling after exocytosis. We addressed these issues by recording from synaptically-coupled pairs of glycine/GABA co-releasing interneurons (cartwheel cells) of the mouse dorsal cochlear nucleus. We find that the plasma membrane transporter GlyT2 and the intracellular enzyme glutamate decarboxylase supply the majority of glycine and GABA, respectively. Pharmacological block of GlyT2 or glutamate decarboxylase led to rapid and complete rundown of transmission, whereas increasing GABA synthesis via intracellular glutamate uncaging dramatically potentiated GABA release within one minute. These effects were surprisingly independent of exocytosis, indicating that pre-filled vesicles re-equilibrated upon acute changes in cytosolic transmitter. Titration of cytosolic transmitter with postsynaptic responses indicated that endogenous, non-vesicular glycine/GABA levels in nerve terminals are 5 to 7 mM, and that vesicular transport mechanisms are not saturated under basal conditions. Thus, cytosolic transmitter levels dynamically set the strength of inhibitory synapses in a release-independent manner.

Introduction

Synaptic vesicles express transporters that drive transmitter accumulation by exploiting a transvesicular voltage and/or pH gradient set by the vesicular ATPase (Edwards, 2007), and cytosolic transmitter levels in nerve terminals must be sufficiently concentrated to permit fast and efficient refilling of recycling vesicles. Indeed, the local cytosolic concentration should determine the rate and extent of vesicle filling, thereby controlling the size of the "quantum" of transmission (Edwards, 2007; Hori and Takahashi, 2012). However, the endogenous cytosolic concentration of most neurotransmitters is unknown, and despite its theoretical importance (Axmacher et al., 2004), the extent to which cytosolic transmitter levels impact vesicle filling is also unknown.

A related issue is whether vesicles retain their contents until release, or if pre-filled vesicles re-equilibrate upon acute changes in cytosolic transmitter independently of exocytosis. Isolated vesicles in certain biochemical experiments leak transmitter in absence of extra-lumenal substrate, suggesting that vesicle content may turn over rapidly (Burger et al., 1991; Floor et al., 1995). If such a leak were prominent in situ, vesicles would need to refill in the absence of activity; the amount of transmitter inside a vesicle would then reflect a "dynamic equilibrium" between transporter rates and leak (Williams, 1997; Edwards, 2007). This model predicts that changes in cytosolic transmitter will be rapidly mirrored as changes in vesicle filling, even at quiescent synapses. By contrast, studies at peripheral cholinergic synapses suggest that pre-filled vesicles are "sealed off" and only exchange their contents after exocytosis, implying that changes in cytosolic

transmitter will affect synaptic strength only after prolonged activity (Cabeza and Collier, 1988; Van der Kloot, 2003).

These questions are particularly important for inhibitory glycinergic and GABAergic synapses. The sole transporter responsible for packaging both glycine and GABA into vesicles, VGAT, has particularly low affinity for its substrates (K_m=5-10 mM; Christensen et al., 1990; McIntire et al., 1997). Previous studies suggest that nerve terminal transmitter may reach up to 20-40 mM for glycine (Supplisson and Roux, 2002) or 50-150 mM for GABA (Fonnum and Walberg, 1973). However, these values would saturate VGAT-mediated uptake (Christensen et al., 1990), implying that fluctuations in cytosolic transmitter will have little effect on vesicle filling even in the presence of a non-specific leak.

We addressed these issues in acute brain slices by identifying the mechanisms that supply cytosolic transmitter in synaptically-coupled pairs of glycine/GABA co-releasing cartwheel interneurons of the dorsal cochlear nucleus (DCN). These short-axon cells (Bender and Trussell, 2009) allowed us to manipulate the presynaptic cytosol and examine the control mechanisms for two major transmitter systems in an identified, homogenous cell population. We show that GlyT2 and glutamate decarboxylase (GAD) supply the majority of glycine and GABA, respectively. Endogenous cytosolic glycine/GABA levels are in the low mM and do not saturate vesicular transporters. Blocking GlyT2 or GAD, or acutely enhancing GAD activity, regulates transmission independently of the level of ongoing exocytosis. Thus pre-filled, release-ready vesicles in nerve terminals re-equilibrate their contents upon changes in cytosolic transmitter,

thereby implicating transmitter supply mechanisms as critical loci for regulating inhibitory synaptic strength.

Methods

Slice Preparation

All procedures involving animals were approved by OHSU's Institutional Animal Care and Use Committee. Wild-type mice of either sex (C57/BL6 or CBA) postnatal 15-24 days were used for the majority of the experiments. Optogenetic experiments were performed on GlyT2-cre transgenic mice (MMRRC Tg(Slc6a5-cre)KF109Gsat/Mmucd) containing a single copy of the *cre* transgene. Mice were anesthetized with isofluorane, decapitated, and 210-230 μm coronal slices of the DCN were cut in ice-cold solution containing (in mM) 87 NaCl, 25 $NaHCO_3$, 25 glucose, 75 sucrose, 2.5 KCL, 1.25 NaH_2PO_4, 0.5 $CaCl_2$, 7 $MgCl_2$, and bubbled with 5% CO_2/95% O_2. After cutting, slices were allowed to recover at 34° C in an ACSF solution containing (in mM) 130 NaCl, 2.1 KCl, 1.7 $CaCl_2$, 1 $MgSO_4$, 1.2 KH_2PO_4, 20 $NaHCO_3$, 3 Na-HEPES, 10-12 glucose, bubbled with 5% CO_2/95% O_2 (300-310 mOsm). In some experiments, 5 μM R-CPP or 50 μM D-APV were added to the incubation chamber. After a 30-45 min recovery period, slices were kept at room temperature (~22° C) until recording. Experiments were typically performed within 5 hours of slice preparation.

Electrophysiology

Slices were transferred to a recording chamber and continuously perfused at 3-4 ml/min with ACSF heated to 31-33° C by an inline heater. Inhibitory post-synaptic currents (IPSCs) were isolated by blocking excitatory transmission with 10 μM NBQX and 5 μM R-CPP (or 50 μM D-APV) in all experiments. Neurons were visualized by Dodt contrast optics with a 40x objective on an upright microscope (Zeiss Axioskop2). Cartwheel cells were identified by previously published criteria (Roberts et al., 2008; Bender and Trussell, 2009; Kuo and Trussell, 2011). The presynaptic pipette solution contained (in mM) 15.5 KCl, 105 K-gluconate, 4.8 $MgCl_2$, 4 ATP, 0.5 Tris-GTP, 14 Tris-phosphocreatine, 0.1 EGTA, 10 HEPES, pH 7.25 with KOH, ~290 mOsm. This solution was used for most postsynaptic recordings in Figures 1-4. In most experiments in Figures 5-8, postsynaptic cells were filled with an internal solution containing (in mM) 94.5 $CsMeSO_3$, 5 TEA-Cl, 5 QX314, 15.5 CsCl, 4.8 $MgCl_2$, 4 ATP, 0.5 GTP, 14 Tris-phosphocreatine, 0.1 EGTA, 10 HEPES. For mIPSC recordings and the majority of glutamate uncaging experiments, $CsMeSO_3$, QX314, and TEA-Cl were exchanged for 113 CsCl. For excised patch experiments, $CsMeSO_3$ was replaced by 103 CsCl. In experiments where presynaptic neurons were dialyzed with exogenous GABA and for puff experiments in Figure 8, 3 μM CGP55845 was added to the ACSF to prevent activation of $GABA_B$ receptors by GABA ejected from the pipette during seal formation. Pipette resistances with a K^+-based internal solution were typically 2-3 MOhm and 1.8-2.5 MOhm with the Cs^+-based internal solution. For postsynaptic recordings, cells were held between -70 and -80 mV. In some experiments, cells were transiently hyperpolarized to -120 mV during presynaptic action potentials to increase the absolute amplitude of

IPSCs. Series resistance of the postsynaptic cell (<15 MOhm) was compensated 60-80% 'correction', 90% 'prediction' (bandwidth=3 kHz) and experiments were not included if series resistance varied >20-25% over the course of the recording. Presynaptic cells were typically held between -70 and -80 mV in current-clamp. Action potentials were elicited every 15 s by positive current injection (0.8-1.5 nA, 1.5-2.5 ms) rapidly followed by negative current (between -0.5 and -1.5 nA, 100 ms) to prevent spike bursts. In some experiments, presynaptic cells were held in voltage clamp and spikes were elicited by steps (20-100 μs) to -20 or -30 mV. Under these conditions, some cartwheel cells displayed a prominent autaptic IPSC with similar properties as paired recordings and thus were used for a minority of the data points (n=1 in Figure 2D, n=2 in Figure 4, n=1 in Figure 8). For extracellular stimulation, voltage pulses (100-200 μs) were delivered once every 10-15 s through a bipolar theta glass electrode placed in the vicinity of the recorded neuron. In experiments in Figure 4 where cells were dialyzed with exogenous glycine, SR95531 was applied >25 min after establishing a presynaptic whole-cell recording. For puff application experiments in Figure 8, glycine and GABA were dissolved in ACSF and pressure ejected (5 psi, 5-20 ms) near the soma. For excised patch experiments, solutions were loaded into separate barrels of a double-barreled, theta-glass pipette and pressure ejected (20-30 psi, 5-20 ms) near the patch. Glycine and GABA puffs were interleaved.

Glutamate Uncaging

In Figure 7, MNI-glutamate (Tocris) was added only to the presynaptic internal solution. K^+ internal solution containing 5 mM MNI-glutamate was prepared in the dark and stored at -80^o C in opaque 1-ml tubes until the day of the experiment. In some experiments, 5

mM glutathione was added along with MNI-glutamate. Experiments were performed in the dark and trans-illumination from the microscope was turned off after establishing a paired recording. The microscope setup for uncaging was similar to that described by Otis et al., 1996.

Data Acquisition and Analysis

All data reported in the text and displayed in figures are expressed as mean ±SEM. Statistical comparisons were made using paired or unpaired Student's t-tests where appropriate. Data were collected with pClamp 9 software using a Multiclamp 700B amplifier and a Digidata 1322A analog-digital converter board. Traces were acquired at 20-50 kHz and low-pass filtered at 10-20 kHz. IPSCs were analyzed by filtering the traces offline at 2-4 kHz and measuring the peak amplitude. Amplitudes were normalized to a stable 5-10 minute baseline period (20-40 traces) and binned per minute. For the experiments with chelidonic acid in Figures 5 and 6, amplitudes were normalized to data during the first 2 min after breaking into the presynaptic cell.

mIPSC analysis

mIPSCs were recorded in 1 μM tetrodotoxin to block spikes, with 10 μM zolpidem + 30 μM pentobarbital to slow the decay kinetics of $GABA_A$ receptors and help distinguish them kinetically from glycinergic currents. Additionally, 10 μM baclofen was routinely added in these experiments. Baclofen reduced mIPSC frequency in cartwheel cells (unpublished observations) and thereby minimized the frequency of overlapping events. Individual mIPSCs were detected using a template algorithm (Axograph X) with a minimum amplitude cutoff between -10 and -20 pA. Events were inspected visually for

false positives or malformed events, and the decay components were fit by the following dual exponent function to determine the relative contribution of glycinergic and GABAergic transmission to individual events (Jonas et al., 1998):

$$y = y_{fast}e^{(-(x-offset)/\tau_{fast})} + y_{slow}e^{(-(x-offset)/\tau_{slow})}$$

t_{fast}=3.07 and t_{slow}=27.88 ms represent the average decay time of purely glycinergic or GABAergic events recorded in 10 μM SR95531 or 500 nM strychnine, respectively. We considered events as "mixed glycine/GABA" if both the amplitude of the fast and slow components were greater than 38.4 and 22 pA, respectively. These values represent the 2x S.D. cutoff for the amplitude of the fast component calculated from events recorded in strychnine (38.4 pA) and from the slow component recorded in SR95531 (22 pA).

Kinetic modeling

The kinetic model and transmitter time course described by Beato, 2008 for spinal interneurons was used to simulate IPSCs and their block by SR95531 in cartwheel cells. In the Beato model, a peak concentration of 3.3 mM was followed by a 0.64 ms exponential decay (obtained for a model in which desensitization was omitted), a glycine profile that accounted quantitatively for antagonism by SR95531 and enhancement following GlyT1 blockade. Axograph X software was used to drive the model with a set of peak glycine levels varying 0.5, 0.75, 1.0, 1.5, 2.0 and 2.5 times the optimal value determined in Beato (2008). For each of these values we then tested a set of SR95531 concentrations (0 to 6 mM), all with no change to the transmitter timecourse. Results in Figure 4C were obtained as the ratio of the response at 70 μM SR95531 to that at 10 μM SR95531, in parallel to the experimental data shown in this figure. The 3.3 mM glycine

value gave a fractional block in SR95531 lower than that observed experimentally (0.58 vs 0.65), suggesting that cartwheel cell vesicles release a somewhat higher concentration of glycine than do spinal interneurons.

In utero injections

Pregnant female mice (10.5-12.5 days pregnant) were deeply anesthetized, and abdominal surgeries were performed as described in Wang et al., 2012. Up to 8 embryos per dam were injected in the hindbrain with <200 nL of an AAV-FLEX-rev-ChR2-tdtomato construct (Addgene # 18917) along with dextran-conjugated Alexa488 using a beveled, glass capillary micropipette and a Parker Picospritzer III. Postnatal pups were genotyped for the *cre* transgene by PCR.

ChR2 activation

A 100W Hg bulb was placed in the epifluorescence port of the microscope and gated by a computer-controlled shutter (Uniblitz). Light was passed through a blue filter and brief flashes (2-50 ms) were delivered through the objective. In 4/8 experiments, we added 10 μM norepinephrine to the bath solution to reduce spontaneous firing of presynaptic cartwheel cells and increase the signal/noise ratio of IPSCs (Kuo and Trussell, 2011). No difference was observed in the glycine/GABA ratio ($p=0.458$) with and without norepinephrine so the data were pooled. ChR2 stimulation evoked "complex spike" bursts of 2-4 IPSCs per light flash. We analyzed the glycine/GABA ratio of these bursts by measuring peak amplitude of the IPSC with the most stable baseline amplitude (typically the second or third IPSC in the burst) after peak aligning the individual sweeps.

Statistics

All data reported in the text and displayed in figures are expressed as mean ±SEM. Statistical comparisons were made using paired or unpaired Student's t-tests where appropriate. Fits to dose-response curves were performed on raw data using a sigmoid or Hill equation with Igor 6.22. The purpose of these fits was to determine through interpolation a predicted concentration for a given response amplitude.Reliability of the estimates of intracellular transmitter concentrations based on these curve fits was determined using a jackknife procedure (Efron and Tibshirani, 1986). In each data set, a single point was removed, and the fit recalculated; the procedure was then repeated sequentially with removal and replacement of all points. Estimates of the concentration were determined from the mean of values obtained from the different curve fits. The error of the mean was then scaled by the number of iterations, according to Equation 10.10 of Efron and Tibshirani (1986).

Reagents

NBQX, D-APV, R-CPP, SR95531 were from Ascent Scientific/Abcam. MNI-glutamate was from Tocris. Strychnine, pentobarbital, zolpidem, and chelidonic acid were from Sigma Aldrich. ORG25543 was a gift from Hardy Sundaram at Organon.

Results

Synaptic transmission between cartwheel cells is predominantly glycinergic.

Because VGAT packages both glycine and GABA into vesicles, functional co-release of glycine/GABA occurs at many synapses in juvenile and mature animals (Jonas et al., 1998; Awatramani et al., 2005). While cartwheel cells label with antibodies against both glycine and GABA (Wenthold et al., 1987), inhibitory transmission is reported to be predominantly glycinergic (Roberts et al., 2008; Mancilla and Manis, 2009).

To further define the balance between the two transmitter systems, paired pre- and post-synaptic recordings were made between neighboring cartwheel cells. Action potentials elicited in a presynaptic cell caused short latency, monosynaptic inhibitory postsynaptic currents (IPSCs) in its voltage-clamped postsynaptic target cell (Figure 1A). In agreement with previous studies, bath application of the glycine receptor antagonist strychnine (500 nM) significantly reduced IPSCs to 13±2% of control (blue traces, n=8. Roberts et al., 2008). The $GABA_A$ receptor antagonist SR95531 (10 μM) blocked the strychnine-insensitive component (2±1% remaining, n=7), showing that glycine and GABA were co-released from the same presynaptic cell. Cytosolic GABA can wash out during whole-cell recordings (Smith and Jahr, 2002; Diana and Marty, 2003), which may underestimate the GABAergic contribution to transmission in cartwheel cell pairs. We tried to avoid washout by applying blockers soon after recording began. Nevertheless, to determine whether the glycinergic predominance was due to selective washout of GABA, we expressed in cartwheel cells the light-activated ion channel channelrhodopsin2 (ChR2) via *in utero* viral transfection in GlyT2-cre transgenic mice (see Methods). Because GlyT2 is specifically expressed in glycinergic neurons (Zafra et al., 1995), viral

transfection results in mosaic expression of ChR2 in cartwheel cells, enabling activation of these neurons via blue light stimuli. In DCN slices from injected GlyT2-cre mice, wide field flashes of blue light (2-50 ms duration) caused barrages of "complex spike" IPSCs previously attributed to burst firing of presynaptic cartwheel cells (Figure 1B; Roberts et al., 2008). 500 nM strychnine reduced the amplitude of ChR2-evoked IPSCs to 16±3% of baseline (n=8), whereas SR95531 blocked the remaining IPSCs (2±1% of baseline remaining, n=8). The IPSC remaining in strychnine was not significantly different between paired recordings and optogenetic experiments (Figure 1C; p=0.32.)

Cartwheel cells receive inhibitory inputs from two main sources: Other cartwheel cells and superficial stellate cells (Rubio and Juiz, 2004). However, stellate cells are thought to be predominantly GABAergic (Rubio and Juiz, 2004) and their connectivity rate is lower than cartwheel <-> cartwheel pairs (Apostolides and Trussell, unpublished observations). We also recorded miniature IPSCs (mIPSCs) to test whether glycine and GABA were co-packaged in the same vesicles, similar to other brain regions (Jonas et al., 1998; Nabekura et al., 2004); Awatramani et al., 2005). We recorded mIPSCs in 1μM tetrodotoxin to block spikes, along with 10 μM zolpidem and 30 μM pentobarbital to slow the decay kinetics of $GABA_A$ receptors. Under these conditions, the decay time constant of $GABA_A$ mIPSCs isolated with strychnine was ~10 fold slower than that of glycine mIPSCs isolated with SR95531 (glycine = 3.0±0.2 ms, n=9; $GABA_A$ = 27.9±2.0 ms, n=9). Consequently, mIPSCs recorded in the absence of inhibitory blockers displayed a spectrum of decay kinetics and could be classified into three basic categories (Figure 1D): Rapidly decaying glycinergic events, slowly decaying events mediated by $GABA_A$ receptors, and a third population with both fast glycine and slow GABAergic

decay components. We determined the relative amplitude of the glycinergic and GABAergic components of mIPSCs by force-fitting the decay phase of individual events with a double exponential function containing the average glycine and $GABA_A$ decay time constants (Jonas et al., 1998; Awatramani et al., 2005). Figure 1E shows representative data from 2 cells, plotting the amplitude of the glycine component against the GABA component for individual mIPSCs. The dashed lines mark the ± 2x S.D. amplitude cutoffs for $GABA_A$ (horizontal) or glycine (vertical) events. We categorized events falling above both vertical and horizontal S.D. lines as "dual component" mIPSCs and thus mediated by both transmitters. On average, 19.3±2.2% of events recorded in absence of inhibitory blockers were classified as mixed glycine/GABA mIPSCs (n=14 cells; Figure 1G). Importantly, adding 10 μM SR95531 (n=10) or 500 nM strychnine (n=4) to the bath solution reduced the fraction of mIPSCs falling above the 2x S.D. lines to 1.5±0.3% (Figure 1F,G). Thus, cartwheel cells co-package GABA and glycine in the same vesicle similar to other co-releasing synapses.

GlyT2 activity determines glycinergic synaptic strength on a time-scale of minutes.

Genetic deletion or chronic block of the plasma membrane glycine transporter GlyT2 reduces the amplitude of glycine mIPSCs in cultured spinal neurons, suggesting that GlyT2 can regulate glycine availability in nerve terminals (Gomeza et al., 2003; Rousseau et al., 2008). However, such chronic manipulations do not abolish glycinergic transmission, implying that nerve terminals can maintain glycine for long periods of time independent of GlyT2, or possibly compensate for loss of GlyT2 activity. Furthermore, in some cases acute block of GlyT2 reduces glycine mIPSC frequency without affecting

mIPSC amplitudes (Bradaïa et al., 2004), suggesting that any acute effects of GlyT2 block could potentially reflect an influence of GlyT2 on presynaptic release probability (but see Rousseau et al., 2008), as has been demonstrated for other cation-coupled transporters (Bagley et al., 2011). We determined the extent to which GlyT2 actively regulates cytosolic glycine levels by assessing the acute effect of a selective GlyT2 inhibitor (ORG25543, 1 μM) on glycine IPSCs. Pairs were recorded in 10 μM SR95531 to isolate glycinergic transmission and ORG25543 was bath applied after establishing a stable baseline. IPSC amplitudes ran down soon after drug application (Figure 2A), declining to 59±11% (n=9) of baseline within 10-11 min (Fig 2D). The rate of rundown was variable between experiments (Figure 2D), although IPSCs invariably dropped to 3±1% of baseline within 30 min of drug application (n=9, p=0.0003). These results show that GlyT2 constitutively supplies glycine for moment-to-moment refilling of recycling vesicles.

Vesicles re-equilibrate with reduced cytosolic transmitter levels independently of exocytosis.

We next tested whether the rundown induced by glycine depletion was affected by the rate of stimulation, either by suspending presynaptic activity during the first 10 min of ORG25543 application, or by increasing the rate of stimulation 30 fold, from 0.067 Hz to 2 Hz (Figure 2B-D). Surprisingly, neither manipulation altered the rate of loss of glycinergic transmission. When stimulation was omitted, IPSCs declined to 57±9% of baseline (Figure 2B,D, n=10), as observed when presynaptic stimulation resumed 10-11 min after ORG25543 application. This value was not significantly different (p=0.83)

from experiments at 0.07 Hz (Figure 2D). In 9 of 10 experiments, stimulation was again stopped for 7-10 min as slices remained exposed to ORG25543. Immediately upon resuming stimulation at 20-23 min, IPSCs were now further depressed to 12±4% of baseline. Again, these values were not significantly different (p=0.294) from the fraction remaining with continuous activity (14±4%, n=8). Conversely, transiently increasing the stimulus rate to 2 Hz to augment vesicle release during ORG25543 application did not appreciably accelerate run down, with amplitudes remaining at 66±27% of baseline (n=3) after 10-11 min (Figure 2C,D). These results argue that glycine content inside vesicles is not static, but rapidly re-equilibrates upon acute reductions in extra-lumenal glycine levels.

Could spontaneous vesicle release account for the apparent activity-independence of rundown during ORG25543 application? In cartwheel cells, glycine mIPSCs recorded in TTX using a CsCl internal solution (without pentobarbital + zolpidem added to the bath) had an average amplitude of 68.8 ± 5.3 pA and occurred with a frequency of 12.3 ± 1.0 Hz (n=16 cells; data not shown). In separate experiments, we estimated the number of functional release sites between single cartwheel cell pairs by loading pre- and post-synaptic neurons with a CsCl-internal solution. Adding CsCl to the presynaptic neuron blocks K^+ channels and broadens the presynaptic action potential waveform, thereby enhancing Ca^{2+} influx and release probability in nerve terminals (Vincent and Marty, 1996). Unitary glycine IPSCs evoked under these conditions had an average amplitude of 4.8 ± 1.4 nA (n=14 pairs; data not shown), suggesting that the reciprocal synapses between cartwheel cells are made up of at minimum ~70 release sites (unitary IPSC/mIPSC amplitude: 4800/69 = 69.5). Based on correlation analysis, cartwheel cells

are probably contacted by at least 2 other cartwheel cells (Roberts and Trussell 2010). If we assume that a single neuron is contacted by 5 neighboring presynaptic cartwheel cells, the frequency of spontaneous fusion at a single release site is on the order of one to two vesicles per min (12.3 Hz/350 release sites = 0.035 Hz/release site). Thus, during a 10-min application of ORG25543, only 20 release sites from a presynaptic neuron will have spontaneously released a single vesicle. If each site contains on average 3 release-ready vesicles (Trigo et al., 2012), spontaneous vesicle fusion will have turned over only 10% of all release-ready vesicles from a single presynaptic neuron.

We also tested whether ORG25543-induced rundown was due to a spurious drug effect on release probability by adding glycine (20 mM) to the pipette solution and subsequently bath applying ORG25543 (Figure 2E). Glycinergic transmission was stable for the entirety of the experiment, with IPSC amplitudes remaining at 106±21% of baseline (n=6) 30-36 min after drug application. This indicates that ORG25543 acted by depleting the terminal of glycine, and also that pipette contents effectively reach presynaptic terminals. The possibility was also tested that washout of presynaptic glycine during prolonged whole-cell dialysis with transmitter-free solution could reduce IPSC amplitude (Diana and Marty, 2003). When pairs were recorded with a glycine-free internal solution, IPSC amplitudes min 35-40 remained at 98±11% of the first five min (n=7, p=0.98. Figure 2F) suggesting that whole-cell dialysis does not significantly reduce presynaptic glycine while GlyT2 is active. Finally, establishing paired recordings with glycine in the presynaptic electrode *after* pre-incubation in ORG25543 rapidly restored transmission (Figure 3), arguing that loss of intracellular glycine does not have a deleterious effect on nerve terminals.

GlyT2-supplied glycine does not saturate VGAT.

Our data indicate that cytosolic transmitter levels determine the level of vesicle filling, and thus the strength of transmission. However, VGAT has a low affinity for glycine and GABA, suggesting that terminals must contain mM levels of free transmitter to adequately refill vesicles. Indeed, GlyT2 can establish intracellular glycine concentrations up to 20-40 mM from nanomolar extracellular pools (Supplisson and Roux, 2002), although concentrations above ~10 mM are expected to saturate VGAT function (Christensen et al., 1990). We tested for such saturation by measuring the degree of block of IPSCs by the low-affinity, competitive glycine receptor antagonist SR95531, under basal conditions and in pairs with 20 mM glycine in the presynaptic pipette. SR95531 blocks $GABA_A$ receptors with high affinity, although it also acts as a low-affinity competitive antagonist of glycine receptors at concentrations >30 μM (Beato et al., 2007);(Beato, 2008). The off-rate of SR95531 from glycine receptors (~30 μs) is shorter than the duration of the synaptic glycine transient (Beato et al., 2007). Thus, a significant fraction of glycine receptors will unbind SR95531 while glycine is still present in the synaptic cleft, making the degree of block by a set concentration of SR95531 inversely proportional to the amount of glycine released in the cleft following exocytosis (Beato, 2008). If the basal cytoplasmic glycine concentration saturates VGAT, experimentally increasing presynaptic glycine levels should have no effect on the efficacy of SR95531 to block glycine receptors compared to control. Alternatively, if vesicular transport is not saturated under basal conditions, SR95531 should reduce IPSC amplitudes significantly less when presynaptic neurons are loaded with 20 mM glycine compared to control conditions with no added transmitter.

SR95531 (10 μM) was present during the baseline period to block $GABA_A$ receptors. In control pairs with no exogenous glycine in the internal solution, increasing SR95531 from 10 to 70 μM reduced glycine IPSCs to 63±3% of baseline (Figure 4A; n=10). 70 μM SR95531 similarly reduced glycine IPSCs evoked with an extracellular stimulating electrode (65±3%, n=6, p=0.68 compared to control pairs), indicating that whole-cell recording from the presynaptic neuron did not significantly diminish the amount of glycine released in the cleft. By contrast, 70 μM SR95531 reduced IPSCs significantly less when 20 mM glycine was added to the presynaptic pipette (77±3% of baseline, n=8, p=0.0014 compared to control pairs). Thus, increasing cytosolic glycine levels near presynaptic vesicles resulted in a higher peak transmitter concentration released per action potential, indicating that the glycine provided by GlyT2 does not saturate VGAT function.

The endogenous concentration of glycine in nerve terminals.

We used the low-affinity antagonist approach to determine the endogenous glycine concentration supplied by GlyT2 by pre-incubating slices in 1 μM ORG25543 to deplete cartwheel cells of their endogenous glycine, and "rescuing" transmission with experimentally-defined glycine concentrations in the recording pipette. IPSCs evoked with 2 mM glycine in the pipette were significantly more sensitive to 70 μM SR95531 than in control conditions (Figure 4A; 52±4% reduction, n=8. p=0.02 and 0.03 compared to control pairs and extracellularly-evoked IPSCs, respectively), showing that GlyT2 must supply more than 2 mM glycine. In pairs loaded with 5 mM glycine, 70 μM SR95531 reduced IPSCs to 65±2% of baseline (n=9). This reduction was similar to

control pairs (p=0.74) and extracellularly-evoked IPSCs (p=0.998). 70 μM SR95531 similarly reduced IPSCs with 10 mM glycine in the pipette (69±3% of baseline remaining, n=5). By fitting these concentration-block data with a Hill function (Figure 4B), we find that the values from control pairs and extracellular stimulation experiments lie near the 5 mM data point (gray bar). Using a value of control block of 0.65, a jackknife analysis of the curve fit to these data (see Methods) indicated that GlyT2 supplies about 5.4±1.0 mM glycine to presynaptic terminals (mean and SEM of fits to 30 trials).

What range of vesicular glycine concentrations might result from the 10-fold range of cytosolic glycine levels that we tested? As we could not directly measure vesicular glycine *in situ*, we adopted an indirect, modeling approach, and determined the predicted values of cleft glycine concentrations that would be associated with the various levels of block observed with SR95531. The results of Beato (2008) were used as a starting point for a kinetic model of synaptic glycine receptors and for an initial value for peak cleft glycine concentration and transmitter time course. Both peak cleft glycine and SR95531 values were varied in the model, and a fractional block was expressed as block in 70 uM / 10 uM SR95531 in order to directly compare values to the experimental data of Figure 4A and B. The results shown in Figure 4A and C indicate that a degree of block similar to that seen with control recordings was obtainable in the model with just under 5 mM peak cleft glycine. Importantly, the results show that although the range we observed of fractional block by SR95531 was <50%, such a range would correspond to a > 3-fold variation in cleft glycine and, presumably, a similar range in vesicular glycine.

GAD is the predominant source of GABA in cartwheel cell terminals.

We next tested whether GAD is the main supplier of GABA to vesicles by dialyzing presynaptic neurons with chelidonic acid, a conformationally-restricted analogue of glutamate that rapidly and competitively inhibits GAD (Porter and Martin, 1985). GABAergic transmission was isolated with 500 nM strychnine, and pairs were recorded with chelidonic acid (1 mM) in the presynaptic pipette. Data collection began within 30 s of breaking into the presynaptic cell. Figure 5A (blue circles) shows that $GABA_A$ IPSCs ran down rapidly after break-in, reaching 11±1% of their initial amplitude after 20 min of presynaptic dialysis (n=9). This remaining component probably reflects a residual glycinergic component not blocked by 500 nM strychnine. These data show that *de novo* synthesis by GAD is the main source of GABA in nerve terminals, and tightly regulates vesicular GABA content on the order of minutes.

Similar to previous studies recording from pairs of GABAergic neurons (Smith and Jahr, 2002; Diana and Marty, 2003), we observed partial rundown of $GABA_A$ IPSCs after ~10 min of whole-cell dialysis with our standard internal solution (without chelidonic acid). This rundown stabilized to 43±7% of baseline after 20-30 min (n=8. Figure 5A,B). Adding 5 mM glutamate to the internal solution significantly reduced this rundown (Figure 5A,B. Fraction remaining after 20-30 min: 88±5%, n=9, p=0.0002 compared to control conditions) supporting an essential role for GAD in supplying GABA for vesicle filling**.** Furthermore, adding exogenous GABA (20 mM) to the presynaptic internal solution rapidly and significantly potentiated transmission to 130±5% of the first 2 min (open circles. p=0.01, n=5). Thus, unlike GlyT2-supplied glycine, vesicular packaging of

GABA does not function optimally during whole-cell dialysis due to washout of GABA and/or its precursor glutamate.

The effective cytosolic concentration of GABA.

Based on the previous observations we estimated the endogenous GABA concentration in nerve terminals by dialyzing presynaptic cells with chelidonic acid plus defined concentrations of exogenous GABA, and determined the amount of GABA necessary to maintain transmission near baseline for 20-30 min. With 2 mM GABA + chelidonic acid in the presynaptic cell (Fig 6A,B), the fraction remaining was 32±6% of baseline (n=7), suggesting that cytosolic GABA levels must be higher than 2 mM. The fraction remaining with 5 mM GABA + chelidonic acid was 82±12% of baseline (n=8), while 10 mM GABA + chelidonic acid potentiated transmission to 130±22% of baseline (n=12; Fig 6A,B). A sigmoid fit to these data using a jackknife procedure (see Methods) indicated that transmission would be maintained at a constant level by 6.2±1.2 mM intracellular GABA (mean and SEM for 40 iterations; Fig 6B). Thus, these observations suggest that synaptic vesicles in cartwheel cell terminals are exposed to similar levels of cytoplasmic GABA and glycine.

GABA is synthesized and loaded into synaptic vesicles on the time scale of minutes.

Is GAD turnover sufficiently fast to supply the high concentrations of GABA needed to refill vesicles? Classic experiments in purified vesicles, along with a recent study at the calyx of Held, suggest that synaptic vesicles rapidly (<1 min) accumulate transmitter

(Christensen et al., 1990; Hori and Takahashi, 2012). However, these experiments could not address whether endogenous transmitter supply mechanisms operate on a similar time scale. Conversely, experiments at cholinergic synapses suggest that newly-synthesized acetylcholine does not readily incorporate into synaptic vesicles unless the preparation is extensively stimulated (Potter, 1970; Agoston et al., 1985), arguing that transmitter synthesis lags behind vesicle filling under periods of low activity. Having established that GAD is the main supplier of GABA, we therefore asked if inhibitory synaptic strength is tightly coupled to GABA synthesis, or whether transmitter supply mechanisms affect transmission only after a significant delay. We dialyzed presynaptic cells with a solution containing no added GABA or glutamate, but rather a caged glutamate compound (MNI-glutamate; 5 mM). The loss of endogenous glutamate and GABA led to rundown of transmission, as expected from the experiments in Figure 5, and subsequently uncaging glutamate inside the terminal rapidly increased local GAD substrate. Figure 7A shows data from a typical experiment, plotting the amplitude of individual GABAergic IPSCs (recorded in strychnine) over time. MNI-glutamate was uncaged with wide-field illumination by UV light (500 ms) at times denoted by the red line. The results were dramatic, with IPSC amplitudes potentiating >3-fold within two minutes. Indeed, the first test points taken even 15 and 30 s after uncaging are clearly enhanced above pre-flash baseline. These data illustrate that GABA is synthesized and packaged into release-ready vesicles within seconds of increases in nerve terminal glutamate concentrations.

We next tested whether GABA synthesis and/or vesicle refilling required activity. MNI-glutamate was uncaged in the absence of presynaptic activity, and the resumption of test stimuli was delayed for ~3 min. An example is shown in Figure 7A, where pre-

synaptic activity was suspended at the 20-min mark, followed by a 500-ms UV flash. When stimulation was resumed, IPSCs were clearly potentiated compared to baseline. These data show that *de novo* transmitter synthesis and vesicle filling are remarkably independent of exocytic history.

The potentiation under the two stimulus conditions was quantified and compared by normalizing IPSCs to the average amplitude during a five-min epoch before uncaging and binning these values per min. With continuous presynaptic activity, IPSC amplitudes increased significantly to 204±12% of baseline 3-5 min after uncaging (Figure 7B, n=12, p=0.0004). Following an absence of stimulation, IPSC amplitudes similarly increased to 211±12% of baseline (Figure 7C, n=9, p=0.0005). The degree of potentiation was not significantly different between these two data sets (p=0.6), showing that the refilling of vesicles was virtually independent of electrical activity.

Several control experiments rejected alternative interpretations that could account for the rapid potentiation following uncaging. 500-ms UV flashes with no MNI-glutamate in the pipette did not potentiate GABAergic transmission (IPSC amplitudes 3-5 min after UV flashes: 71±7% of baseline, n=3), ruling out direct effects of UV light on $GABA_A$ receptors (Chang et al., 2001). Furthermore, uncaging MNI-glutamate in presynaptic cartwheel cells had no effect on glycinergic IPSCs recorded in 10 μM SR95531 (IPSC amplitudes 3-5 min after uncaging were 93±4% of baseline, n=9, p=0.35), demonstrating that uncaging glutamate does not merely increase the probability of vesicle release. Finally, uncaging-induced potentiation of $GABA_A$ IPSCs was absent when presynaptic cells were loaded with 5 mM MNI-glutamate and 1 mM chelidonic acid (IPSC amplitudes 3-5 min after uncaging were 75±9% of baseline, n=7), showing that

potentiation required *de novo* GABA synthesis. Taken together, these data confirm that GABAergic transmission is temporally coupled to increases in GAD substrate availability, and that the extent of increase is not influenced by ongoing exocytosis.

Transmission is predominantly glycinergic even when terminals contain similar GABA and glycine levels.

The results thus far suggest that cartwheel cell terminals contain similar concentrations of glycine and GABA. As an independent test of our presynaptic glycine/GABA estimate, we loaded cartwheel cells with the concentrations determined in Figures 4 and 6 (5 mM glycine and 7 mM GABA), while depleting neurons of endogenous glycine/GABA by preincubating in 1 μM ORG25543 and adding chelidonic acid to the internal solution. Under these conditions, 500 nM strychnine reduced IPSC amplitudes to 24±1% of baseline (Figure 8A,B; n=10), and subsequent application of 10 μM SR95531 reduced the remaining IPSCs to 1.3±0.2% (n=7). Given that IPSCs were predominantly glycinergic in all 10 pairs tested (Figure 8B), these results indicate that cartwheel cells contain roughly equal concentrations of glycine and GABA, and suggest that postsynaptic factors determine IPSC identity.

Postsynaptic receptor expression determines IPSC phenotype.

One transmitter typically predominates over the other at mixed glycine/GABA synapses, but whether this is due to different ratios of transmitter in presynaptic vesicles (Nabekura et al., 2004) or differential postsynaptic expression of glycine and $GABA_A$

receptors (Dugué et al., 2005) is controversial. Given that VGAT has a ~2-fold higher affinity for GABA than glycine (Burger et al., 1991), the largely glycinergic phenotype in Figure 1 might be determined postsynaptically and not by differential presynaptic glycine/GABA levels. We tested whether the postsynaptic response to exogenous glycine and $GABA_A$ differed in parallel to that of synaptic responses by quantifying the relative amplitude of currents evoked by puff application of 1 mM glycine or GABA onto the same neuron (Figure 8C,D). The average amplitude of glycine-evoked currents was always substantially greater than the $GABA_A$ component ($p=0.006$, $n=7$), with an average glycine/GABA ratio of 3.6±0.3 (Figure 8D). Because the puff-evoked whole-cell currents were often several nano-amperes in amplitude, we worried that voltage-clamp errors could distort these results. Furthermore, saturating concentrations of agonists may lead to receptor desensitization during puffs. To overcome these limitations and apply agonists more uniformly, we performed excised ("outside-out") patch experiments from cartwheel cell soma and puff-applied glycine and GABA (1 mM each) to the same membrane patch. In agreement with our whole-cell results, glycine evoked significantly larger responses than GABA in excised patches, with a peak glycine/GABA ratio of 3.5 ± 1.4 ($n=11$ patches, $p=0.003$). These results, along with our finding that cartwheel cell terminals contain similar glycine/GABA concentrations, show that the IPSC phenotype in cartwheel cells is determined by the relative expression of postsynaptic glycine/$GABA_A$ receptors and not by different transmitter levels in synaptic vesicles.

Discussion

Vesicular transmitter content is in dynamic equilibrium with cytosolic concentrations.

We used paired recordings to determine the molecular mechanisms, temporal dynamics, and cytosolic transmitter concentrations involved in vesicle refilling at a mixed glycine/GABA synapse. Surprisingly, neither up- or down-regulation of vesicle content was modified by activity-driven exocytosis, suggesting that vesicular transmitter turns over in minutes, independent of activity. These results establish that synaptic vesicle content is not merely a static reflection of initial transport activity following vesicle biogenesis, but is dynamically regulated by ongoing fluctuations in cytosolic transmitter availability.

Our results contrast with studies at cholinergic synapses, where blocking vesicular acetylcholine uptake does not affect transmission unless axons are stimulated extensively and ~15% of the vesicle pool has turned over (Cabeza and Collier, 1988; Searl et al., 1991). Furthermore, radio-labeled acetylcholine does not incorporate into vesicles in un-stimulated preparations (Agoston et al., 1985; Whittaker, 1987), suggesting that vesicles do not increase their contents upon acute increases in cytosolic transmitter, nor is active synthesis of acetylcholine required to maintain vesicle content. Thus, it is thought that cholinergic vesicles are "sealed off" and cannot change their contents until they are recycled after exocytosis, thereby limiting fluctuations in cytoplasmic transmitter from affecting transmission only after significant activity (Van der Kloot, 2003). One explanation is that positively charged acetylcholine may be less prone to leaking from vesicles than glycine/GABA, which are transported as neutral zwitterions (Edwards, 2007).

Recent studies exploring this issue at inhibitory synapses in the hippocampus provided differing results, with some data suggesting that vesicles re-equilibrate independent of exocytosis after acutely blocking GABA synthesis (Mathews and Diamond, 2003), whereas another study required significant activity to observe changes in vesicle filling (Liang et al., 2006). One explanation is that differences in spontaneous firing of presynaptic neurons may result in different rates of vesicle turnover during experiments. Indeed, extensive stimulation produces a component of synaptic depression due to depletion of glycine availability in terminal (Rousseau et al., 2008). We controlled the degree of presynaptic activity using paired recordings and found that regulation of cytosolic transmitter caused rapid, activity-independent changes in transmitter release. Our results corroborate a model whereby vesicle content reflects the balance between transport-mediated uptake of cytosolic transmitter and non-specific efflux.

GlyT2 provides glycine for cartwheel cell nerve terminals.

Previous studies show that GlyT2 is intimately linked to refilling of glycinergic vesicles (Rousseau et al., 2008). However, alternative sources may also supply glycine to fill synaptic vesicles: GlyT2 -/- mice exhibit some glycinergic transmission, albeit with reduced quantal size (Gomeza et al., 2003), and preincubation of cultured spinal neurons with ORG25543 for 12-24 hours does not completely abolish glycine IPSCs (Rousseau et al., 2008). Our results extend these observations by demonstrating that GlyT2 is the main, if not only source of glycine for constitutive vesicle refilling (Figure 2). Thus, any alternative pathway for intracellular synthesis or uptake of glycine is likely to operate on a slower time scale than GlyT2.

GAD is the main supplier of vesicular GABA.

GABA is synthesized from the decarboxylation of glutamate by GAD65 and GAD67, and mutant mice lacking both GAD isoforms have no detectable brain GABA (Ji et al., 1999). However, pharmacological block of GAD using extracellularly applied antagonists over several hours typically fails to abolish GABAergic transmission (Engel et al., 2001; Mathews and Diamond, 2003; Lu et al., 2008). Thus, while GAD is involved in synthesizing GABA for vesicular transport, it is possible that other sources, such as local recapture by plasma membrane GAT1 transporters (Kirmse and Kirischuk, 2006) or synthesis from polyamines (Bell et al., 2011), may also rapidly concentrate GABA near synaptic vesicles. However, we find that direct application of a GAD inhibitor to the presynaptic cytosol causes rapid and almost complete run down of GABAergic transmission that is reversed, in a concentration-dependent manner, by the addition of exogenous GABA to the pipette (Figure 6). Moreover, in GABA depleted synapses, step increases in cytosolic glutamate through intracellular uncaging restored GABAergic transmission within seconds (Figure 7).

Why do other studies report incomplete reductions in GABAergic transmission with GAD inhibitors, even after incubations >12 hours (e.g. Engel et al., 2001)? A commonly employed GAD inhibitor, 3-mercaptopropionic acid, blocks only ~50% of GABA synthesis in brain slices, even at saturating concentrations (Dericioglu et al., 2008). Chelidonic acid is a potent GAD inhibitor that is competitive with glutamate and does not inhibit GAD by interfering with its required co-factor, pyridoxal-phosphate (Porter and Martin, 1985). To our knowledge, our study is the first to apply directly a GAD inhibitor

inside nerve terminals to determine the extent to which GAD supplies GABA for vesicle refilling.

Synaptic vesicles are exposed to low mM glycine/GABA concentrations.

Little is known about endogenous transmitter levels inside nerve terminals. One study suggested that the endogenous glutamate concentration in the cytoplasm is 1-10 mM (Ishikawa et al., 2002), while experiments in chromaffin cells estimated that catecholamines are between 5-50 μM (Mosharov et al., 2003). There have been no functional estimates of intracellular glycine/GABA levels until now. Previous studies proposed GABA concentrations ranging from 7 mM in somata (Obata et al., 1970; Otsuka et al., 1971) to 50-150 mM in nerve terminals (Fonnum and Walberg, 1973), while glycine may be near 20-40 mM (Supplisson and Roux, 2002). These estimates raise the intriguing possibility that VGAT saturation is a prerequisite for efficient refilling of inhibitory vesicles. However, we find that endogenous transmitter does not saturate vesicular transporters, as dialyzing presynaptic cells with high concentrations of glycine or GABA reduced the efficacy of a fast-off glycine receptor antagonist (Figure 4) and potentiated GABAergic transmission (Figure 5).

Our cytosolic transmitter estimates agree with the work of Obata et al. (1970) and Otsuka et al. (1971) in Purkinje cell somata. Cartwheel cells share considerable homology to Purkinje cells (Mugnaini et al., 1987), suggesting that our estimates extend to GABA-only synapses. Nevertheless our results may represent underestimates, as previous work suggests that cytosolic glycine and GABA compete for vesicular transport

(Burger et al., 1991). Moreover, the concentrations reached in the terminal cytoplasm may be somewhat lower than that of the pipette. Our experiments were limited by the fact that GABA, but not glycine washes out during whole-cell dialysis (Figures 2D and 5A). Thus, if GABA and glycine compete for vesicular transport, the 5 mM glycine estimate was calculated under conditions where endogenous GABA is reduced by approximately 50%. However it should be noted that GAD is anchored to synaptic vesicles in nerve terminals (Kanaani et al., 2002; Jin et al., 2003). This association with vesicles could reduce the extent to which glycine and GABA compete for vesicular transport by establishing spatial "nanodomains" of GABA that would be preferentially transported by VGAT. In agreement with minimal competition are data showing that neither pharmacological block (Bradaïa et al., 2004; Rousseau et al., 2008) nor genetic deletion of GlyT2 (Latal et al., 2010) increase $GABA_A$ mIPSC amplitudes in spinal neurons (but see Xu et al., 2005).

Postsynaptic receptor expression, not presynaptic transmitter availability determines transmitter phenotype.

Glycine/GABA co-release occurs in the cerebellum (Dugué et al., 2005), brainstem (Nabekura et al., 2004; Awatramani et al., 2005) and spinal cord (Jonas et al., 1998). Whether transmitter phenotype is determined by differential glycine/GABA concentrations in presynaptic vesicles (Nabekura et al., 2004) and/or by differential expression of glycine and $GABA_A$ receptors at postsynaptic targets (Dugué et al., 2005) remained unresolved. We find that under conditions where there is equal, if not more GABA than glycine in vesicles, synaptic transmission is predominantly glycinergic

(Figures 1 and 8). Furthermore, direct application of glycine and GABA to postsynaptic cells revealed much larger glycine than $GABA_A$ currents. A fraction of this glycinergic predominance can be explained by the larger (~40%) single channel conductance of glycine over $GABA_A$ receptors (Smith et al., 1989). However, the postsynaptic response to exogenous glycine was 3.5-fold larger than to equimolar GABA, suggesting that an increased density of glycine receptors accounts for the majority of the observed phenotype. The glycine/GABA ratio in the puff experiments was slightly lower than our synaptic estimates with paired recordings. This is not surprising, as puff application will sample both synaptic and extrasynaptic receptors. A high density of extrasynaptic $GABA_A$ receptors, as reported for targets of co-releasing interneurons in the spinal cord (Chéry and de Koninck, 1999), would reduce our synaptic glycine/GABA estimate. We nevertheless observe a 3.5-fold larger glycine than $GABA_A$ component, indicating that receptor expression determines transmitter phenotype in cartwheel cells.

Implications for inhibitory synaptic plasticity

GlyT2 membrane expression and GABA synthesis are subject to regulation by multiple signaling pathways: GlyT2 traffics to and from the plasma membrane on a time-scale of minutes, and this trafficking is regulated by activity-dependent Ca^{2+} influx (Geerlings et al., 2001), protein kinase C (Fornés et al., 2008), and metabotropic purine receptors (Jiménez et al., 2011). Furthermore, GABA synthesis is bi-directionally controlled by PKA and PKC (Wei and Wu, 2008), suggesting that activators upstream of these kinases could potently control cytosolic GABA levels. Together with our current

findings, these results predict that cytosolic transmitter levels potently regulate inhibitory synaptic strength.

Acknowledgments: We thank Michael Bateschell for performing the *in utero* injections; Drs Stephen Smith and Gary Westbrook for comments on the manuscript; Dr. John Brigande and Dan Yaeger for advice regarding the optogenetic experiments; Drs Hai Huang, Kevin Bender, and Sid Kuo, and all members of the Trussell lab for helpful discussions during the course of these experiments. This project was funded by NIH grant R01DC004450 (L.O.T.), Cornelia H. Stevens ARCS scholarship, N.L. Tartar Trust fellowship, and NIH/NIDCD fellowship F31DC012222 (P.F.A.)

Figure 1.1

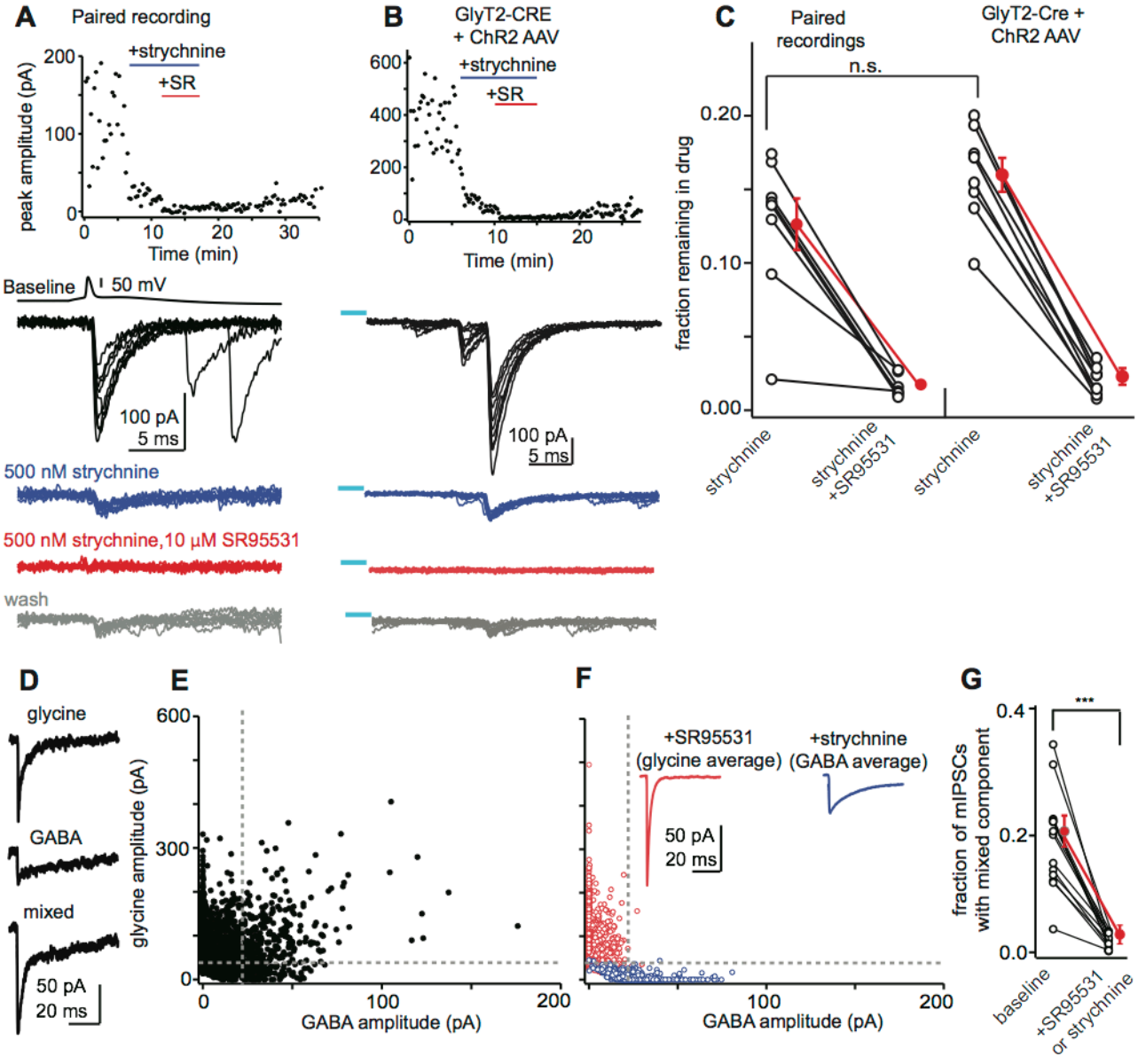
A
Paired recording
+strychnine
+SR
peak amplitude (pA)
Time (min)
B
GlyT2-CRE
+ ChR2 AAV
+strychnine
+SR
Time (min)
C
Paired
recordings
GlyT2-Cre +
ChR2 AAV
n.s.
fraction remaining in drug
strychnine
strychnine
+SR95531
strychnine
strychnine
+SR95531
Baseline
50 mV
100 pA
5 ms
500 nM strychnine
500 nM strychnine,10 µM SR95531
wash
D
glycine
GABA
mixed
50 pA
20 ms
E
glycine amplitude (pA)
GABA amplitude (pA)
F
+SR95531
(glycine average)
+strychnine
(GABA average)
50 pA
20 ms
GABA amplitude (pA)
G
fraction of mIPSCs
with mixed component
baseline
+SR95531
or strychnine

Figure 1.1 Transmission between cartwheel cells is predominantly glycinergic.

(A) Example paired recording between synaptically connected cartwheel cells demonstrating that glycine is the main neurotransmitter at this synapse. The top panel shows IPSC amplitude over time from a single experiment, showing IPSC block by the glycine receptor antagonist strychnine and the $GABA_A$ receptor antagonist SR95531. The lower panel shows traces from this experiment, with a single presynaptic action potential and an overlay of 10 IPSCs evoked during baseline conditions (black), in the presence of 500 nM strychnine (blue), and in the presence of strychnine + 10 μM SR95531. Bottom gray traces show partial recovery of IPSCs during drug washout.

(B) Optogenetic activation of cartwheel cells. In a GlyT2-*cre* mouse injected with a ChR2 AAV virus, wide-field blue light flashes evoked bursts of IPSCs that were mostly blocked by strychnine, similar to paired recordings. Top panel shows a time course of the experiment. Lower panel is example sweeps evoked in different drug conditions. The color scheme is the same as in A. Blue line denotes approximate offset of a 20 ms light stimulus in this experiment.

(C) Summary data plotting the IPSC amplitude remaining in strychnine and SR95531 from paired recordings and optogenetic experiments. The percent block by strychnine was not significantly different between the two data sets, showing that transmission between cartwheel cells is mainly glycinergic. Open circles are individual experiments. Red points are mean ± SEM.

(D) Individual mIPSCs recorded in the absence of inhibitory blockers and in the presence of pentobarbital + zolpidem display a spectrum of decay kinetics and can be classified

into three basic categories: rapidly decaying and predominantly glycinergic events, slowly decaying events mediated by $GABA_A$ receptors, and a third population with both fast glycinergic and slow GABAergic decay components.

(E) The relative amplitude of the glycinergic and GABAergic components of mIPSCs was measured by force-fitting the decay phase of individual events recorded in absence of inhibitory blockers with a double exponential function containing the average glycine and $GABA_A$ decay time constants recorded in the presence of SR95531 or strychnine (Jonas et al., 1998; Awatramani et al., 2005). The amplitude of the slow $GABA_A$ decay is plotted on the x-axis whereas the fast glycine component is plotted on the y-axis. The dashed gray lines represent the 2x S.D. for the amplitudes of glycine and $GABA_A$ decay components, and events falling above the cutoff for both glycine and $GABA_A$ amplitudes were classified as co-releasing glycine/GABA. On average, 19.3±2.2% of events recorded in absence of inhibitory blockers were classified as mixed glycine/GABA mIPSCs (n=14 cells). Data are from two separate cells.

(F) mIPSCs recorded from the same two cells as panel (E), but after the addition of strychnine (blue points) or SR95531 (red points) in one or the other cell. The majority of mIPSCs fell below the 2x S.D. lines after blocking either $GABA_A$ or glycine receptors with SR95531 or strychnine. Inset shows the average glycinergic and GABAergic mIPSC recorded in SR95531 or strychnine, respectively. Note the similarity in kinetics to the pure glycine and GABA events recorded (D).

(G) Summary data from 14 experiments similar to (D-F). Red points are mean ± SEM. Asterisks denote statistical significance at p=0.00001, paired t-test.

Figure 1.2

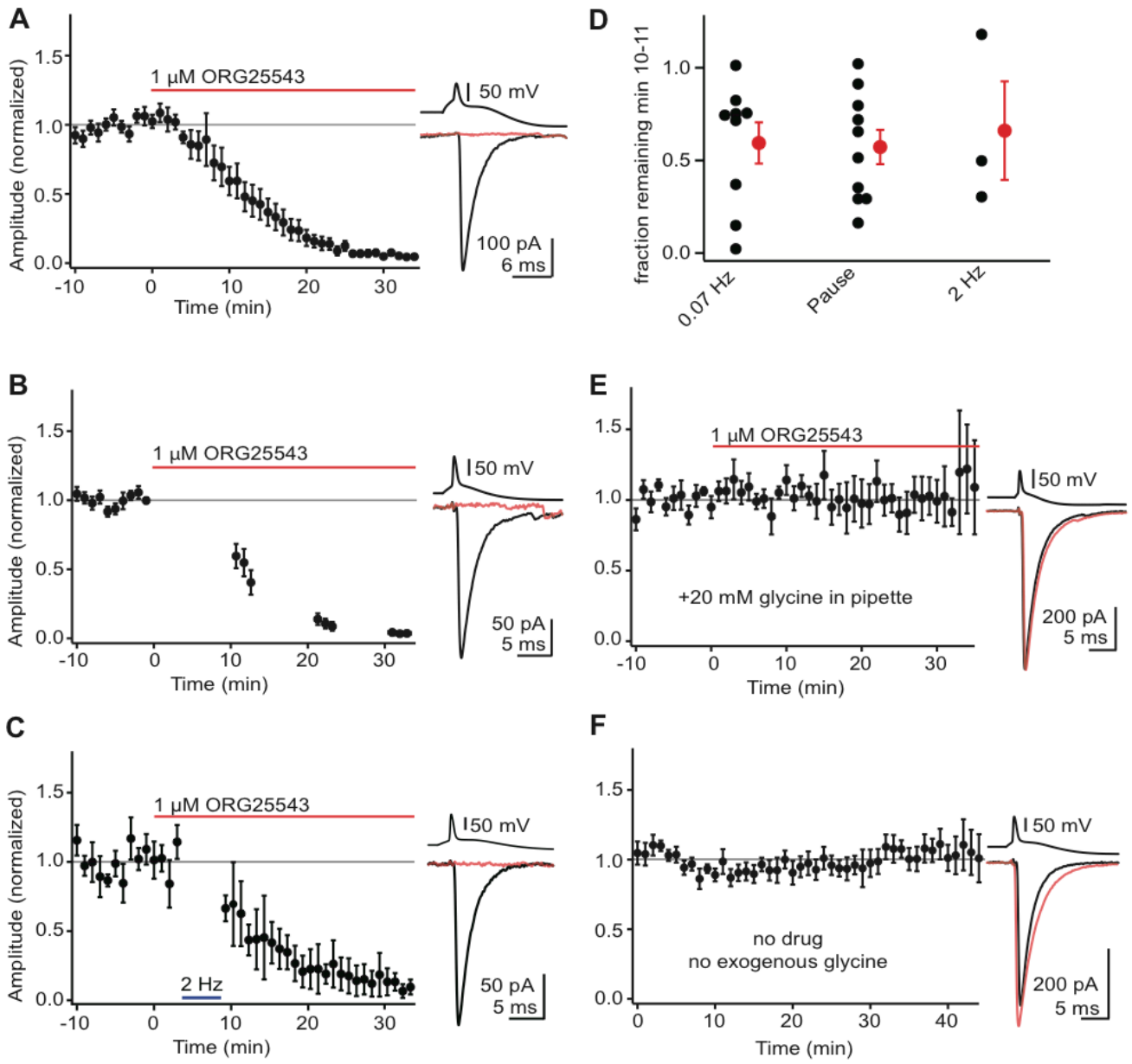
A
1 µM ORG25543
50 mV
100 pA
6 ms
Amplitude (normalized)
Time (min)
B
1 µM ORG25543
50 mV
50 pA
5 ms
Amplitude (normalized)
Time (min)
C
1 µM ORG25543
2 Hz
50 mV
50 pA
5 ms
Amplitude (normalized)
Time (min)
D
fraction remaining min 10-11
0.07 Hz
Pause
2 Hz
E
1 µM ORG25543
+20 mM glycine in pipette
50 mV
200 pA
5 ms
Time (min)
F
no drug
no exogenous glycine
50 mV
200 pA
5 ms
Time (min)

Figure 1.2: GlyT2 supplies the majority of glycine destined for filling of recycling vesicles.

(A-C) Bath application of the GlyT2 inhibitor ORG25543 causes a rapid and near complete run down of glycinergic transmission independently of presynaptic activity. Left: Time course of run down. Each data point is normalized mean ± SEM of 3-9 individual experiments in (A), 8-10 experiments (B), and 2-3 experiments in (C). Right: average of IPSCs from a single experiment evoked during baseline period (black) and after 25-30 min in ORG25543 (red trace). In (A), IPSCs were elicited at 0.07 Hz for the entirety of the experiment. In (B), activity was suspended for the majority of drug application and transmission was periodically tested at ~10 min intervals. The run down in these "minimal activity" experiments was similar to the experiments in panel (A). In (C), presynaptic stimulation frequency was transiently increased from 0.07 Hz to 2 Hz, eliciting between 572 and 600 action potentials during min 3-8 of ORG25543 application. Upon returning to 0.07 Hz stimulation, IPSC rundown was not greater than in experiments from A and B. (D) Summary showing the fraction remaining min 10-11 in experiments from panels A-C. No significant differences were found between the three conditions, demonstrating that presynaptic vesicle content equilibrates with cytosolic transmitter availability independently of exocytosis. Black dots represent values from individual experiments. Red is mean ± SEM.

(E) Adding exogenous glycine to the whole-cell internal solution occluded the run-down caused by GlyT2 block, showing that the ORG25543 effect was specifically due to loss glycine availability in the presynaptic terminal. Right: average IPSCs during baseline

(black) and after 25-30 min in ORG (red). Each time point is the normalized mean ± SEM from 4-6 individual experiments.

(F) Glycinergic transmission remains stable during whole-cell recordings with a glycine-free internal solution, showing that endogenous GlyT2 activity is sufficient to continuously fill synaptic vesicles even during prolonged dialysis. Right: Average IPSCs during min 0-3 (black) and min 35-40 (red). Each time point is the normalized mean ± SEM from 3-7 individual experiments.

Figure 1.3

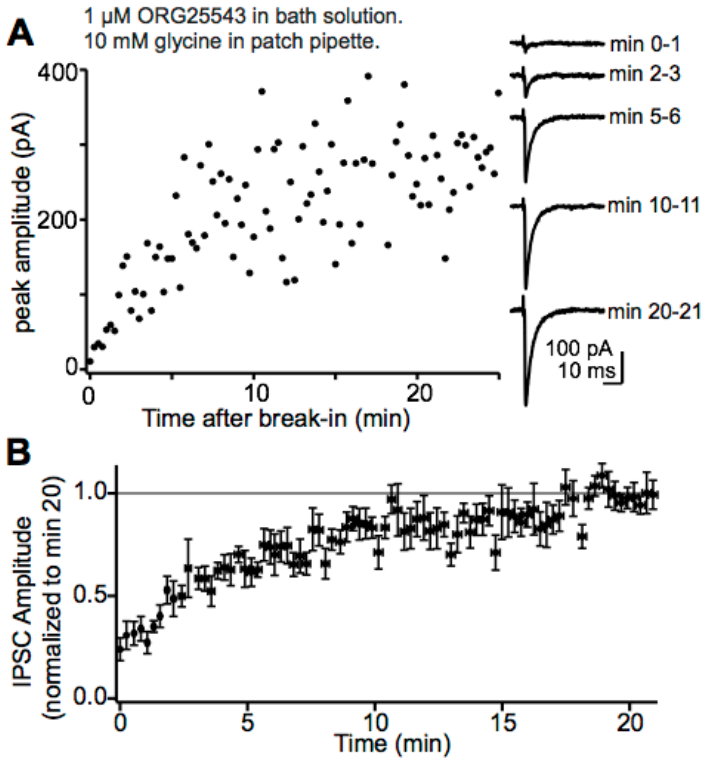

Figure 1.3: Rapid restoration of transmission in glycine-depleted cartwheel cells.

(A) Data from a single experiment where the slice was pre-incubated in 1µM ORG25543 for ~ 2 hours. Glycinergic transmission was isolated with 10 µM SR95531. A pair of cartwheel cells was patched with an internal solution containing 10 mM glycine. Data collection at t=0 began less than 1 min after breaking into the presynaptic cell. IPSC amplitudes rapidly increased during the first 20 min after break in. Right, example IPSCs (average of 4 sweeps per trace) at various times during presynaptic glycine dialysis.

(B) Average time course of transmission run up by presynaptic dialysis of 10 mM glycine in ORG25543-treated slices, similar to the experiment in (A). T=0 begins <2 min after

presynaptic break-in. Data are normalized to the average IPSC amplitude at t=20 min, and each data point is the normalized mean ± SEM of 6-8 individual experiments.

Figure 1.4

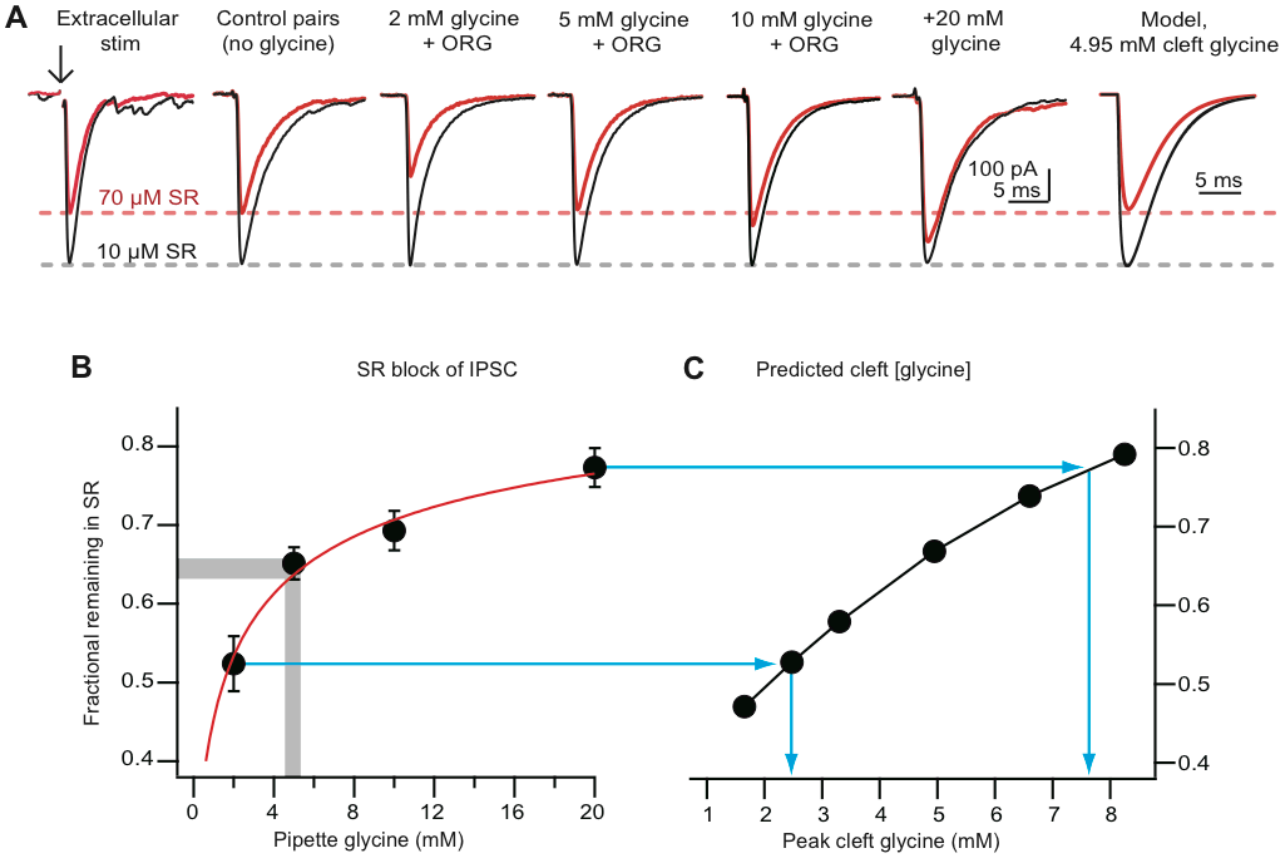

Figure 1.4: GlyT2 supplies ~ 5 mM to presynaptic terminals.

(A) Cytosolic transmitter concentrations determine the degree of vesicle filling. Example average IPSCs evoked during baseline (10 µM SR95531) and after partial block of glycine receptors with 70 µM SR95531 (red traces) under endogenous conditions (control pairs and extracellular stimulation) and in paired recordings with experimentally-determined concentrations of exogenous glycine. Far right trace shows results of a kinetic model for 4.95 mM peak cleft glycine and the relative amplitudes predicted for 10 mM and 70 mM SR95531.

(B) Summary plotting the fraction IPSC remaining in 70 μM SR95531 as a function of pre-synaptic glycine concentration. These values were fit with a standard Hill equation of the form $base + \left(\frac{\max - base}{1 + (x_{half} / x)^{rate}} \right)$. Gray bar brackets range of block seen with control pairs or extracellular stimulation, predicting about 5 mM cytosolic glycine.

(C) A kinetic model (Beato, 2008) was driven with different peak glycine transients and the relative block in 70 mM versus 10 mM was compared, as in panel B. Blue lines connect experimental values in panel B for the range of cytosolic glycine levels used to the corresponding predicted values of cleft glycine in the model.

Figure 1.5

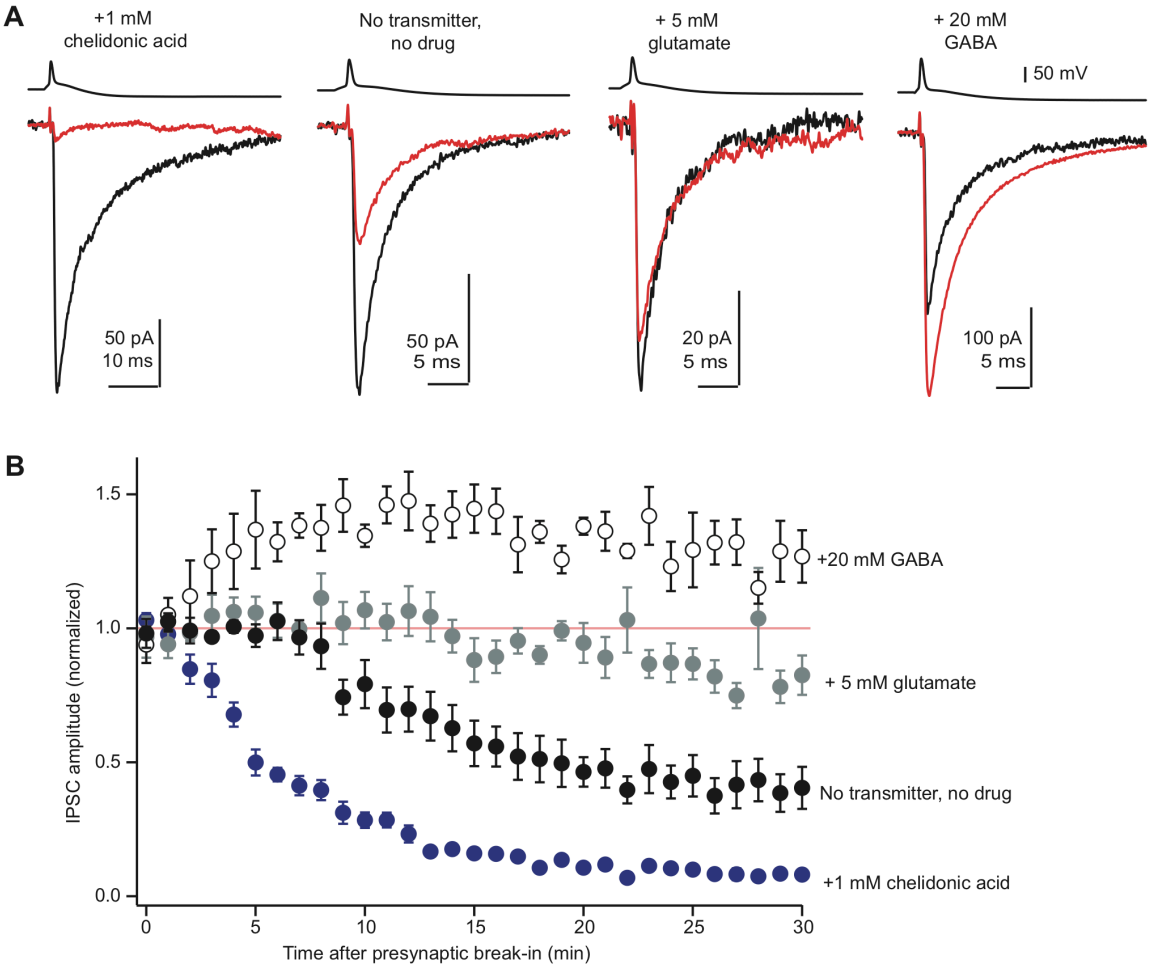

Figure 1.5: GAD supplies the majority of GABA for synaptic vesicles.

(A) Average of $GABA_A$ IPSCs evoked during the first two min after breaking into the pre-synaptic cell (black traces) and after 25-30 min of presynaptic dialysis (red traces). Each pair of red and black traces are from the same individual experiment. Dialyzing presynaptic cells with 1 mM chelidonic acid caused a near complete run down of GABAergic transmission. Prolonged dialysis with a control internal solution caused partial rundown of GABAergic transmission that was reduced by exogenous glutamate, while 20 mM GABA potentiated transmission.

(B) Average time course of experiments shown in panel (A). Each data point is the normalized mean ± SEM of 5-9 individual experiments in each condition.

Figure 1.6

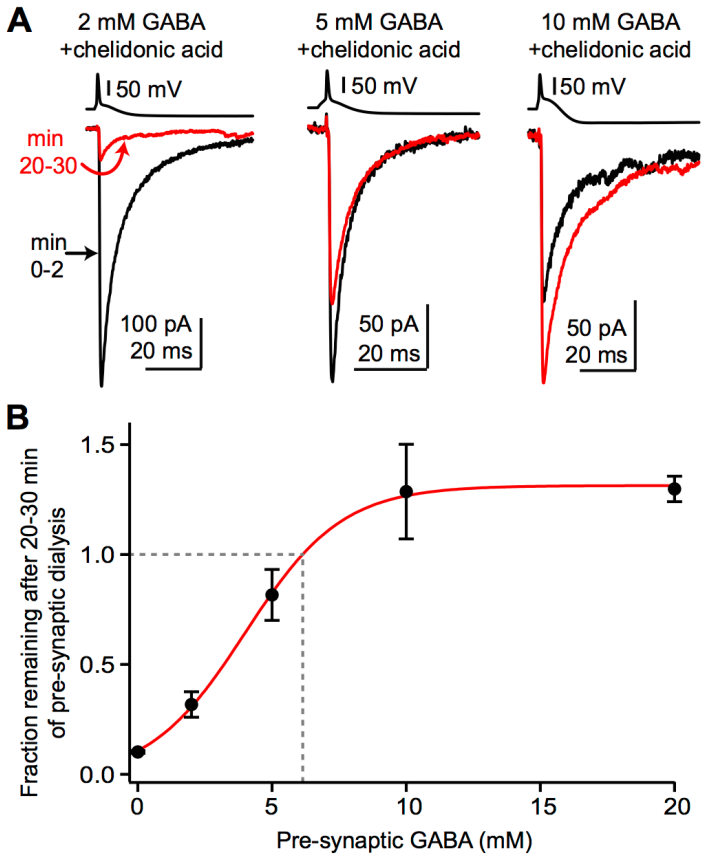

Figure 1.6: GAD supplies millimolar concentrations of GABA.

(A) Average $GABA_A$ IPSCs in single experiments during presynaptic dialysis with chelidonic acid and different concentrations of exogenous GABA. The black trace is an average of IPSCs during the first two min after presynaptic break-in and the red trace is an average of min 20-30. The large hyperpolarization following the presynaptic action potential is due to negative current injection to prevent complex-spike firing.

(B) Fractional IPSC remaining after 20-30 min is plotted against the concentration of exogenous GABA added to the presynaptic pipette solution. Data are normalized to the amplitude of IPSCs recorded during first two min after presynaptic dialysis. The point 0

represents dialysis with chelidonic acid and 0 mM GABA. The 20 mM GABA data are from experiments in Figure 5 where presynaptic cells were loaded with 20 mM GABA and no chelidonic acid. To estimate the GABA concentration needed to prevent run-down (dashed gray line), the data were fit with a sigmoidal function of the form $Baseline+\{YMAX(1+\exp((EC50-C)n))\}$. With C as concentration the fitted parameters were Baseline (starting level of the fit), YMAX (peak), EC50 (concentration at half maximal run-down) and n (slope factor). For the solid red line these parameters were 0.02, 1.34, 4.01 mM and 1.8. This equation was also used for jackknife analysis of the data set as described in the text.

Figure 1.7

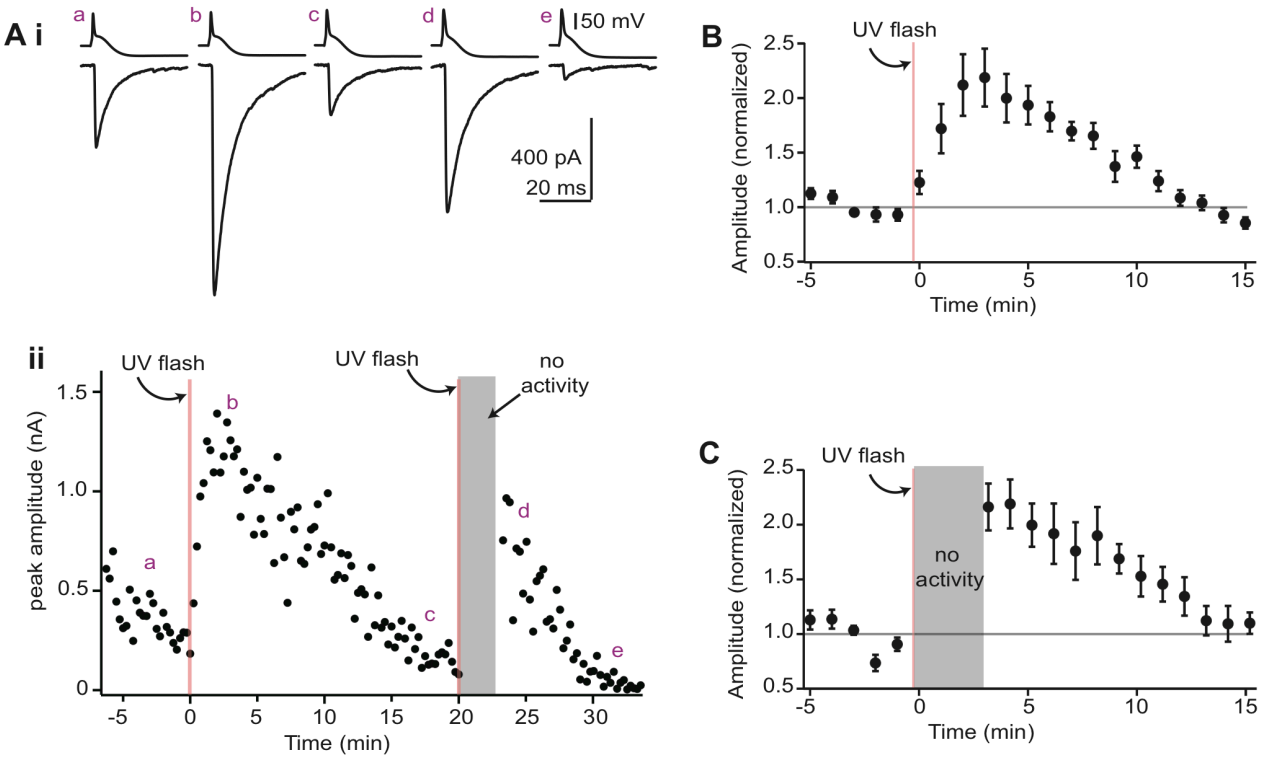

Figure 1.7: Vesicles re-equilibrate with cytosolic transmitter within one minute and independently of activity.

(A) Time course of $GABA_A$ IPSC amplitudes (bottom) and average traces at different time points (top) from a recording with 5 mM MNI-caged glutamate added to the presynaptic internal solution. Presynaptic whole-cell recording began ~10 min prior to data collection. Uncaging glutamate by wide-field UV flash (500 ms; red line) rapidly potentiated GABAergic transmission. At the ~20 min mark, presynaptic activity was suspended and glutamate was uncaged a second time. Presynaptic activity resumed 3 min after uncaging, and IPSC amplitudes were similarly potentiated.

(B-C) Average time course of the uncaging effect in experiments where IPSCs were continuously evoked after uncaging (B) or in experiments where presynaptic activity was suspended during uncaging (C). Each data point is the normalized mean ± SEM of 11-12 individual experiments (B) or 6-9 experiments (C).

Figure 1.8

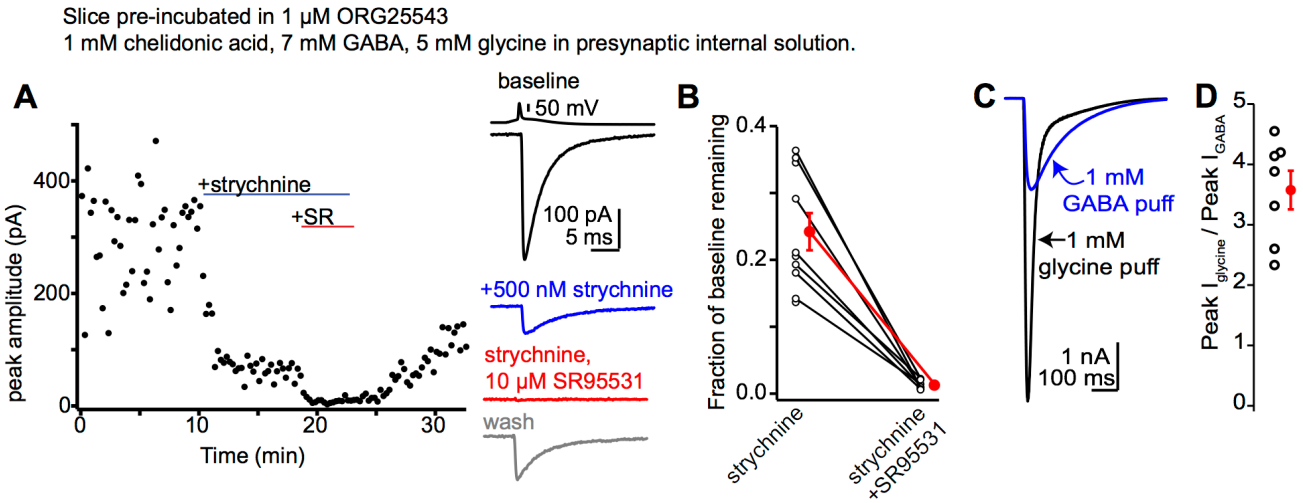

Figure 1.8: Postsynaptic receptor density determines IPSC phenotype.

(A) Presynaptic cartwheel cells loaded with 5 mM glycine + 7 mM GABA recapitulate the endogenous, predominantly glycinergic IPSC phenotype. Slices were pre-incubated in ORG25543 and cartwheel cells were patched with an internal solution containing 5 mM glycine, 7 mM GABA, and 1 mM chelidonic acid. The left panel is a time course from a single experiment plotting IPSC amplitude over time, showing that IPSCs evoked under these conditions are predominantly blocked by the glycine receptor antagonist strychnine. The traces on the right show a single presynaptic action potential and average IPSCs from this experiment during the baseline period (black, no inhibitory blockers), in strychnine (blue), and in strychnine + SR95531 (red). Gray trace is partial recovery during drug washout.

(B) Summary data plotting the fractional IPSC remaining in the presence of strychnine and strychnine + SR95531. Open circles are individual experiments. Red circles denote mean ± SEM. Data are normalized to the average IPSC amplitude during baseline.

(C) Puff application (10 ms, 5 psi) of 1 mM glycine or GABA to the same cell reveals that post-synaptic glycine currents are ~3-fold larger than $GABA_A$ currents. Traces are averages from a single experiment.

(D) Summary of puff-evoked glycine/$GABA_A$ current ratios in 7 cells similar to panel (C). Open circles are individual experiments. Red dot represents mean ± SEM of these data.

CHAPTER 2: CHEMICAL SYNAPTIC TRANSMISSION ONTO SUPERFICIAL STELLATE CELLS OF THE DORSAL COCHLEAR NUCLEUS

Pierre F. Apostolides[1,2] & Laurence O. Trussell[2]

[1]Neuroscience Graduate Program

[2]Vollum Institute & Oregon Hearing Research Center, Oregon Health & Science University. Portland, Oregon, 97239, USA.

This chapter was submitted as a research article to the *Journal of Neurophysiology* on November 17th, 2013.

Abstract

The dorsal cochlear nucleus (DCN) is a cerebellum-like auditory brainstem region whose functions include sound localization and multisensory integration. While previous *in vivo* studies show that glycinergic and GABAergic inhibition regulate the response properties of several DCN cell types in response to sensory stimuli, data regarding the synaptic inputs onto DCN inhibitory interneurons remain limited. Using acute DCN slices from P15-P24 mice, we examined the properties of excitatory and inhibitory synapses onto the superficial stellate cells, a poorly understood cell class in the DCN. Excitatory synapses onto stellate cells activated both NMDA receptors and fast-gating, Ca^{2+}-permeable AMPA receptors. Inhibition onto superficial stellate cells was mediated by glycine and $GABA_A$ receptors with different temporal kinetics. Paired recordings revealed that superficial stellate cells make reciprocal synapses and autapses, with a connection probability of ~18-20%. Unexpectedly, superficial stellate cells co-released both glycine and GABA, suggesting that co-transmission may play a role in fine-tuning the duration of inhibitory transmission.

Introduction

The dorsal cochlear nucleus (DCN) is a mammalian auditory brainstem region composed of diverse neuronal cell types (Oertel and Young, 2004). Although the contribution of the DCN to auditory processing is not clear, previous studies suggest that it may be involved in sound localization in the vertical plane and orientation of the head towards sounds of interest (Davis and Young, 2000; May, 2000). Interestingly, the local circuitry of the DCN closely resembles that of the cerebellum and cerebellum-like nuclei found in mammals and fish (Oertel and Young, 2004) and this homology suggests that the DCN may also function to generate "negative images" of predictable auditory input, thereby filtering out self-generated sounds (Bell et al., 2008; Requarth and Sawtell, 2011).

Regardless of the precise role of the DCN in auditory processing, previous studies have established that the glutamatergic efferent neurons (fusiform and giant cells) integrate auditory information from the ear with sensory input from non-auditory brain regions (Oertel and Young, 2004). Sound information is relayed via auditory nerve fibers synapses on the basal dendrites of fusiform cells, whereas non-auditory information enters via an array of cerebellum-like, granule cell parallel fibers that synapse onto fusiform cell apical dendrites. DCN parallel fibers also contact two types of molecular layer interneuron: glycinergic, Purkinje-like cartwheel cells, and GABAergic superficial stellate cells (henceforth “stellate cells”) that closely resemble the stellate/basket cells of the cerebellum (Wouterlood et al., 1984; Mugnaini, 1985; Bell et al., 2008).

Previous studies show that parallel fibers recruit feedforward glycinergic inhibition onto fusiform cells, presumably mediated by cartwheel cells (Davis et al., 1996; Davis

and Young, 1997; Kanold and Young, 2001; Roberts and Trussell, 2010; Kuo and Trussell, 2011; Doiron et al., 2011). Given that even a single cartwheel cell can control the firing rate of fusiform cells (Roberts and Trussell, 2010), these findings imply that feedforward inhibition from interneurons potently gates whether the DCN relays signals to downstream targets. Interestingly, *in vivo* work suggests that GABAergic inhibition also controls the response properties of cartwheel and fusiform cells (Davis and Young, 2000), and a recent *in vitro* study suggested that GABAergic inhibition controls the spread of parallel fiber excitation in the DCN (Middleton et al., 2011). Since cartwheel cell transmission is predominantly glycinergic (Golding and Oertel, 1997; Roberts et al., 2008; Mancilla and Manis, 2009; Apostolides and Trussell, 2013a), these results suggest that stellate cells are a likely source of GABAergic inhibition.

However, little is known about chemical synaptic transmission onto DCN stellate cells. This lack of information is surprising, as stellate cells are common components of the outer layers of the DCN (Wouterlood et al., 1984) and may share homology with the stellate and basket cells known to be crucial for controlling the output of the cerebellar cortex (Callaway et al., 1995; Barmack and Yakhnitsa, 2008; Oldfield et al., 2010; Coddington et al., 2013). Therefore, a comparison of cerebellar and DCN stellate cell properties might provide clues to DCN function. Nevertheless, there are no confirmed *in vivo* recordings from DCN stellate cells, and *in vitro* recordings are few (Zhang and Oertel, 1993; Golding and Oertel, 1997; Apostolides & Trussell 2013b). We performed whole-cell recordings from visually identified DCN stellate cells in acute mouse brain slices and examined the properties of excitatory and inhibitory synapses. We find that similar to cerebellar stellate/basket cells, parallel fibers activate fast, Ca^{2+}-permeable

AMPA receptors on DCN stellates. Unlike cerebellar stellate cells (Clark and Cull-Candy, 2002), however, single parallel fibers activated both AMPA and NMDA receptors. We also find that DCN stellate cells inhibit one another via reciprocal synapses as well as autapses. While it has been previously suggested that DCN stellate cells were GABAergic, we found that they express the glycine transporter GlyT2 required for functional glycinergic transmission (Gomeza et al., 2003; Rousseau et al., 2008), and most stellate cells tested co-released both glycine and GABA. Our findings shed light on the synaptic properties to DCN stellate cells, highlighting significant functional similarities and differences between the DCN and the cerebellum.

Methods

Slice Preparation

All protocols involving animals were approved by OHSU's Institutional Animal Care and Use Committee. Mice P15-P24 days of age of wild-type (C57/Bl6 or CBA), GlyT2-GFP, or GAD65-GFP background were used for these experiments. Mice were anesthetized with isofluorane, decapitated, and slices (200-250 μm thick) containing the DCN were cut in an ice-cold sucrose solution containing (in mM): 87 NaCl, 25 NaHCO3, 25 glucose, 75 sucrose, 2.5 KCl, 1.25 NaH2PO4, 0.5 CaCl2, 7 MgCl2, and bubbled with 5% CO2/95% O2. After cutting, slices were allowed to recover for 30-45 min at 34o C in an artificial cerebrospinal fluid (ACSF) solution containing (in mM): 130 NaCl, 2.1 KCl, 1.7 CaCl2, 1 MgSO4, 1.2 KH2PO4, 20 NaHCO3, 3 Na-HEPES, 10-12 glucose, bubbled with 5% CO2/95% O2 (300-310 mOsm). This solution was used as the standard perfusate

for all experiments. In some experiments 5 μM R-CPP or 50 μM D-APV were added to the cutting solution and/or recovery chamber. After recovery, slices were maintained at ~22o C until recording. Experiments were typically performed within 5 hours of slice preparation.

Electrophysiology

Slices were mounted in a recording chamber and continuously perfused at 3-5 ml/min with ACSF heated to 31-33o C. Neurons were visualized using Dodt contrast optics with a 40x or 63x objective on a Zeiss Axioscop2 microscope. For paired recordings, the pipette internal solution contained 60 K-gluconate, 10 K-glutamate, 70 KCl, 4.8 MgCl2, 4 ATP, 0.5 GTP, 10 Tris-phosphocreatine, 0.1-0.2 EGTA, 10 HEPES, pH adjusted between 7.2-7.3 with KOH (~290 mOsm). For recording miniature events and broadening action potentials in figure 7, K-gluconate, K-glutamate and KCl were replaced by 120 mM CsCl. For evoked and spontaneous EPSC recordings, the internal contained (in mM) 118 CsMeSO3, 5 TEA-Cl, 5 QX314-Cl, 5 Cs4-BAPTA, 10 HEPES, 4 Mg-ATP, 0.5 GTP, 10 Tris-Phosphocreatine. In some experiments, 30 mM CsFl was substituted for equimolar CsMeSO3.

Whole-cell recording pipettes (final resistance: 2.5-5 MOhm) were made from boroscillicate glass (#8250, World Precision Instruments) using a Narishige P97 puller. Parallel fibers were stimulated by delivering voltage pulses (50-200 μs) through a theta glass pipette filled with ACSF positioning within 20-40 μm of the cell. Series resistance in voltage-clamp (<30 MOhm) was monitored frequently and compensated 60-80%

'correction', 90% 'prediction' (bandwidth=3 kHz) and data were not analyzed if series resistance varied >20-25% over the course of the recording.

Identification of stellate cells

Most experiments were performed using wild-type mice. Stellate cells were identified by their location in the slice (at the outer edge of the molecular layer and below the ependymal surface) and basic membrane properties. The main types of neurons found in the DCN superficial molecular layer are stellate and cartwheel cells (Wouterlood et al., 1984; Osen and Mugnaini, 1981). Stellate cells were easily distinguished from cartwheel cells by the size of their soma and input resistance which typically differed by an order of magnitude (Apostolides & Trussell, 2013b). In experiments with transgenic mice, GFP fluorescence was observed with a 100W Hg bulb placed in the epi-fluorescence port of the microscope and passed through a GFP filter set.

Data Acquisition and Analysis

Traces were recorded with a Multiclamp 700B amplifier and a Digidata 1322A analog-digital converter board using pClamp 9 software. Signals were low-pass filtered at 10-20 kHz and digitized at 20-50 kHz. Data were analyzed offline after filtering the traces at 2-10 kHz. For voltage-clamp data, all measurements were made on the peak amplitude of averaged traces unless otherwise stated. Spontaneous and miniature events were detected using a template algorithm or amplitude threshold in Axograph X or Clampfit, and each event was visually inspected for false positives or malformed events. Decay kinetics were measured on averages of aligned events with a single, double, or

triple exponential function. Weighted decay time constants were calculated from double exponential fits were calculated as:

$$\frac{(A_{slow} * \tau_{slow}) + (A_{fast} * \tau_{fast})}{A_{slow} + A_{fast}}$$

All values are reported as mean ± SEM. Statistical significance was determined using paired or unpaired Student's t-tests where appropriate.

Histology

Mice were transcardially perfused with warm (38°C) 100mM PBS solution, pH 7.4, followed by ice-cold 4% paraformaldehyde in PBS. The brains were dissected from the skull and incubated overnight in 4% paraformaldehyde for complete tissue fixation. Next the brains were rinsed in PBS and brainstem coronal sections were acquired at 30 μm on a vibratome (VT1000S, Leica). After sectioning, the tissue was washed in PBS solution for 30 minutes. Sections were then incubated for 1 hour in block solution (2% goat serum, 0.2% Triton X-100 (in PBS), 0.3% BSA) and subsequently incubated overnight at 4°C with anti-GFP, rabbit polyclonal antibody, Alexa Fluor 488 conjugate (1:200 in block solution, Invitrogen Molecular Probes). Next day, sections were washed in PBS for 1 hour and mounted on 0.3% gelatin coated slides. After drying, sections were dehydrated in ascending alcohols, and delipidized in xylenes. The tissue was then rehydrated and coverslipped using Fluoromount G medium (Southern Biotechnology Associates). Fluorescence images were acquired using a confocal microscope (Olympus FV1000) by sequential scanning of GFP signals using an oil-immersion objective (60×,

numerical aperture 1.42) with Olympus Fluoview-1000 software. Image analysis was conducted using NIH ImageJ software.

Reagents

NBQX, APV, CPP, SR95531 were purchased from Ascent Scientific/Abcam. Strychnine was purchased from Sigma-Aldrich.

Results

Single parallel fibers activate AMPA and NMDA receptors

Previous studies in cerebellar stellate/basket cells showed that excitatory postsynaptic currents (EPSCs) evoked by parallel fiber stimulation lack a prominent NMDA receptor component (Glitsch and Marty, 1999). Consequently, NMDA receptors on cerebellar stellate cells are thought to be extra-synaptic and primarily activated by glutamate spillover during sustained activity of multiple parallel fibers (Carter and Regehr, 2000; Clark and Cull-Candy, 2002). We tested whether NMDA receptors were similarly excluded from postsynaptic sites in DCN stellate cells by evoking EPSCs while voltage-clamping the cell at negative or positive potentials. All recordings were performed in 10 μM SR95531 and 0.5-2 μM strychnine to block $GABA_A$ and glycine receptors, respectively. Single parallel fiber shocks from a bipolar stimulating electrode (0.5-6 V), delivered while the cell was held at -67 to -77 mV, evoked fast EPSCs typical of AMPA receptor-mediated transmission (Fig. 1A, lower trace). By contrast, EPSCs at +33 mV displayed a prominent slow component (Fig. 1A, upper trace) that was blocked by the selective NMDA receptor antagonist R-CPP (5 μM, n=6 cells; Fig. 1B). NBQX (10 μM)

blocked the fast EPSC component (n=5 cells; Fig. 1C), confirming that it was mediated by AMPA receptors.

However, even relatively weak shocks employed in these experiments likely activated more than one presynaptic parallel fiber (Roberts and Trussell, 2010). It could be argued that pooling of glutamate from even a few closely spaced synapses, or the repetitive activation of single parallel fibers (Isope et al., 2004; Nahir and Jahr, 2013), might suffice to activate high-affinity, extrasynaptic NMDA receptors. We therefore tested whether NMDA receptors were activated by single parallel fibers by analyzing spontaneous EPSCs occurring due to random firing of presynaptic granule cells. At +33 mV, spontaneous EPSCs displayed a prominent slow component similar to evoked EPSCs (Fig. 1D). The decay phase of these events was best fit with the sum of two or three exponentials, with an average weighted decay time constant of 36.2±6.3 ms (n=8 cells). 5 μM R-CPP or 50 μM D-APV selectively blocked the slow decay component, thereby reducing the weighted decay time constant to 1.8±0.2 ms (Fig. 1E,F; n=8, $p<0.001$, paired t-test). However, NMDA receptor antagonists had minimal effect on the peak amplitude of spontaneous events (Fig. 1F. baseline: 26.3±2.1 pA, NMDA blockers: 21.5 ±3.4 pA, n=8, p=0.20). Together these results show that, in contrast to cerebellar stellate/basket cells, AMPA and NMDA receptors are co-localized at parallel fiber synapses in DCN stellate cells.

DCN stellate cells contain fast, Ca^{2+}-permeable AMPA receptors.

Cerebellar stellate cells express Ca^{2+}-permeable, GluA2-lacking AMPA receptors with sub-millisecond decay kinetics (Liu and Cull-Candy, 2000; Carter and Regehr, 2002; Jackson and Nicoll, 2011). Interestingly, previous studies in the cochlear nuclei found that the biophysical properties of AMPA receptors correlate with the identity of the presynaptic terminal: AMPA receptors at auditory nerve synapses have rapid kinetics and are typically Ca^{2+}-permeable, whereas AMPA receptors at parallel fiber synapses gate slowly and are impermeable to Ca^{2+} (Gardner et al., 1999; Gardner et al., 2001). Thus, we asked whether DCN stellate cells contained Ca^{2+}-permeable AMPA receptors with rapid kinetics similar to cerebellar stellate cells, or if their AMPA receptor properties followed the pattern proposed by (Gardner et al., 2001).

We first quantified the kinetics of synaptic AMPA receptors by recording miniature EPSCs (mEPSCs) in DCN stellate cells. D-APV, SR95531, and strychnine were added to the bath solution to isolate AMPA mEPSCs, and 1 μM tetrodotoxin (TTX) was added to block spikes. Quantal events typically ranged in amplitude between 20 and 200 pA, with an average amplitude of 45.2±6.5 pA, a 10-90% rise time of 0.17±0.01 ms, and a weighted decay time constant of 0.71±0.07 ms (n=12 cells). Data from an example cell are shown in Figure 2A, with the corresponding amplitude histogram of individual events shown in 2B. mEPSCs could exceed 200 pA, which, given the high input resistance of stellate cells (Apostolides & Trussell 2013b) would make even small synapses relatively potent. These amplitude and kinetic values are similar to those reported in cerebellar stellate/basket cells (Carter and Regehr, 2002; Crowley et al., 2007), and suggest that

AMPA receptors on DCN stellate cells might lack the GluA2 subunit and be Ca^{2+}-permeable (Liu and Cull-Candy, 2000; Jackson and Nicoll, 2011).

We further tested for expression of Ca^{2+}-permeable AMPA receptors by evoking EPSCs with a stimulating electrode while voltage clamping stellate cells at different holding potentials. Ca^{2+}-permeable AMPA receptors exhibit an inward rectification due to intracellular polyamine block at positive potentials, while GluA2-containing AMPA receptors are Ca^{2+}-impermeable and have a linear current-voltage (IV) relationship (Isaac et al., 2007). AMPA EPSCs were isolated with D-APV/SR95531/strychnine and exogenous polyamines (spermine, 100 μM) were added to the pipette internal solution. Parallel fibers were stimulated 3 times at 100 Hz (delivered once every 10-15 s) while holding the postsynaptic cell between -50 and +50 mV. AMPA EPSCs exhibited paired-pulse facilitation, typical of parallel fiber synapses in the DCN (Tzounopoulos et al., 2004; Kuo and Trussell, 2011; Fig. 2C): The amplitude of the third EPSC at -50 mV was on average 6.28±0.56 times larger than the first EPSC (n=12 cells). As expected from Ca^{2+}-permeable AMPA receptors, the IV curve of EPSCs showed significant inward rectification (Fig. 3C, D). We calculated a "rectification index" (RI) for each cell, defined as the actual EPSC amplitude recorded at +50 mV divided by the value extrapolated from a linear fit of EPSCs recorded at negative potentials. 10 of 12 DCN stellate cells tested exhibited significant inward rectification (RI=0.58±0.05, $p<0.0001$, one sample t-test; Fig 2E,F), and rectification was absent when EPSCs were recorded without exogenous polyamines added to the pipette solution (RI=1.06±0.06, n=6, p=0.5; (Kamboj et al., 1995); Fig 2F). Thus, inward rectification was due neither to poor voltage-clamp at positive potentials, nor to the activation of glutamatergic synapses on electrically-coupled

neurons (Apostolides & Trussell, 2013b). The degree of inward rectification we observed was comparable to that that reported in rat cerebellar stellate cells (Liu and Cull-Candy, 2000; Soto et al., 2007). Given the low release probability of parallel fiber synapses, we measured the final EPSC in a train of 3 parallel fiber stimuli delivered at 100 Hz. This analysis may therefore underestimate the degree of inward rectification if the receptors experienced use-dependent unblock by spermine (Rozov and Burnashev, 1999). However, paired-pulse facilitation was not significantly different between EPSCs recorded at negative and positive potentials (EPSC3/EPSC1 at -50 mV was 6.27±0.47 versus 6.79±0.93 at +50 mV; p=0.47, paired t-test), suggesting that any use-dependent unblock of GluA2-lacking receptors occurring during these short trains was negligible.

Stellate cells are GABA/glycine co-releasing interneurons.

DCN stellate cells receive inhibitory inputs both from cartwheel cells and other stellate cells (Manis et al., 1994; Wouterlood et al., 1984). While cartwheel cells are dual GABA-glycinergic neurons (Roberts et al., 2008; Apostolides and Trussell, 2013a), previous immunohistochemical and anatomical studies suggested that stellate cells are GABAergic interneurons (Wouterlood et al., 1984; Mugnaini, 1985). Indeed, in order to train ourselves to recognize these tiny neurons for patch clamping in thick brain slices, we initially utilized a mouse line in which GFP expression was driven by the promoter for GAD65 (Hughes et al., 2005), a synthetic enzyme for GABA. In the DCN molecular layer in this mouse line, small cells could be observed lying close to the ependymal layer, with numerous fine processes extending towards the cell body layer (Fig 3A), consistent with superficial stellate cells. Labeled small cells are also very common in the molecular

layer of the cerebellum of this mouse (not shown). However, we were surprised that small cells can also be readily observed in a mouse line (Zeilhofer et al., 2005) in which GFP expression is driven by the promoter for GlyT2, a marker of glycinergic neurons (Fig 3B). These observations suggested that inhibition by stellate cells may be mediated by both GABA and glycine.

GABAergic and glycinergic transmission onto stellate cells

We therefore quantified the amplitude and kinetics of GABAergic and glycinergic miniature inhibitory postsynaptic currents (mIPSCs). $GABA_A$ mIPSCs were isolated with 10 μM NBQX, 50 μM D-APV, 500 nM strychnine and 1 μM TTX. The decay phase of averaged $GABA_A$ mIPSCs were fit by the sum of two exponentials (Fig. 4A). The fast component decayed with a time constant 2.2±0.1 ms and represented 82±2% of the total amplitude, whereas the slow component decayed with a time constant of 9.8±1.3 ms. The weighted decay time constant for $GABA_A$ mIPSCs was 3.4±0.2 ms (n=12 cells). $GABA_A$ mIPSCs had an average amplitude of 44.4±7.1 pA and a 10-90% rise time of 0.24±0.01 ms (n=9).

Glycine mIPSCs (isolated with NBQX, D-APV and SR95531) were prevalent in all cells tested and had an average amplitude of 42.9±5.5 pA and a 10-90% rise time of 0.17±0.01 ms (n=14). The decay of glycine mIPSCs was fit with a double exponential function in 13/14 cells, whereas one cell was best fit by a single exponential. Similar to $GABA_A$ mIPSCs, glycinergic events were dominated (72±6% of total amplitude) by a fast decay time constant of 1.1±0.1 ms and a minor slow component of 3.6±0.2 ms

(n=14). The average weighted decay time constant for glycine mIPSCs was 1.7±0.2 ms (Fig. 4B). Glycine mIPSCs rose significantly faster than GABAA events ($p<0.001$, unpaired t-test). Furthermore, both fast and slow decay components were significantly faster for glycinergic compared to $GABA_A$ mIPSCs ($p<0.01$, unpaired t-test), although the relative weighting of fast vs. slow did not differ significantly ($p=0.19$). The peak amplitude of the glycine and $GABA_A$ mIPSCs did not differ significantly ($p=0.82$). Figures 4C and 4D show amplitude histogram for GABA and glycine mIPSCs recorded in two different cells. These results show that stellate cells receive similarly potent glycinergic and GABAergic inhibition, albeit with different temporal kinetics. These results do not however indicate whether these different events arose from cartwheel cell or stellate cell synaptic terminals.

Unitary synaptic and autaptic connections in DCN stellate cells

Previous anatomical studies suggested reciprocal synaptic connections between DCN stellate cells (Mugnaini, 1985), in agreement with the connectivity profile of stellate/basket cells of the cerebellum (L Palay and Chan-Palay, 1974). We searched for reciprocal connections by making paired recordings from neighboring DCN stellate cells. Similar to reports on cerebellar stellate cells (Kondo and Marty, 1998), we found that 11/60 (18.3%) of attempted stellate connections (each pair = 2 connections) were synaptically coupled. An example pair is shown in Figure 5A. The presynaptic cell was held in voltage clamp and action potentials were elicited at 10 Hz by voltage steps from -70 to +5 mV for 100 μs (top trace). Five consecutive sweeps from the postsynaptic cell are shown in black, and an average of these sweeps is shown in red. Interestingly, a

similar proportion of cells also displayed a prominent autaptic connection (19/89 cells tested, 21.3%), observed as an IPSC arising after evoking an escaping action potential in the recorded neurons, thus highlighting another parallel between the DCN and cerebellar stellate cells (Pouzat and Marty, 1998). An example autaptic recording is shown in Figure 5B. The top traces are an overlay of 20 consecutive sweeps (4 failures) evoked at 0.5 Hz in black, with an average of successes in red. The transmission probability in this recording was 83.9% (131/156 successes). The lower traces in Figure 5B are 20 consecutive sweeps (black) and average (red) after the addition of 10 μM SR95531, showing that this current was predominantly due to GABA release. Figure 5C plots the amplitude of autaptic events from the recording in Figure 5B as a function of time as the $GABA_A$ receptor blocker was added. Overall, transmission fidelity was highly variable between connections, with success probability ranging from 16.8% to 100% when IPSCs were evoked at 0.5-1 Hz (mean rate of successes (ie, when an IPSC followed a presynaptic spike) was 56±9%, n=6 autapses and 4 paired recordings).

SR95531 blocked the majority of transmission in 7 unitary connections (5 autapses and 2 paired recordings). In some recordings, we noticed a small residual IPSC in SR95531, which together with the GlyT2 expression described above, suggests that DCN stellate cells co-release glycine. Due to the high failure rate of these connections, however, it was impossible to determine whether these IPSCs originated specifically from the stellate cell of interest, or if these were spontaneous glycinergic IPSCs coincidently originating from another presynaptic neuron. We therefore repeated the pharmacological experiments in stellate cells loaded with a CsCl-rich internal solution. By blocking K+ currents that would normally repolarize presynaptic action potentials,

intracellular Cs^+ should enhance exocytosis, thereby increasing the absolute IPSC size and reducing the variability of unitary IPSCs (Vincent and Marty, 1996). Under these conditions, autaptic IPSCs showed almost no failures (Fig. 6A). Bath application of 10 μM SR95531 reduced the peak IPSC to 29±7% of baseline (n=13 cells). In 11/13 experiments, a significant SR95531-insensitive component remained and this component was subsequently blocked by 0.5-1 μM strychnine (Fig. 6B). Thus, glycine and GABA are functionally co-released from DCN stellate cells. Although transmission was mostly mediated by GABA and $GABA_A$ receptors in the majority of experiments, there was a significant variability in percentage of transmission mediated by glycine in the grouped data (Fig. 6B).

Activating fusiform cells generates GABA and glycinergic IPSCs in stellate cells.

We sought another method for determining the transmitter phenotype of stellate cells that would avoid the dialysis of presynaptic neurons which may alter the effectiveness of inhibitory transmission (Apostolides and Trussell, 2013a). The approach is based upon the recent demonstration that stellate cells are electrically coupled to fusiform principal cells, and that optogenetic activation of fusiform cells leads to action potentials in stellate cells (Apostolides & Trussell 2013b). This provides a means for selectively activating presynaptic stellate cells without doing presynaptic recordings. We therefore recorded from stellate cells in transgenic mice expressing channelrhodopsin2 in glutamatergic fusiform cells (Apostolides & Trussell 2013b; Thy1-ChR2 line 18: Arenkiel et al., 2007 and VGluT2-ChR2: Hägglund et al., 2010). Stellate cells were recorded with a cesium-based internal solution and voltage-clamped between 0 and +40 mV to establish an

outward Cl- driving force. Pulses of blue light delivered to the slice often led to electrically conducted photocurrents and spikelets, as previously shown. However, we noticed that holding the stellate cell at positive potentials for extended periods (>5 min) of recording weakened the gap-junction mediated events on the recorded cell, leaving only chemical transmission. This enabled us to record IPSCs in stellate cells generated by the neighboring still-coupled stellate cells. Blue light pulses led to vigorous bursts of IPSCs (Fig 7A). We determined the transmitter phenotype of stellate cells by using an event detection to overlay and average individual IPSCs evoked under baseline conditions and in the presence of $GABA_A$ receptor blockers. GABA-glycine co-transmission was evident in 10/12 cells tested: SR95531 reduced the peak amplitude of average IPSCs to 47±10% of baseline (range: 20-80% remaining in SR95531. n=6 and n=4 in Thy1-ChR2 and VGluT2-ChR2 mice, respectively). In two cells, SR95531 completely abolished light evoked IPSCs (1 cell from each genotype). The fraction remaining in SR95531 in these experiments was not significantly different from the CsCl-filled autapses (p=0.45, unpaired t-test). Together with the results of Figures 3 and 6, these data show that DCN stellate cells co-release GABA and glycine from autaptic and reciprocal synaptic connections.

Discussion

We have examined chemical synaptic transmission onto DCN stellate cells, contrasting the results with known properties of synapses onto cerebellar stellate cells. While general parallels exist between these two types of interneuron in terms of GABAergic phenotype, subtype of AMPA receptors and existence of gap junctions (see

Apostolides & Trussell 2013b), several differences were apparent, notably in NMDA and glycine receptor activation. Given the kinetic properties of these receptors, our results suggest that the time course of synaptic excitation and inhibition may be quite different in stellate cells of the two regions.

Glutamate receptors on DCN stellate cells are Ca^{2+}-permeable

We observed that NMDA and AMPA receptors in DCN stellate cells could be activated by single stimuli to parallel fibers. This contrasts with cerebellar molecular layer interneurons, where the NMDA component of parallel fiber EPSCs is small (Glitsch and Marty, 1999; Clark and Cull-Candy, 2002) and is primarily recruited by glutamate spillover during intense presynaptic activity (Carter and Regehr, 2000; Clark and Cull-Candy, 2002; Nahir and Jahr, 2013). However, similar to cerebellar stellate cells, intracellular polyamines cause inward rectification of current-voltage relations for AMPA receptor EPSCs, indicating the presence of GluA2-lacking, Ca^{2+}-permeable AMPA receptors. Thus, single action potentials in granule cells may activate two types of glutamate-gated, Ca^{2+}-permeable conductances on DCN stellate cells, mediated by AMPA and NMDA receptors. DCN parallel fiber synapses onto cartwheel and fusiform cells are differentially depressed or potentiated by similar patterns of Ca^{2+} influx through NMDA receptors during spike-timing dependent plasticity (Tzounopoulos et al., 2004; Tzounopoulos et al., 2007). The presence of Ca^{2+}-permeable AMPA receptors, which lack the outward rectification endowed by voltage-dependent Mg^{2+} block of NMDA receptors, suggests the possibility that parallel fiber plasticity rules in DCN stellate cells

may be distinct from those previously described in cartwheel and fusiform cells (e.g. Lamsa et al., 2007). Moreover, the submillisecond decay kinetics of stellate cell AMPA receptors contrast sharply with the properties of AMPA receptors at parallel fiber synapses onto cartwheel cells and the apical dendrites of fusiform cells (Gardner et al., 1999; Gardner et al., 2001), suggesting that similar patterns of parallel fiber activity will result in cell-type specific spike output.

Inhibitory transmission is mediated by glycine and GABA

Glycinergic and GABAergic mIPSCs had similar amplitudes but different time courses, suggesting that the potency of both transmitter systems is approximately equal, but also that the temporal profiles of inhibition may differ in a transmitter-specific manner. Based on labeling of small superficial cells similar to the ones we routinely record from, DCN stellate cells probably express the plasma membrane glycine transporter GlyT2, which transports glycine from the extracellular space into the nerve terminal for subsequent vesicular packaging (Gomeza et al., 2003; Rousseau et al., 2008). Most DCN stellate cells tested co-released glycine and GABA, although transmission was predominantly mediated by $GABA_A$ receptors. This suggests that stellate cells release more GABA than glycine, or alternatively, that postsynaptic $GABA_A$ receptors are more abundant and/or have higher conductance than glycine receptors. Although our data do not distinguish between these possibilities, cartwheel cells of the DCN appear to maintain a largely glycinergic phenotype through a preponderance of glycine receptors rather than a mismatch in GABA/glycine synthesis (Apostolides and Trussell, 2013a).

Stellate cells probably also receive inhibitory inputs from cartwheel cells (Manis et al., 1994), and we have occasionally noticed large IPSC bursts typical of the cartwheel cell's "complex spike" firing pattern (data not shown; Golding and Oertel, 1997; Roberts et al., 2008). Thus, some proportion of glycine and $GABA_A$ mIPSCs in our data sets likely originate from cartwheel as well as stellate cell synapses.

Function of DCN stellate cells

A recent study from (Middleton et al., 2011) demonstrated that in a mouse model of tinnitus, brain slices made from acoustically traumatized mice exhibited enhanced spread of electrical activity through the DCN molecular layer, apparently due to reduced GABAergic control of excitation. Given that GABA is the primary transmitter of stellate cells, it may be that reduced activity of stellate cells or their synapses may underlie this cellular correlate of tinnitus, and this possibility highlights the need to clarify how stellate cells function within the context of molecular layer circuitry. Indeed, the three targets of parallel fibers, stellate cells, cartwheel cells and fusiform cells, together form a remarkably sophisticated, interacting network. Cartwheel cells provide powerful inhibition to fusiform cells (Roberts and Trussell, 2010), with synapses targeting near the fusiform soma (Rubio and Juiz, 2004). Stellate cells, given their size and position, primarily reach the distal portions of fusiform dendrites (Apostolides and Trussell, 2013b), and probably distal regions of cartwheel dendrites as well. It is therefore possible that they serve to locally control excitation by parallel fibers in those distal compartments. However, the recent observation that fusiform cells communicate to

stellate cells via gap junctions suggests a model in which fusiform cell activity, triggered either by parallel fibers or auditory nerve, is carried back into the molecular layer by stellate cells (Apostolides and Trussell, 2013b). The inhibitory synapses stellate cells make onto one another and onto other cell types, as well as the gap junctions between stellate cells, may provide a mechanism for distributing these 'retrograde' signals from fusiform cells in complex ways throughout the molecular layer. Further understanding of how such signals are processed will require clarifying the organization of these cell types with respect to the tonotopic axis and the subtypes of modalities represented by parallel fiber activity.

Acknowledgements: Funding was provided by NIH grant R01DC004450 (L.O.T.), Cornelia H. Stevens ARCS scholarship, N.L. Tartar Trust fellowship, and NIH/NIDCD fellowship F31DC012222 (P.F.A.). We thank Carolina Borges-Merjane for preparing sections from GFP mice used for the confocal imaging in Figure 3, as well as Michael Bateschell and Ruby Larisch for help with mouse colony management.

Figure 2.1

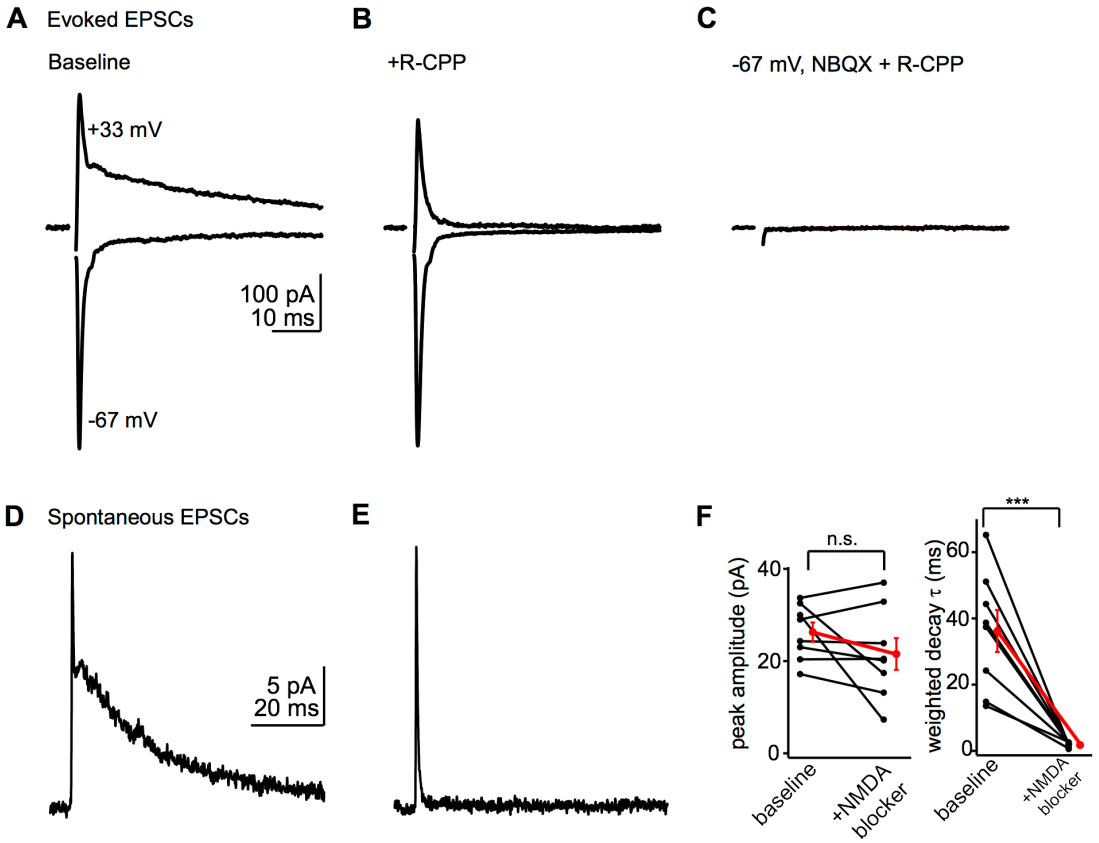

Figure 2.1: Parallel fibers activate AMPA and NMDA receptors.

A) Example average EPSCs recorded in a stellate cell at negative (lower trace) and positive (upper trace) holding potentials. Of note is the slow decay component at +33 mV, typical of NMDA receptor-mediated transmission.

B) In the same cell, bath application of the NMDA receptor antagonist R-CPP (5 μM) selectively blocks the slow component.

C) Subsequent application of the AMPA receptor blocker NBQX (10 μM) abolishes the fast EPSC.

D) Average of spontaneous EPSCs recorded at +33 mV, highlighting a slow component similar to evoked EPSCs. Different cell from the one shown in panels A-C.

E) Average of spontaneous EPSCs recorded at +33 mV in the presence of R-CPP, showing that the slow decay is due to NMDA receptor activation.

F) Quantification of 6 experiments similar to panels D-E. Left panel shows the peak amplitudes of average spontaneous EPSCs before and after NMDA receptor blockade, indicating that NMDA receptors contribute minimally to the peak. The rightmost panel shows the effect of NMDA receptor blockers on the weighted decay time constant of spontaneous EPSCs. Black lines connect data from individual experiments, red dot is mean ± SEM. Asterisks denote statistical significance.

Figure 2.2

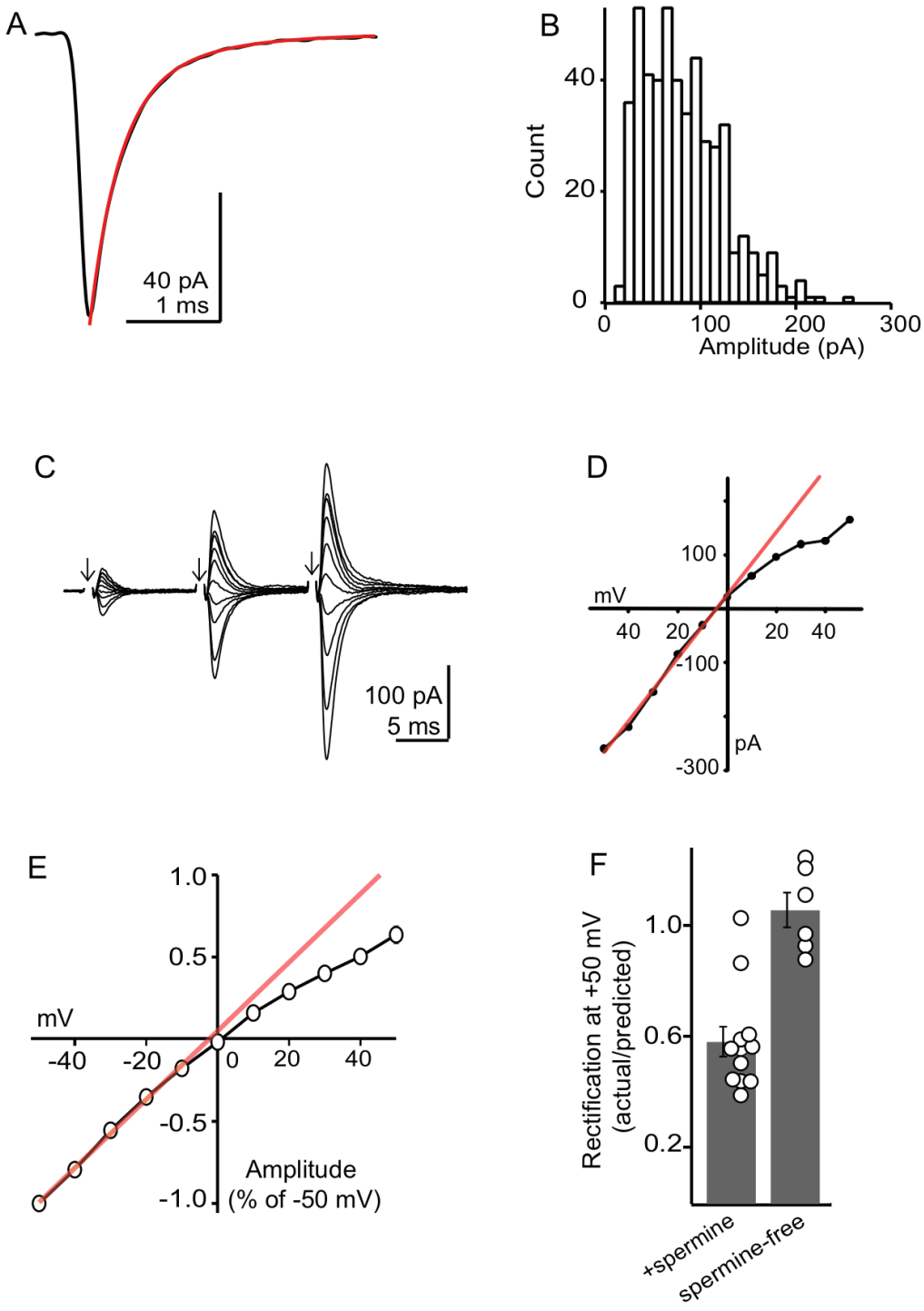
A
40 pA
1 ms
B
Count
40
20
0
0
100
200
300
Amplitude (pA)
C
100 pA
5 ms
D
100
mV
40
20
20
40
-100
pA
-300
E
1.0
0.5
mV
-40
-20
0
20
40
-0.5
-1.0
Amplitude
(% of -50 mV)
F
Rectification at +50 mV
(actual/predicted)
1.0
0.6
0.2
+spermine
spermine-free

Figure 2.2: AMPA receptors are Ca^{2+}-permeable.

A) Example average mEPSC from a DCN stellate cell. The decay phase is fit with a double exponential decay (weighted decay t = 0.42 ms).

B) Amplitude histogram of individual mEPSCs from the same cell as in (A).

C) Example average EPSCs evoked at different holding potentials. Arrows denote time of parallel fiber stimulation. The shock artifact is blanked for clarity.

D) IV curve for the third EPSC in the example traces shown in (A). The red line is a linear fit to the data recorded at negative holding potentials.

E) Summary IV curve for 12 cells, normalized to the amplitude at -50 mV. Error bars are generally smaller than the symbols.

F) Group data showing the rectification index of individual stellate cells. Note that all cells recorded with a spermine-free internal solution displayed a linear IV.

Figure 2.3

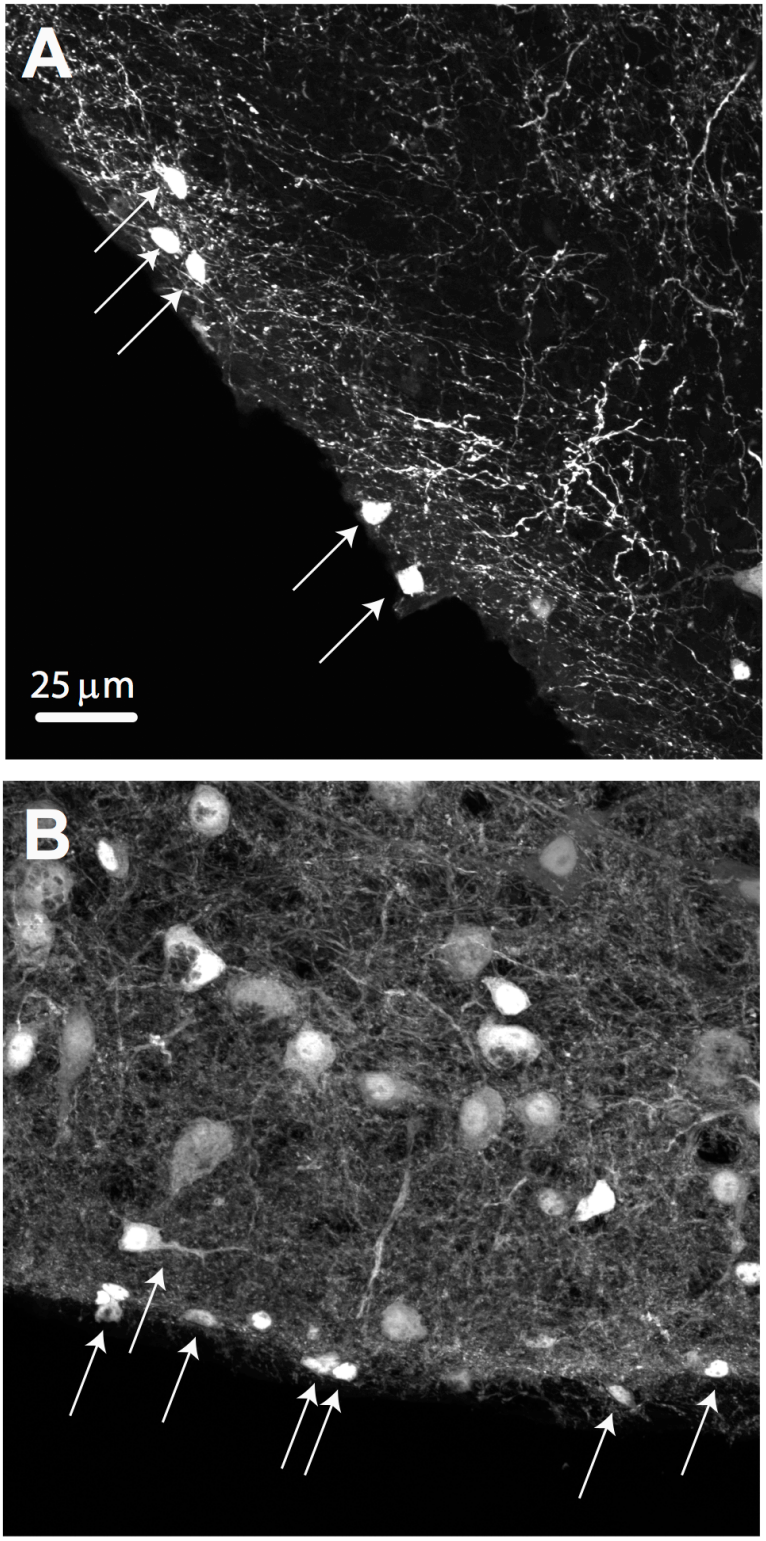

Figure 2.3: Stellate cells express molecular markers of GABA/glycine co-releasing interneurons.

A) Photomicrograph of the DCN in a GAD65-GFP mouse, showing that stellate cells express the GABA synthesizing enzyme GAD65. Arrows point to stellate cells located at the ependymal edge of the DCN.

B) Photomicrograph of the DCN in a section from a GlyT2-GFP mouse. Arrows point to small labeled neurons at the ependymal edge of the brainstem, suggesting that stellate cells also express the plasma membrane transporter required for functional glycine release. The larger neurons in the DCN molecular layer are presumably cartwheel cells, while the intense background indicates a high density glycinergic fibers throughout the DCN.

Figure 2.4

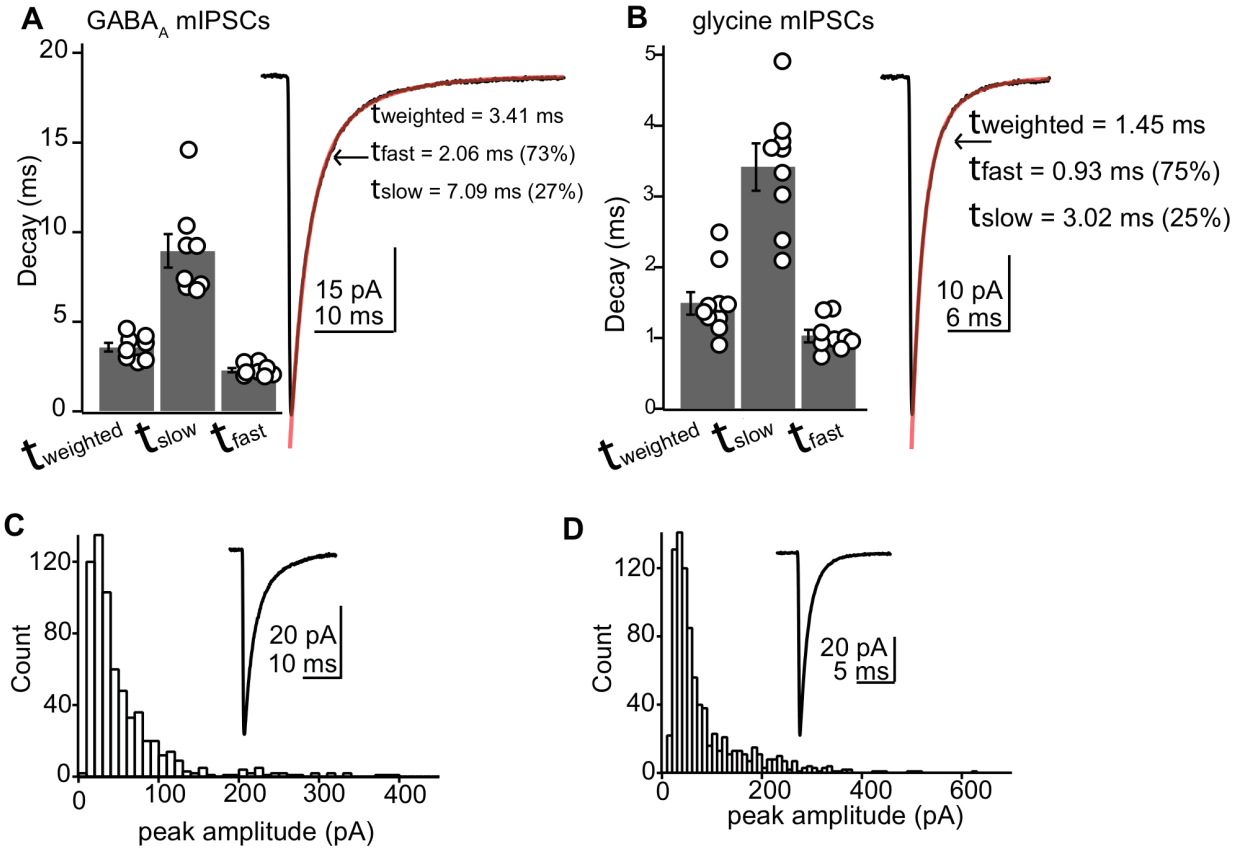

Figure 2.4: Inhibition is mediated by glycine and GABA

A) Left: Summary data showing the distribution of fast, slow, and weighted decay time constants for average $GABA_A$ mIPSCs. Right, example average $GABA_A$ mIPSC. Red curve is the double exponential fit to the decay phase. Rate constants for the fit were: t-fast, 2.1 ms (73%), t -slow 7.1 ms (27%), weighted t, 3.41 ms.

B) Histogram showing the amplitude distribution of $GABA_A$ mIPSCs from a single cell. Right,: example average mIPSC from this cell. Rate constants for the fit were: t- fast, 0.9

ms (75%), t-slow 3.0 ms (25%), weighted t, 1.5 ms. These data are from a different cell than that shown in panel A.

C) Same as panel A, but for glycine mIPSCs.

D) Same layout as panel B, but for glycine mIPSCs. The data are from a different cell as panel C.

Figure 2.5

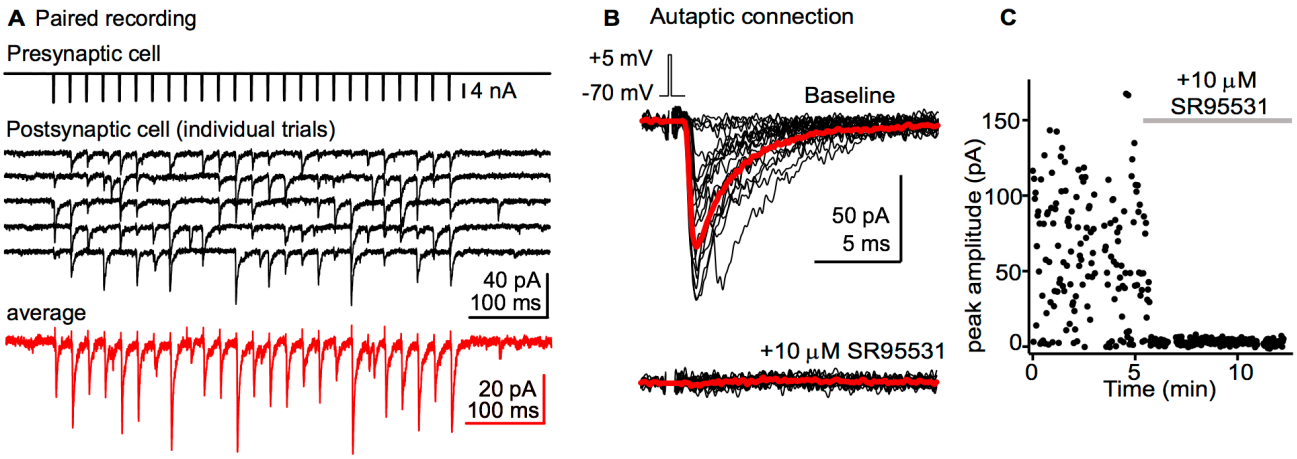

Figure 2.5: reciprocal synaptic connections and autapses in DCN stellate cells.

A) Example recording of a synaptically coupled pair of stellate cells. The presynaptic cell (upper trace) is held in voltage clamp and escaping spikes were triggered by short voltage steps. Middle black traces are four consecutive sweeps showing time-locked IPSCs in a postsynaptic stellate cell. Lower red trace is an average of multiple trials from this cell. These experiments were performed in the presence of NBQX/R-CPP to block AMPA and NMDA receptors. IPSCs are inward due to a high Cl- internal solution.

B) Example autaptic IPSCs from a stellate cell. Black traces are individual trials, red trace is an average of successful transmission events. Lower trace is after bath application of SR95531. The escaping spike artifact was removed by digitally subtracting an average of transmission failures from these traces.

C) Time course of the experiment shown in panel (B)

Figure 2.6

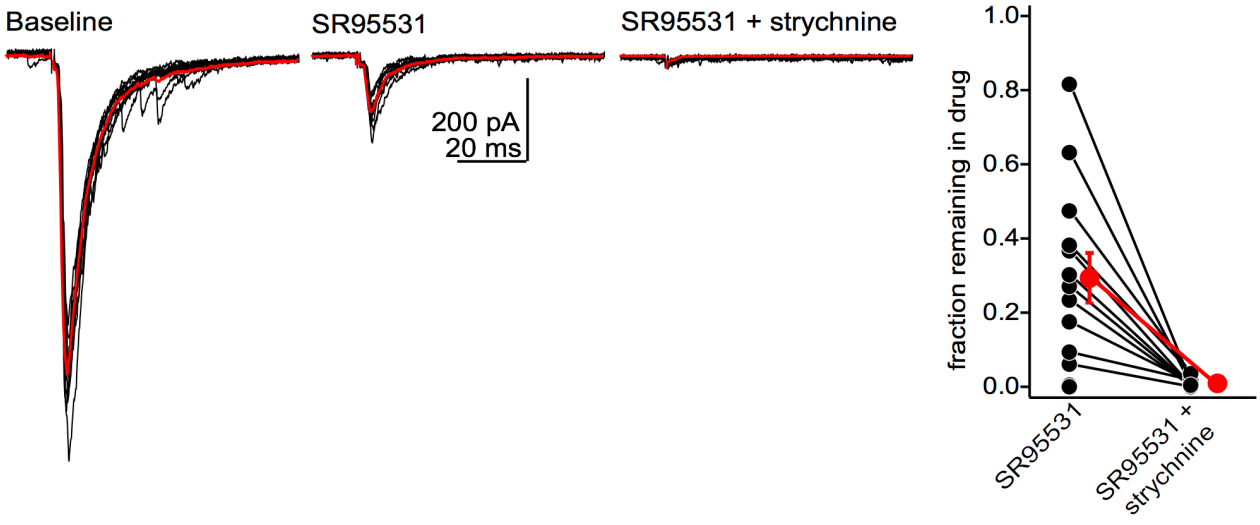

Figure 2.6: Stellate cells co-release GABA and glycine

A) Example traces from a stellate cell filled with a CsCl internal solution. Black traces are individual sweeps, red trace is an average of sweeps in each individual condition. SR95531 blocks the majority of the autaptic IPSC in this cell. The remaining component is blocked by strychnine.

B) Summary data showing the fraction of IPSC (normalized to a baseline period) remaining after the addition of SR95531 and strychnine. Notice the spread of data points, with some cells displaying no glycine component, whereas some were predominantly glycinergic.

Figure 2.7

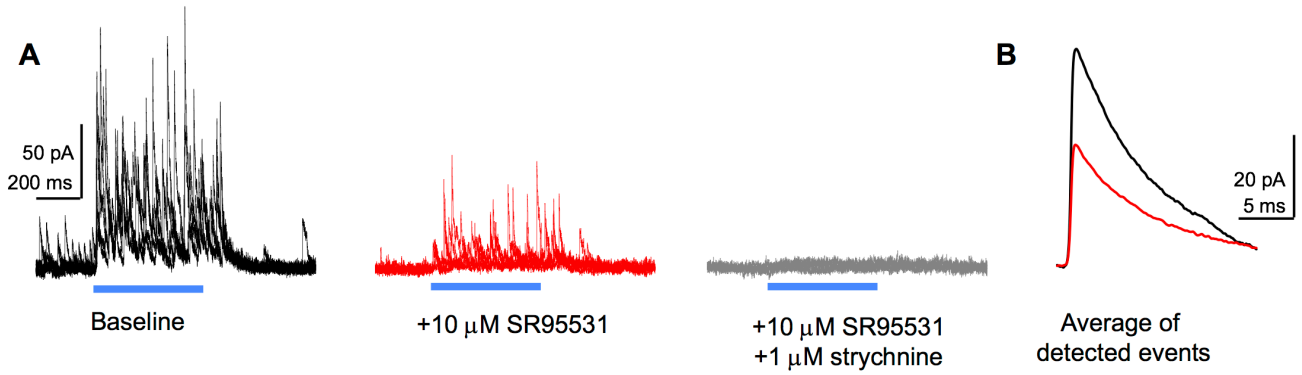

Figure 2.7: Reciprocal connections between neighboring stellate cells are also mixed GABA/glycinergic.

A) Example experiment from a Thy1-ChR2 mouse. The stellate cell is held at +33 mV and fusiform cells are activated by blue light stimuli (500 ms) denoted by the blue bar. Four example sweeps are shown superimposed, recorded in baseline (black), SR95531 (red), and SR95531 + strychnine (gray).

B) Average of IPSCs in baseline (black) and SR95531 (red) detected with a template algorithm. Data are from the same cell as in panel (A).

CHAPTER 3: REGULATION OF INTERNEURON EXCITABILITY BY GAP JUNCTION COUPLING WITH PRINCIPAL CELLS

Pierre F. Apostolides[1,2] & Laurence O. Trussell [2]

[1]Neuroscience Graduate Program

[2]Vollum Institute & Oregon Hearing Research Center, Oregon Health & Science University, Portland, Oregon, 97239, USA

This chapter appeared as an article in *Nature Neuroscience* (December, 2013 (16):1764-1772)

Abstract

Electrical coupling of inhibitory interneurons can synchronize activity across multiple neurons, thereby enhancing the reliability of inhibition onto principal cell targets. It is unclear whether downstream activity in principal cells controls the excitability of such inhibitory networks. Using paired patch-clamp recordings, we show that the excitatory projection neurons (fusiform cells) and inhibitory stellate interneurons of the dorsal cochlear nucleus form an electrically coupled network via connexin36-containing gap junctions. Remarkably, stellate cells were more strongly coupled to fusiform cells than to other stellate cells. This heterologous coupling was functionally asymmetric so as to bias electrical transmission from principal cell to interneuron. Optogenetically-activated populations of fusiform cells reliably enhanced interneuron excitability and generated GABAergic inhibition onto postsynaptic targets of stellate cells, whereas deep afterhyperpolarizations following fusiform spike trains potently inhibited stellate cells over several hundred milliseconds. Thus, the excitability of an interneuron network is bi-directionally-controlled by distinct epochs of activity in principal cells.

Introduction

Cerebellum-like structures are present in most vertebrates and may act as adaptive filters of ongoing sensory information, thereby reducing the salience of predictable sensory input patterns (Bell et al., 2008; Dean et al., 2010; Requarth and Sawtell, 2011). To this end, the principal efferent neurons of these circuits integrate two types of excitatory synapses: "Instructive" signals from a specific sensory modality and "predictive" signals from other brain nuclei that convey the multisensory context in which the instructive signal occurred. Although these basic anatomical motifs are conserved across most cerebellum-like structures, the cellular mechanisms and local computations underlying the adaptive filtering of sensory information remain poorly understood (Bell et al., 2008).

The dorsal cochlear nucleus (DCN) is an auditory brainstem region thought to function as an adaptive filter to cancel predictable, self-generated sounds (Oertel and Young, 2004; Requarth and Sawtell, 2011). Similar to other cerebellum-like structures, the DCN is divided into instructive and predictive pathways which converge upon principal neurons (Bell et al., 2008; Requarth and Sawtell, 2011), an anatomical layout that implies that auditory and multisensory information are processed by largely non-overlapping circuits. The glutamatergic principal neurons (termed fusiform or pyramidal cells) integrate sound frequency information from tonotopically-organized, auditory nerve synapses with multisensory signals relayed by granule cell parallel fibers (Figure 1a). The parallel fiber pathway also recruits two types of inhibitory interneurons in the circuit's molecular layer: Purkinje-like cartwheel cells and superficial stellate cells that are analogous to the stellate/basket cells of the cerebellum (Oertel and Young, 2004).

Although fusiform cells receive convergent excitation from multisensory parallel fibers and the auditory nerve, the inhibitory stellate and cartwheel interneurons of the molecular layer only receive parallel fiber input. This suggests that while multisensory signals may filter auditory inputs by recruiting interneurons to modify fusiform cell spiking (Roberts and Trussell, 2010), auditory nerve synapses do not directly control the activity of molecular layer interneurons.

We find that the GABAergic stellate interneurons of the molecular layer are electrically-coupled to the excitatory fusiform cells that integrate auditory and multisensory inputs. This novel circuit motif is surprising, as electrical coupling in the brain occurs primarily between inhibitory neurons of the same anatomical and functional class (Bennett and Zukin, 2004; Hestrin and Galarreta, 2005). These heterologous electrical synapses showed directional asymmetry, thereby favoring transmission from the auditory to the multisensory processing domains. Accordingly, the functional consequences of electrical coupling were such that stimulating auditory nerve synapses onto fusiform cells reliably depolarized stellate cells, and fusiform cell activity was sufficient to generate robust inhibition in the multisensory pathway. Our data significantly revise the connectivity map of DCN, and show that at the first synapses of the central auditory system, interneuron excitability is temporally controlled by the activity of projection neurons via electrical synapses.

Methods

DCN brain slice preparation

All procedures involving animals were approved by OHSU's Institutional Animal Care and Use Committee. C57/BL6 wild-type mice postnatal 15-32 days were used for the majority of the experiments. For optogenetic experiments, mice were B6.Cg-Tg(Thy1-COP4/EYFP)18Gfng/J (Thy1-ChR2; Jax stock # 007612) or C57Bl/6-TG(Slc17a6-COP4*H134R/EYFP)2OKi/J (VGluT2-ChR2; Jax stock # 017978). Mice were anesthetized by isofluorane inhalation, followed by decapitation, and 200-250 μm coronal DCN slices were cut in a cold sucrose solution containing (in mM) 87 NaCl, 25 $NaHCO_3$, 25 glucose, 75 sucrose, 2.5 KCl, 1.25 NaH_2PO_4, 0.5 $CaCl_2$, 7 $MgCl_2$, and bubbled with 5% CO_2/95% O_2. After cutting, slices recovered for 30-45 min at 34^o C in an ACSF solution containing (in mM) 130 NaCl, 2.1 KCl, 1.7 $CaCl_2$, 1 $MgSO_4$, 1.2 KH_2PO_4, 20 $NaHCO_3$, 3 Na-HEPES, 10-12 glucose, bubbled with 5% CO_2/95% O_2 (300-310 mOsm). In some experiments, 5 μM R-CPP, 50 μM D-APV or 5 μM MK801 were added to the slice and recovery solutions. After recovery, slices were kept at room temperature (~22 C^o) until recording.

For DCN slices from mature animals, P54-P63 mice were anesthetized with an i.p. injection of 2% Avertin, transcardially perfused and the brain sliced in a chilled solution containing (in mM) 93 NMDG, 2.5 KCl, 1.2 NaH_2PO_4, 30 $NaHCO_3$, 20 HEPES, 10 $MgSO_4$, 0.5 ascorbic acid, 2 thiourea, 3 Na-pyruvate, 25 Glucose, 0.5 $CaCl_2$, 0.005 MK801, 12 n-acetyl-l-cysteine, 300-310 mOsm, pH adjusted to 7.3-7.4 with HCl (Zhao et al., 2011). Slices recovered at 34^o C in NMDG-based solution for 10-15 min followed by a 40-60 min recovery period at room temperature in standard ACSF.

Electrophysiology

Slices were transferred to a recording chamber and continuously perfused at 3-4 ml/min with ACSF heated to 32-34 C^o by an inline heater. Neurons were visualized by Dodt contrast optics with a 40x objective. Chemical synaptic transmission was blocked in most experiments in Figures 1-3 and 5-7 by adding (in μM) 10 NBQX, 5 R-CPP (or 50 D-APV or 5 MK801), 0.5-2 strychnine, 5-10 SR95531. 0.5-1 TTX was sometimes added to experiments in Figure 1 and Supplemental Figures 3 and 4 to stop spontaneous firing. For experiments in Figures 4d-e, NBQX and R-CPP were omitted to enable activation of auditory nerve synapses. Fusiform cells were identified by previously published criteria (Roberts and Trussell, 2010; Kuo and Trussell, 2011). Superficial stellate cells were identified by their location at the ependymal edge of the DCN molecular layer and soma size (Wouterlood et al., 1984). Stellate cells could be easily distinguished from cartwheel cells by their smaller soma located at the ependymal edge of the DCN, stronger I_h sag upon hyperpolarization, and significantly higher input resistances (stellate: 996 ± 139 MOhm, n=29. Cartwheel: 50 ± 4 MOhm, n=12, p=0.0001, unpaired t-test). In addition, 30 μM Alexa488 (or 20 μM Alexa594) was added to the pipette solution in many experiments to visualize the somatodendritic morphology. The pipette solution for most current- and voltage-clamp experiments contained (in mM) 113 K-gluconate, 4.8 $MgCl_2$, 4 ATP, 0.5 Tris-GTP, 14 Tris-phosphocreatine, 0.1 EGTA, 10 HEPES, pH 7.25 with KOH, ~290 mOsm. In some experiments in Figure 1, 15.5 KCl was substituted for equimolar K-Gluconate. For IV curves in Figure 9, the internal solution contained (in mM) 64.5 $CsMeSO_3$, 30 CsFl, 5 TEA-Cl, 5 QX314-Cl, 5 Cs_4BAPTA, 4.8 $MgCl_2$, 4 ATP, 0.5 GTP, 10 Tris-phosphocreatine, 10 HEPES. In some experiments, CsFl was replaced

with 15 $CsMeSO_3$ and 15.5 CsCl. Data are corrected for experimentally-determined liquid junction potentials of 7 or 10 mV ($CsMeSO_3$ and K-Gluconate internal solutions, respectively). For paired recordings in Figure 8, 10 mM GABA was added to the presynaptic K-Gluconate solution to reduce transmitter washout during whole-cell dialysis (Apostolides and Trussell, 2013a), and cartwheel cells in Figure 8a+b were recorded with a Cs-based internal solution containing 103 CsCl in place of $CsMeSO_3$ and CsFl. Fusiform cells in Figure 8c+d were recorded with the $CsMeSO_3$ internal solution. Pipette resistances for fusiform/cartwheel and stellate cells were typically 2-3 and 3-5 MOhm, respectively. In current-clamp, pipette capacitance was canceled and bridge balance maintained. For voltage-clamp recordings, neurons were held between -60 and -80 mV. Series resistance (< 15 and 25 MOhm for fusiform/cartwheel and stellate cells, respectively) was compensated 60-80% 'correction', 90% 'prediction' (bandwidth=3 kHz) and experiments were discarded if series resistance varied more than 20-25%. Stimulation of auditory nerve fibers (50-100 μsec pulses, 0.5-5 V) was performed using a bipolar metal electrode positioned in the ventral cochlear nucleus in a coronal slice that contained both cochlear nuclear divisions. Optogenetic stimulation was performed as described in (Apostolides and Trussell, 2013a) or using a custom-built, TTL-gated blue LED light source.

2-Photon imaging

The 2-photon imaging system (Prairie Technologies) is described in detail in (Bender et al., 2010). For Ca^{2+} imaging experiments, EGTA in the K-Gluconate internal solution was replaced with 150-200 μM Fluo-5F and 20 μM Alexa594. A Ti:sapphire pulsed laser (Coherent Chameleon Ultra II) was set to 810 nm and line scans (2-2.4 ms) were

performed at multiple sites along the somatodendritic axis of fusiform cells. Epi- and transfluorescence signals were collected with a 40x, 0.8 NA objective and a 1.4 NA oil immersion condenser. For imaging the morphology of coupled pairs, the laser was set to 800 nm; stellate and fusiform cells were filled with 20-30 μM Alexa594 or 90 μM Alexa488, respectively.

Auditory Brainstem Response

In order to be assured that the Cx36 KO mice did not have gross abnormalities in auditory function, we performed auditory brainstem response (ABR) audiometry test to pure tones. Three KO and three wt mice were anesthetized with a ketamine/xylazine cocktail, their eyes coated with Altalube (15% mineral oil/85% white petroleum) to prevent drying, and then placed on a heating pad in a sound-proof chamber. The experimenter was blinded to the genotype of the animals. Needle electrodes were placed subcutaneously near the each ear at the vertex. Each ear was then stimulated separately with a closed tube sound delivery system sealed into the ear canal. The auditory brain-stem response to a 1-ms rise-time tone burst at 4, 8, 12, 16, 24, and 32 kHz was recorded, and thresholds for visually obvious responses were obtained for each ear. Thresholds for 16-24 kHz tones ranged from 24-49 dB for wt mice and 24-39 dB for KO mice.

Data Acquisition and analysis

Electrophysiology data were recorded using Pclamp 9 software with a Molecular Devices Multiclamp 700B amplifier and a Digidata 1332A analog-to-digital converter board. Signals were acquired at 20-50 KHz and low-pass filtered at 1-10 KHz for offline analysis. Ca^{2+} imaging experiments were analyzed using custom macros in ImageJ or

Igor; data are expressed DG/R*100 and each trace is an average of 20-25 events. Ca^{2+} transient amplitudes were calculated by extrapolating the peak from monoexponential fits to the fluorescence decay at the end of the action potential train.

Coupling conductances between cells were calculated according to equation 7 of Bennett (1966), which is based on current responses and estimates of input resistance. Although the results suggested directional rectification of gap junction conductance between fusiform and stellate cells, the high input resistance of stellate cells makes it difficult to estimate an input resistance independent of junctional resistances in the network. The equation also does not account for dendritic cable properties. In any case it is likely that the high resistance of stellate cells is the dominant factor in greater efficacy of transmission from fusiform to stellate cells. Similar results were obtained using the equations of Devor and Yarom (2002).

Statistics

Data were analyzed with statistical tests listed in the main text. For ANOVAs, alpha was corrected for multiple comparisons and individual comparisons were made using Tukey post-hoc test. Chi-square tests were performed with Yate's correction.

Reagents

NBQX, R-CPP, D-APV, TTX, and SR95531 were from Abcam. Strychnine, MK801, and MFA were from Sigma-Aldrich.

Results

Electrical coupling between interneurons and principal cells.

We made whole-cell current-clamp recordings from pairs of fusiform and stellate cells in DCN-containing brain slices from 15-32 day-old mice. Neurons were identified based on morphological and electrophysiological criteria (see *Methods*). In 92/203 attempted pairs (45%), hyperpolarizing one neuron (the "prejunctional" cell) via negative current injection caused a simultaneous hyperpolarization in the other cell (the "postjunctional" cell; Figure 1b). The bi-directional translation of negative, subthreshold membrane potential deflections across two neurons is a hallmark of electrotonic coupling (Bennett and Zukin, 2004).

For 57 pairs in which transmission was tested bi-directionally, we calculated a coupling coefficient, defined as the ratio of the mean hyperpolarization during the last 50-100 ms of the current step in postjunctional and prejunctional cells. Surprisingly, we found that coupling strength showed strong directional preference, such that the average coupling coefficient in the fusiform-to-stellate direction was 0.10 ±0.01, but only 0.026 ±0.003 in the stellate-to-fusiform direction (Figure 1c,d). Although electrical coupling is stronger in neonates in some brain regions (Christie et al., 1989; Maher et al., 2009), coupling remained robust in DCN slices from mice 7-9 weeks of age (connection probability: 10/16; 62.5%). For pairs recorded in the more mature animals, the average fusiform-to-stellate cell coupling coefficient was 0.13 ±0.04 (n=8 pairs tested in this direction), whereas the stellate-to-fusiform coupling coefficient was 0.026 ±0.005 (n=5 pairs tested). These results show that the excitatory projection neurons of the DCN form strong, developmentally-persistent electrical synapses with local inhibitory interneurons.

Furthermore, the directional asymmetry is such that coupling from fusiform-to-stellate cells is nearly 4-fold stronger than in the opposite direction. Using the approach of Bennett (1966), we calculated the junctional conductances for each direction, finding an average fusiform-to-stellate cell conductance of 0.41±0.04 nS, and stellate-to-fusiform conductance of 0.98±0.11 nS (n=57 pairs). The average ratio of junctional conductances was 0.53±0.05, suggesting but not confirming rectification of gap junctional signals opposite to that expected from the coupling coefficients (see Methods).

Heterologous electrical coupling requires connexin36-containing gap junction channels.

Similar to other brain regions (Bennett and Zukin, 2004), electrical coupling was significantly compromised in DCN slices from mutant mice lacking the neuronal gap junction protein Connexin36 (Cx36 -/- mice; Figure 1d). Only 3/60 attempted pairs were coupled in these mice ($p<0.0001$ compared to wild-type, chi-square test). The average fusiform-to-stellate coupling coefficient of the remaining coupled pairs was 0.024 ±0.012 (n=3), whereas coupling was 0.003 ±0.001 in the opposite direction (n=2). Furthermore, electrical coupling in wild-type mice was blocked by a 15-30 min bath application of the gap junction blocker meclofenamic acid (MFA; Supplemental Figure S1). Together, these data show that electrotonic coupling between fusiform and stellate cells reflects *bona fide* electrical synapses between two very different cell types, and that this coupling requires the neuronal gap junction channel Connexin36.

Fusiform and stellate cells make weak homologous electrical synapses.

These results are surprising, as electrical coupling in the brain is typically observed between inhibitory neurons of the same class (Gibson et al., 1999; Hestrin and Galarreta, 2005). We therefore asked how coupling between fusiform and stellate cells contrasts with the efficacy of electrical transmission between the same cell types. Electrical coupling was indeed found to occur between stellate cells (9/42 of attempted pairs, Supplemental Figure S2a), as predicted from an anatomical study in the DCN (Wouterlood et al., 1984), and by homology to cerebellar stellate cells (Mann-Metzer and Yarom, 1999, Supplemental Figure S2b). However, the homologous coupling between stellate cells (0.024 ±0.005, average of both directions) was much weaker than fusiform-to-stellate cell coupling. Interestingly, we also found electrical coupling in the majority of attempted fusiform cell pairs (20/28; Supplemental Figure S3), although again this coupling was weak (0.014 ±0.001). By contrast, we found no evidence for electrical coupling between fusiform cells and another major molecular layer interneuron, cartwheel cells (0/27 connected pairs, data not shown). This result highlights the remarkable specificity of electrical coupling in the DCN as cartwheel cells make potent inhibitory synapses onto fusiform cells and overlap extensively in their dendritic fields (Oertel and Young, 2004). Altogether, our data reveal a broad, cell-type specific network of gap junction-mediated communication between excitatory and inhibitory neurons in the DCN molecular layer, and show that electrical transmission is largely biased towards heterologous coupling in the fusiform-to-stellate cell direction.

Fusiform cell action potentials are transmitted to stellate cells via electrical synapses.

Previous studies show that fusiform cells fire spontaneously *in vitro* (Roberts and Trussell, 2010; Leao et al., 2012) and *in vivo* (Davis and Young, 2000). The strong coupling between fusiform and stellate cells suggests that these spikes could modulate the membrane potential of electrically-coupled stellate cells. Accordingly, we observed spontaneous, subthreshold spikelets in the majority of current-clamp recordings from single stellate cells (44/65; 67%. Figure 2a, top trace). In voltage clamp, spikelets were clearly biphasic, with a fast inward current followed by a slower, smaller outward current (Figure 2a, bottom trace). These events were due to electrical coupling as they occurred in the presence of glutamate, GABA, and glycine receptor antagonists and were absent in recordings from Cx36 -/- mice (Figure 2b). Furthermore, paired recordings revealed that action potentials in prejunctional fusiform cells evoked spikelets in the postjunctional stellate cell (Figure 2c). Spikelets had an average positive peak amplitude of 0.9±0.2 mV and a mean latency from the peak of the prejunctional spike to that of the postjunctional spikelet of 837±72 μs (n=11 pairs). Figure 2d illustrates a fusiform cell spike-triggered average of action potential-evoked spikelets from the same pair as in Figure 2c. Furthermore, we never observed any spikelet transmission failures, indicating that fusiform cell spikes reliably propagate to stellate cells.

Electrical coupling occurs in distal regions of fusiform cell apical dendrites.

Stellate cell somata lie primarily near the DCN ependyma (Wouterlood et al., 1984), suggesting that electrical synapses are located in fusiform cell apical dendrites. In a

subset of our paired recordings, we investigated the location of putative contacts by first visualizing the morphology of fusiform cells with a fluorophore (Alexa488 or Alexa594) in the pipette internal solution and then selectively targeting stellate cells located near the fusiform cell's apical dendrites. This method significantly increased the probability of finding an electrically coupled pair from 36% without *a priori* visualization of fusiform cell morphology (41/113) to 57% when we targeted stellate cells near fusiform cell dendrites (51/90, p=0.006, chi-square test). We further characterized the anatomical organization of electrical coupling by imaging connected pairs using 2-photon microscopy. Fusiform and stellate cells were filled with Alexa488 (90 μM) and Alexa594 (20-30 μM) dyes, respectively. Figure 3a shows a Z-projection of the paired recording in Figure 1b, with the dashed line denoting the DCN ependyma. We consistently (N=11 electrically-coupled pairs) observed that stellate cell processes were primarily (though not exclusively) restricted to the distal region of fusiform cell apical dendrites, in agreement with previous anatomy (Wouterlood et al., 1984). Moreover, the dendritic arbors of the two cell types could be in close apposition (Figure 3b,c), suggesting putative points of contact.

Previous studies suggest that action potentials in fusiform cells back-propagate into the apical dendrites (Molitor and Manis, 2003; Tzounopoulos et al., 2004). The slower waveform of the spikelet versus the fusiform cell action potential suggests that the latter may be filtered as it propagates to the stellate cell, although the lack of transmission failures argues that fusiform cell spikes nevertheless reliably propagate through the apical dendrites (Figures 2c, d). In agreement with this interpretation, 2-photon Ca^{2+} imaging of fusiform cells loaded with Alexa594 and the Ca^{2+} indicator Fluo5F (150-200 μM)

revealed that action potentials invaded the entire apical arbor (Figure 3d, e). As expected from back-propagation of action potentials, the absolute amplitude of action potential-evoked ΔG/R signal (see *Methods*) did not attenuate as a function of approximate distance from the soma, but instead remained constant throughout the distal processes (n=6 cells, Figure 3e). Altogether these data argue that spikelets in stellate cells originate as action potentials that have propagated through the apical dendritic arbor of the fusiform cell. Moreover, the obvious size difference between fusiform and stellate cells suggests that impedance mismatch contributes to the coupling asymmetry observed in Figure 1. Accordingly, input resistances for the two cells were found to differ by over tenfold (fusiform cells: 87±37 MOhms [cf. Zhang and Oertel, 1994]; stellate: 996±139 MOhms (n=29), this study).

Frequency-dependent transmission of signals from fusiform to stellate cells.

Previous studies suggest that electrotonic spikelets may exert a predominantly inhibitory effect on the postjunctional cell, as the low-pass filter properties of gap junction channels allow preferential passage of the spike after-hyperpolarization (AHP) compared to the faster depolarizing Na^+ upstroke (Dugué et al., 2009; Vervaeke et al., 2010). Indeed, our paired recordings (Figure 2d) show that fusiform-to-stellate cell spikelets are biphasic, with a prominent negative-going phase. However, other studies indicate that the shape of postjunctional spikelets depends on the firing rate of the prejunctional cell, and that the hyperpolarizing trough disappears at frequencies >50 Hz (Gibson et al., 2005). We therefore asked if the prejunctional spike frequency determined whether fusiform cells exert a net depolarizing or hyperpolarizing effect on stellate cells.

We evoked spikes in fusiform cells at different frequencies and measured the mean change in membrane potential of the stellate cells to which they were coupled (Figure 4a,b). Stellate cells were hyperpolarized with constant bias current to prevent action potentials. Fusiform cell spikes evoked at 1 and 10 Hz had no effect on mean membrane potential in stellate cells (1 Hz: 0.005±0.009 mV; 10 Hz: -0.04±0.04 mV, n=9 pairs). Thus, during low-frequency activity similar to that observed *in vivo* during periods of quiescence, fusiform cell activity does not cause the stellate cell's membrane potential to appreciably deviate from baseline. On the other hand, high-frequency fusiform cell activity (50 and 100 Hz) had a net excitatory effect, causing a mean voltage change of +0.3 mV±0.1 mV and +0.8±0.2 mV. Given that fusiform cells can fire >200 Hz during sound-evoked activity *in vivo* (Davis and Young, 2000; Ma and Brenowitz, 2012), these data indicate that physiological spike rates in single fusiform cells depolarize the membrane potential of electrically coupled interneurons in a frequency-dependent manner.

Following a spike train in fusiform cells, a post-train AHP was invariably apparent. For trains elicited by square-pulse current injection (0.3-1 nA, 0.4-1 s), the negative peak of the AHP was -11.3 ±1.0 mV below rest with a half-width of 406 ± 58 ms (n=8 fusiform cells; Figure 4c). Intracellular recordings from fusiform cells driven by acoustic stimuli *in vivo* show that this AHP occurs upon sound termination (Rhode et al., 1983; Hancock and Voigt, 2002), indicating that the AHP is not an artifact of direct current injection through the recording pipette. Paired recordings revealed that the post-train AHP in fusiform cells reliably invaded stellate cells (n=7 pairs, Figure 4c). Interestingly, the absolute peak amplitude of the postjunctional AHP in stellate cells was 92±8% of the

steady-state depolarizing phase, suggesting that positive and negative-going phases of fusiform cell activity may be of comparable significance to stellate cells.

Auditory nerve activity is transmitted to stellate cells via gap junction coupling.

Auditory nerve fibers contact the basal dendrites of fusiform cells, but do not extend into the DCN molecular layer (Merchan et al., 1985). However, the results of Figures 4a-c show that single fusiform cells can control the membrane potential of electrically-coupled stellate cells, suggesting that acoustic information from the auditory nerve may nevertheless reach stellate cells through electrical synapses. We explicitly tested the possibility that stellate cells sense activity in the auditory pathway by recording from single stellate cells and stimulating the auditory nerve with a bipolar electrode placed in the ventral cochlear nucleus. In agreement, trains of stimuli to the auditory nerve depolarized stellate cells (3.2±0.5 mV; n=6 cells, Figure 4d,e). Two features of this response indicate that it occurred through gap junction coupling with fusiform cells. First, the depolarization was followed by a hyperpolarization (in current clamp) or outward current (in voltage clamp; Figure 4d), similar to the postjunctional activity generated by direct current injection in fusiform cells (Figure 4c). The slow outward current seen in voltage-clamp likely reflects the membrane potential of prejunctional fusiform cells relaxing towards baseline during the decay of the AHP. Second, depolarization of the stellate cell to 0 mV, which markedly reduces the driving force for glutamatergic transmission, only mildly reduced the amplitude of the steady-state response (Figure 4e. Average amplitude at -67 mV: -17±3 pA; 0 mV: -13±3 pA; ratio of average current at 0 mV to -67 mV= 0.75±0.03; n=5 cells). Nevertheless, these voltage-independent

responses were entirely blocked by bath application of AMPA and NMDA receptor antagonists (Figure 4e, lower traces; n=3 cells), showing that they were generated by glutamatergic synaptic transmission. Thus, auditory nerve synapses generate excitatory responses that do not arise from transmitter-gated channels in stellate cells. These results strongly suggest that the auditory pathway transmits information to stellate cells, albeit independently of a direct auditory nerve projection into the molecular layer.

Optogenetic activation of multiple fusiform cells.

Because auditory nerve input to the DCN is tonotopically organized, single fusiform cells respond best to a limited range of sound frequencies. If multiple prejunctional fusiform cells with similar frequency tuning converge upon a single stellate cell, our paired recordings likely underestimate the extent to which electrical synapses control stellate cell excitability. To determine the capacity of multiple prejunctional fusiform cells to control stellate cell membrane potential, we performed experiments in transgenic mice expressing the light-activated cation channel channelrhodopsin2 (ChR2) driven by the Thy1 (Thy1-ChR2-YFP line 18: Arenkiel et al., 2007) or vesicular glutamate transporter 2 promoters (VGluT2-ChR2-YFP: Hägglund et al., 2010). Both lines robustly expressed ChR2 in fusiform cells: Blue light flashes delivered through the microscope objective caused large inward currents in voltage-clamped fusiform cells and reliably drove spiking in current-clamp (Figure 5a,d). The absolute amplitudes of photocurrents in voltage-clamped fusiform cells from Thy1-ChR2 mice were on average significantly larger than those observed in VGluT2-ChR2 line (Thy1: 991 ± 185 pA, n=19 cells. VGluT2: 225 ±25 pA, n=13 cells. p=0.002, unpaired t-test). However, similar results

were obtained with Thy1 and VGluT2 lines for the optogenetic experiments in Figures 5-7, so the data were pooled.

In slices from ChR2 mice, blue light also robustly increased the firing frequency of stellate cells recorded in current-clamp (Figure 5b,e). These experiments were performed in the presence of AMPA and NMDA receptor blockers (10 μM NBQX and 5 μM R-CPP), showing that the rapid increase in stellate cell spike rate was not due to ChR2 activation of presynaptic glutamatergic axons. We further investigated the depolarization underlying this phenomenon by hyperpolarizing stellate cells with negative bias current to prevent spiking. As expected from activating prejunctional fusiform cells, blue light evoked trains of spikelets atop a DC depolarization (Figure 5c,f, upper traces) followed upon light termination by the post-train AHP seen in paired recordings (e.g., Figure 4c). In voltage-clamped stellate cells, the same light stimuli caused biphasic "postjunctional photocurrents" characterized by spikelets riding atop an inward current, followed by a slow outward current upon light termination (Figure 5c,f, lower traces). The amplitudes of the mean steady-state inward and peak outward postjunctional photocurrents were -16.9 ± 2.5 and 14.4 ± 1.8 pA, respectively (n=28 cells). Careful inspection of the voltage-clamp traces revealed spikelets of different amplitudes (Figure 5f,g), suggesting that multiple fusiform cells with different coupling coefficients contact a single stellate cell. Additionally, we never observed light-evoked spikelets, depolarizations or inward currents in cartwheel cells (0/37 cells tested), further highlighting the cell-type specificity of electrical coupling.

Several control experiments led us to reject the possibility that the light-evoked depolarizations and postjunctional photocurrents in stellate cells were due to direct ChR2

expression in the stellate cell plasma membrane. First, the VGluT2 line should show ChR2 expression restricted to excitatory glutamatergic neurons such as fusiform cells (Ito and Oliver, 2010) and not in the GABAergic stellate cells(Mugnaini, 1985). Second, if postjunctional photocurrents are due to ChR2 expression in stellate cells, they should follow the current-voltage (IV) curve documented in previous studies of the ChR2 cation channel and reverse at positive potentials (Nagel et al., 2003). However, postjunctional photocurrents in voltage-clamped stellate cells were only minimally voltage-dependent and remained inward at +53 mV, as expected for a cation current arising through an unclamped distal compartment (Supplemental Figure S4a,b). By contrast, photocurrents in fusiform cells displayed a rectifying IV relationship expected of the ChR2 channel and reversed at positive potentials. Third, the gap junction blocker MFA abolished postjunctional photocurrents in stellate cells but had little effect on ChR2 photocurrents in fusiform cells (Supplemental Figure S4c,d). Together, these data show that postjunctional photocurrents represent the summed activity of prejunctional fusiform cells, not ectopic expression of ChR2 in stellate cells. Finally, bath application of tetrodotoxin (TTX; 500 nM) significantly reduced the amplitude of the stellate cell postjunctional depolarization by 38±4% (baseline: 5.8 ± 1.0 mV, TTX: 3.4 ±0.6 mV, n=14, p=0.0005, paired t-test), and reduced the postjunctional AHP during the light-off response by 61±3% (baseline: -5.2 ± 0.8 mV, TTX: -2.2 ± 0.5 mV, n=14, $p<0.0001$, paired t-test). These data show that spikes in prejunctional fusiform cells contribute to the light-evoked depolarizations in stellate cells. Thus, active and passive depolarizations in fusiform cells are transmitted to stellate cells. Moreover, the fact that the ChR2-induced, TTX-sensitive depolarization (2.4 mV) in stellate cells was over 2-fold greater than the

depolarization generated by stimulating a single fusiform cell (0.8 mV at 100 Hz) indicates that the ChR2-induced depolarization was indeed generated by multiple prejunctional fusiform cells.

Fusiform cell activity increases stellate cell spike output.

Can a single fusiform cell suffice to increase stellate cell spike output, or does this require simultaneous activity in multiple prejunctional cells? We recorded electrically-coupled pairs and injected a family of depolarizing current steps in the stellate cell with and without simultaneous 100-Hz activity in the prejunctional fusiform cell (Figure 6a). Negative bias current was used to prevent spontaneous firing of both neurons. A linear fit was made to the non-zero portions of stellate cell input/output curves to compare the slope and offset (x-intercept for y=0) of the function during the two conditions (Mitchell and Silver, 2003). In 8 pairs tested, fusiform cell activity shifted the offset of stellate cell input/output curves from 28.8 ± 5.0 pA during baseline to 25.2 ± 5.0 pA when the fusiform cell was active (Figure 6c. -13 ± 4% difference, p=0.02, paired t-test). However, fusiform cell activity had no significant effect on the slope of the input/output curve (baseline: 1.1±0.1 pA/Hz, with fusiform cell activity: 1.2±0.1 pA/Hz. +4.5±2.8% change, p=0.14, paired t-test). Furthermore, activating multiple prejunctional fusiform cells with blue light stimuli in ChR2 mice (Figure 6b) caused significantly larger shifts in the offset of stellate cell input/output functions (Figure 6d. From 34.1 ± 5.4 pA to 15.1 ± 4.9 pA. -52 ± 10% difference, n=10 cells, p=0.005, paired t-test) with no significant change in the slope (1.6 ±0.15 pA/Hz to 1.47 ± 0.11 pA/Hz. -6.8±4.3% change, p=0.21). Thus, activity in even a single fusiform cell significantly enhances the excitability of local interneurons,

and this represents a largely additive transformation of the stellate cell's input/output function.

Distinct epochs of fusiform cell activity bi-directionally control stellate cell spike output.

The large postjunctional AHP observed in stellate cells following fusiform cell or auditory nerve spike trains (Figures 4 & 5) suggests that the timing of fusiform cell activity determines whether electrical synapses exert a net excitatory or inhibitory effect on stellate cell spike output. We tested this by recording single stellate cells in ChR2 mice and varying the time interval between depolarizing current steps in the stellate cell and blue light stimuli, thereby allowing either the depolarizing or AHP phase of fusiform cell activity to overlap with stellate cell spiking (Figure 7a). The results were dramatic, as coincident activation of fusiform cells within a ±100 ms time window of stellate cell depolarization increased spike output by 50±5% compared to baseline (Figure 7b, n=13). By contrast, activating fusiform cells 500 ms *before* stellate cell current injection, resulting in maximal overlap of the postjunctional AHP and stellate cell depolarization, reduced the total number of spikes by 53±6%. Thus, the timing of fusiform cell activity with respect to stellate cell excitation bi-directionally regulates the number of spikes generated by the interneuron over a 3-fold range.

Fusiform cell activity generates local inhibition.

Our data show that activity of even a single prejunctional fusiform cell is sufficient to excite stellate cells, and thus predict that fusiform cell spiking should increase inhibition in the DCN molecular layer by depolarizing the stellate cell network. By homology to their cerebellar counterparts, stellate cells are suggested to synapse onto the Purkinje-like cartwheel cells of the DCN (Wouterlood et al., 1984; Rubio and Juiz, 2004). Accordingly, paired recordings revealed unitary stellate-to-cartwheel cell inhibitory postsynaptic currents (IPSCs) in 8/26 attempted pairs (30.8% connection probability, Figure 8a).

To explicitly test whether fusiform cell activity generates inhibition in the DCN, we recorded from single cartwheel cells while isolating GABAergic transmission and optogenetically activating fusiform cells (300-500-ms light stimuli). In the majority of voltage-clamped cartwheel cells (25/28), optogenetic activation of fusiform cells caused barrages of IPSCs (Figure 8b) that were entirely blocked by the $GABA_A$ receptor antagonist SR95531 (5 μM; Figure 8b, n=8). These IPSCs were not due to polysynaptic recruitment of interneurons via glutamatergic synapses because excitatory transmission was blocked by 10 μM NBQX and 5 μM R-CPP in all experiments.

We also examined whether activation of fusiform cells could lead to inhibition of other fusiform cells through stellate-to-fusiform chemical synapses. Fusiform cells were recorded in voltage-clamp near the reversal potential for the ChR2 photocurrent (0-13 mV) using a Cs-based internal solution. In 7 of 11 fusiform cells tested, blue light stimuli generated barrages of IPSCs that were partially occluded by the small inward

photocurrent (Figure 8c). These IPSCs were not triggered by excitatory glutamatergic synapses because all experiments were performed in the presence of NBQX and R-CPP. Bath application of inhibitory synaptic blockers (SR95531 and strychnine; n=6 cells) blocked the IPSCs, and subsequent digital subtraction of the average photocurrent trace from the single traces recorded in NBQX/CPP clearly showed that optogenetic activation of neighboring fusiform cells generated a robust inhibitory response in the voltage-clamped neuron (Figure 8d). Thus, principal neuron activity generates time-locked increases in local inhibition, thereby regulating the excitability of neighboring principal neurons and interneurons.

Discussion

A hallmark of sensory circuits is that external stimuli recruit inhibition proportional to the magnitude of excitatory drive (Isaacson and Scanziani, 2011). Whether the sensitivity of inhibitory neurons is fixed or labile with respect to a given stimulus is unclear. We have demonstrated a simple cellular mechanism that uses gap junctions to rapidly control the moment-to-moment dynamics of inhibition based upon the timing of principal neuron activity. The probability of electrical coupling between principal cells and interneurons was high (57%), suggesting that this transmission pathway constitutes a significant component of the DCN circuit. Moreover, electrical coupling was robust in animals as old as two months postnatal, indicating that this circuit motif should function as a component of sensory processing and is not a transient developmental phenomenon. Thus, our findings raise the possibility that even at the earliest stages of auditory

processing, ongoing sensory input bi-directionally regulates the threshold for recruiting local inhibition.

These results significantly revise the canonical DCN model, whereby multisensory and auditory inputs recruit distinct classes of interneurons (Oertel and Young, 2004). Through electrical coupling with fusiform cells, the stellate cell membrane potential will rapidly sense ongoing auditory activity, a prediction supported by our observation that auditory nerve activation itself generates signals in stellate cells through gap junction coupling. There are no recordings from identified stellate cells *in vivo*, presumably due to their small size and precarious location at the ependymal edge of the brainstem. Given that single stellate cells are coupled to multiple prejunctional fusiform cells, our data suggest that electrical coupling may endow stellate cells with complex "best frequency" characteristics reflecting the additive frequency tuning properties of prejunctional fusiform cells. Nevertheless, an understanding of how electrical coupling regulates information flow through the DCN will require knowing the functional connectivity between a stellate cell's postsynaptic targets and its electrically-coupled partners. Stellate cells form inhibitory synapses onto cartwheel and fusiform cells(Osen et al., 1990; Rubio and Juiz, 2004; our Figure 8). Activating stellate cells through the gap junction pathway generated IPSCs in a functionally silent (e.g., voltage-clamped) fusiform cell (Figure 8c,d), showing that stellate cells do not strictly perform feedback inhibition onto activated principal neurons. However, it is unknown whether stellate cells inhibit fusiform cells that are tuned to similar frequencies as those with which they form electrical synapses, or if stellate cells inhibit fusiform cells across frequencies, a form of lateral inhibition. Similarly, the spatial distribution of cartwheel cell axons is also not yet known; thus it

remains to be determined if stellate cells inhibit cartwheel cells that control local or more distant fusiform cells.

Further studies are required to definitively assign a specific functional role for the novel circuit we have identified. The DCN is organized similarly to the cerebellum and cerebellum-like structures found in mammals and weakly electric fish: Fusiform cells are analogous to deep cerebellar nucleus neurons and the glutamatergic efferent cells of mormyrid electric fish's electrosensory lobe, whereas cartwheel cells are thought to function as the Purkinje-like cells of these circuits (Oertel and Young, 2004; Bell et al., 2008). Given that cerebellum-like circuits may mediate the adaptive filtering of self-generated sensory input, the molecular layer circuitry of the DCN could facilitate comparison of acoustic signals in the environment with body orientation or activity (Oertel and Young, 2004; Requarth and Sawtell, 2011). A key cellular phenomenon suggested to underlie such adaptive filtering is that coincident activity of predictive parallel fiber and instructive sensory pathways induces an anti-Hebbian, long-term depression of the active parallel fiber synapses (Bell et al., 1997b; Han et al., 2000). For example, in the cerebellum-like electrosensory lobe of the mormyrid electric fish, the Purkinje-like medium ganglion cells and excitatory efferent neurons integrate sensory information from electroreceptors on the skin (e.g., instructive signals) with parallel fiber synapses that convey predictive information regarding the fish's motor movements and behavior (Bell et al., 2008; Requarth and Sawtell, 2011). Simultaneous pairing of motor commands with electrosensory signals leads to long-term depression of the active parallel fibers in Purkinje-like cells and efferent neurons (Bell et al., 1997a; Sawtell and Williams, 2008). On a circuit level, this phenomenon is thought to be involved in

generating activity patterns that are "negative images" of predictable sensory input (Bell et al., 2008; Requarth and Sawtell, 2011). However, experiments show that associative, long-term plasticity in cerebellum-like circuits requires prolonged induction protocols and is fully expressed only several minutes after induction (Han et al., 2000; Tzounopoulos et al., 2004; Hansel et al., 2006; Sawtell and Williams, 2008). Our work suggests an alternative mechanism that might contribute to a moment-to-moment reduction of parallel fiber synapses, thereby mediating adaptation to a rapidly changing environment. We find that activation of fusiform cells via the auditory pathway depolarizes stellate cells (Figure 4d), and thus can sensitize molecular layer interneurons to subthreshold parallel fiber inputs. Furthermore, fusiform cell activity alone is sufficient to generate robust inhibition onto two major targets of parallel fibers: cartwheel cells and neighboring fusiform cells (Figure 8). Thus, auditory signals could, in principle, rapidly recruit or suppress stellate cells and control the efficacy of parallel fiber actitivty, depending on the relative timing of auditory and non-auditory sensory signals. Interestingly, recent studies suggest that cerebellar stellate cells sense glutamate "spillover" from instructive climbing fiber synapses (Szapiro and Barbour, 2007; Mathews et al., 2012; Coddington et al., 2013), and feedforward inhibition generated by climbing fiber activity is sufficient to rapidly decrease the capacity of parallel fibers to drive spikes in neighboring Purkinje cells (Coddington et al., 2013). Together with our data, these findings imply that transmission of instructive signals to molecular layer interneurons may be a general feature of cerebellum-like circuits.

Acknowledgements: We thank Michael Roberts and Sidney Kuo for preliminary observations that led us to search for electrical coupling in the DCN; Michael Bateschell and Ruby Larisch for help with mouse colony management and genotyping; Carolina Borges-Merjane for genotyping the Thy1-ChR2 mice and providing cerebellum slices used in Supplemental Figure 2; Hsin-Wei Lu for writing the macros used to analyze the calcium imaging data; Sarah Foster for performing the ABR measurements. Kevin Bender, Will Giardino, and Nate Sawtell for critical comments on the manuscript. Funding was provided by NIH Grants R01DC004450 to L.O.T. and F31DC012222 to P.F.A.

Figure 3.1

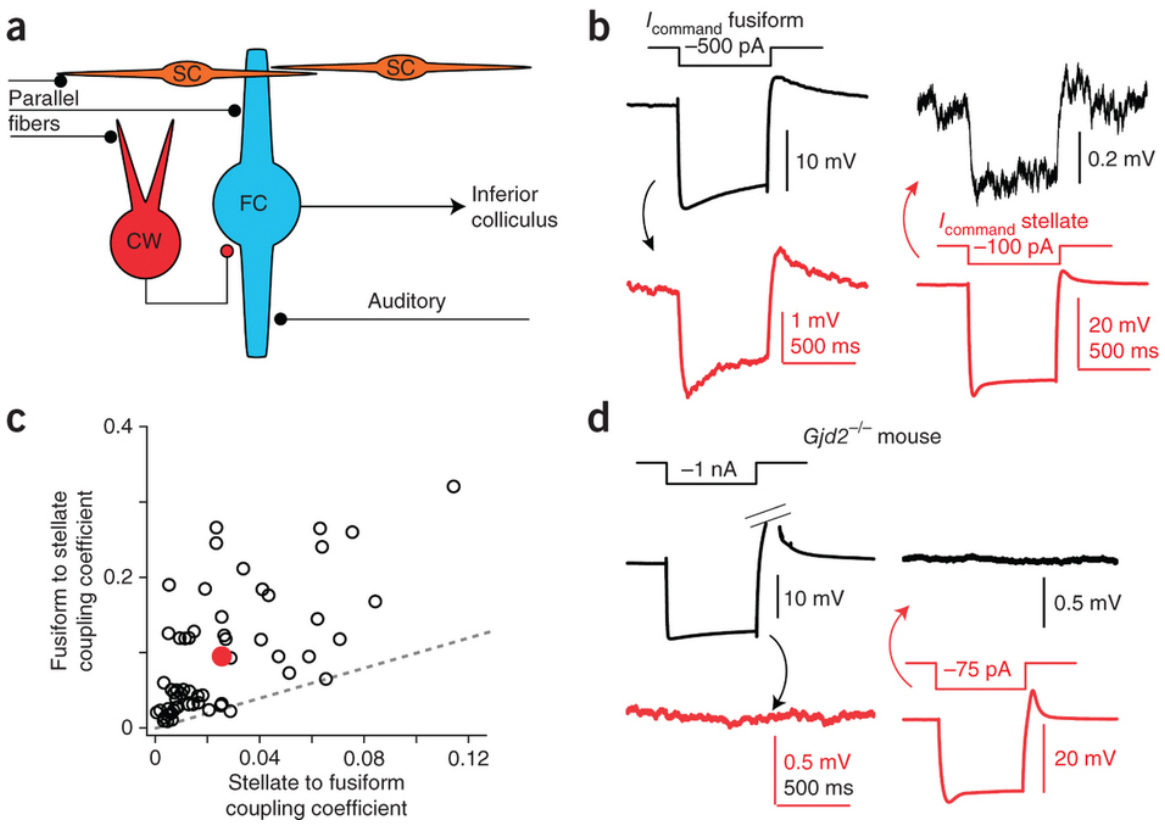

Figure 3.1: Asymmetric electrical coupling between DCN fusiform and stellate cells.

a) Diagram of DCN circuitry. The excitatory projection neurons of the DCN (fusiform cells; FC), integrate excitatory auditory nerve and multisensory parallel fiber synapses(Oertel and Young, 2004). Parallel fibers, but not auditory nerve fibers, impinge upon two distinct types of inhibitory interneurons: cartwheel cells (CW) and superficial stellate cells (SC).

b) Example average traces from an electrically-coupled fusiform/stellate pair. Negative current injection into the fusiform cell (black trace) causes the expected

hyperpolarization. This causes a smaller voltage deflection with similar time course in the simultaneously recorded stellate cell (red trace, note difference in scale). Similarly, hyperpolarizing the stellate cell causes a small voltage deflection in the fusiform cell.

c) Summary of coupling coefficients for 57 pairs similar to (b). Red point is average of the data set, and dotted gray line represents the unity line. Almost all pairs fall above the unity line, showing that the coupling coefficient is stronger in the fusiform-to-stellate direction compared to vice versa.

d) Example average traces from a typical paired recording in a DCN slice from a Cx36 -/- mouse. Color coding is similar to panel (b). Out of 60 attempts, only 3 pairs were connected.

Figure 3.2

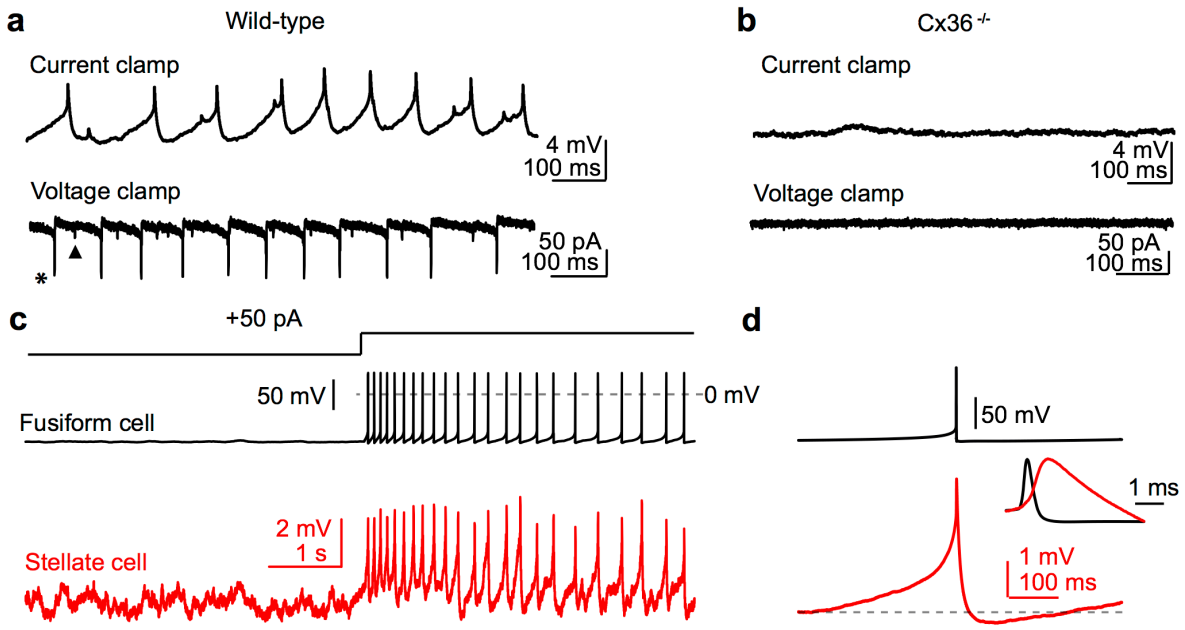

Figure 3.2: Fusiform cells generate spikelets in electrically-coupled stellate cells.

a) Example recording from a wild-type mouse showing spontaneous spikelet activity in a single stellate cell recorded in current- and voltage-clamp (upper and lower traces, respectively). These recordings were performed in the presence glutamate, glycine and $GABA_A$ receptor blockers. Spikelet events with two distinct amplitudes are apparent (e.g., see asterisk and triangle), suggesting that at least two prejunctional fusiform cells are coupled to the same stellate cell but with different coupling coefficients.

b) Same experiment as (a), but in a Cx36 -/- mouse. No spikelet events were evident in stellate cells recorded from knockout mice; (0/77 cells tested, $p<0.0001$ compared to wild-type, chi-square test). Traces were similarly recorded in the presence of synaptic blockers.

c) Example paired recording from electrically coupled fusiform and stellate cells (upper and lower traces, respectively). The fusiform cell was driven to spike by positive current injection denoted by the command current waveform. Notice the immediate onset, uniform amplitude, and lack of transmission failures of spikelets in the stellate cell.

d) Example averages (acquisition triggered by detection of the prejunctional spike) from the same pair as in (c). Only action potentials that occurred more than 300 ms apart were included in the average, so as to highlight the full time course of the depolarizing and hyperpolarizing phases of the spikelet waveform. The spikelet rises *before* the peak of the fusiform cell action potential, suggesting that the prejunctional voltage trajectory determines the moment-to-moment fluctuations in stellate cell baseline membrane potential. The inset shows the spikelet rising phase on a fast time base and normalized to the peak of the prejunctional spike, highlighting that the spikelet rises before the downswing of the fusiform cell action potential.

Figure 3.3

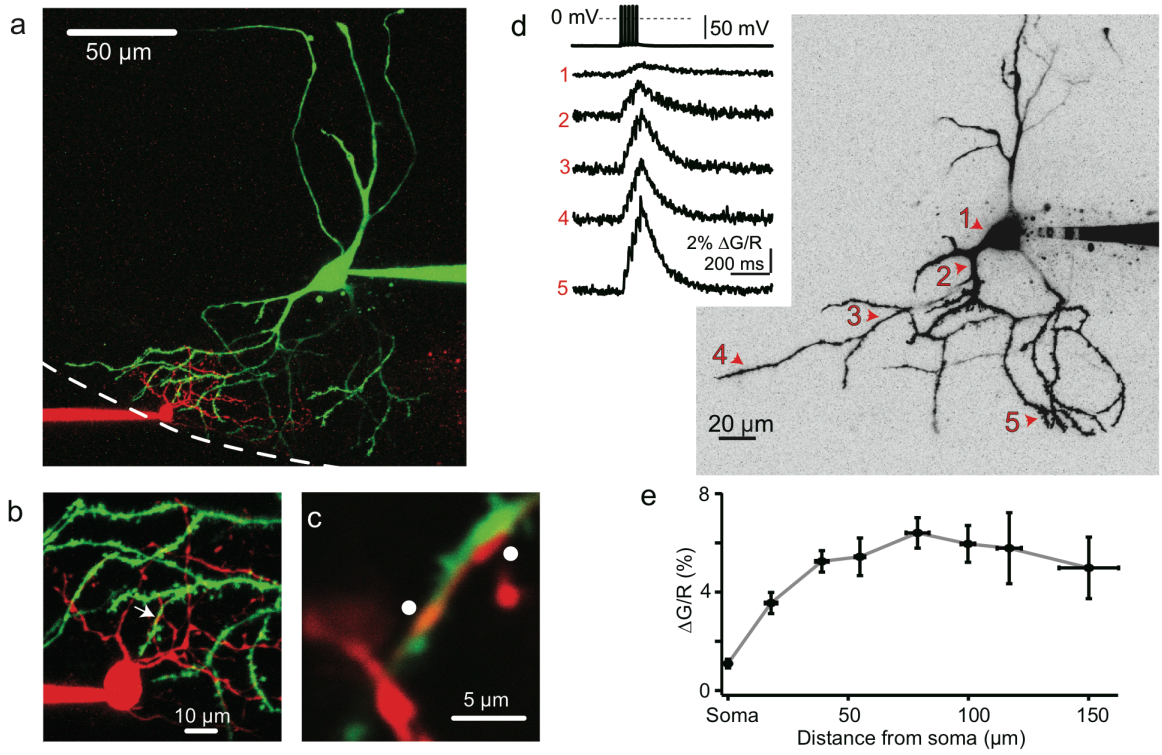

Figure 3.3: Fusiform cell action potentials propagate into the distal apical dendrites.

a) 2-photon maximum intensity z-stack from the example pair in Figure 1b. The stellate and fusiform cells are filled with Alexa594 (red) and Alexa488 (green) dyes, respectively. Dotted gray line represents the approximate ependymal border of the DCN. Stellate cell processes do not extend into the cell body layer, whereas fusiform cell processes span the entire length of the DCN.

b) A maximal intensity z-stack at higher magnification from the same pair.

c) High magnification, single optical section of the area denoted by the white arrow in panel (b), showing a high degree of overlap between the stellate and fusiform cell processes (white dots).

d) Right: Maximum intensity 2-photon z-stack from a representative fusiform cell showing line scan locations during the Ca^{2+} imaging experiment. Left: Example sweeps of action potential-evoked Fluo-5f Ca^{2+} transients (5 spikes, 50 Hz) recorded at the corresponding dendritic locations marked in the z-stack on the left. Each trace represents the average of 20-25 trials.

e) Absolute $\Delta G/R$ are plotted as a function of approximate distance from the soma. Response amplitudes remain relatively constant along the dendrite. Each data point represents values from 3 to 6 individual cells.

Figure 3.4

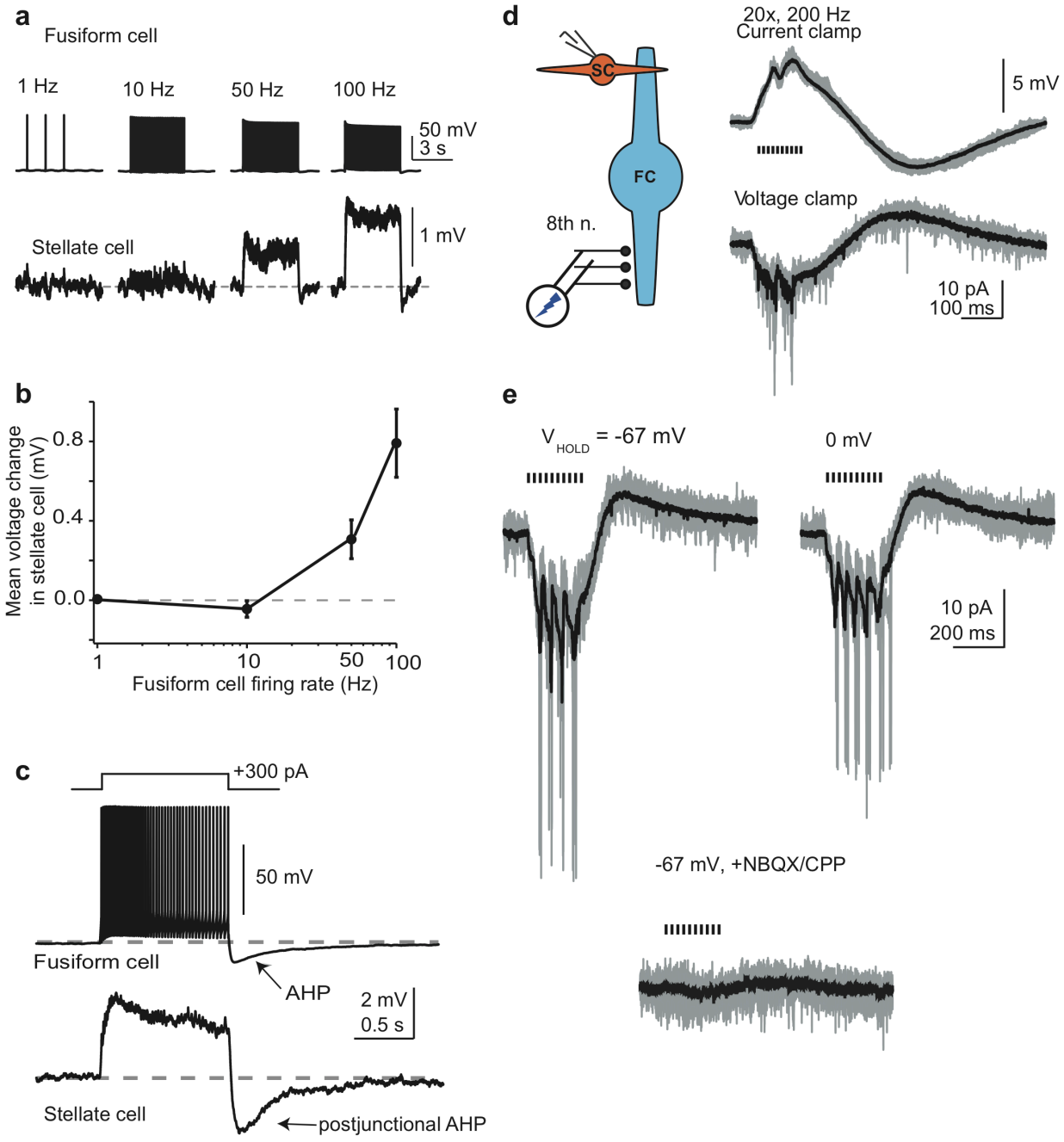
a
Fusiform cell
1 Hz
10 Hz
50 Hz
100 Hz
50 mV
3 s
Stellate cell
1 mV
b
Mean voltage change in stellate cell (mV)
0.8
0.4
0.0
1
10
50
100
Fusiform cell firing rate (Hz)
c
+300 pA
50 mV
Fusiform cell
AHP
2 mV
0.5 s
Stellate cell
postjunctional AHP
d
SC
FC
8th n.
20x, 200 Hz
Current clamp
5 mV
Voltage clamp
10 pA
100 ms
e
V HOLD = -67 mV
0 mV
10 pA
200 ms
-67 mV, +NBQX/CPP

Figure 3.4: Single fusiform cells control the membrane potential of electrically-coupled stellate cells in a frequency-dependent manner.

a) Upper traces are spikes evoked in a fusiform cell at different frequencies (single trials). Lower traces are time-synchronized averages of multiple trials in an electrically-coupled stellate cell.

b) Summary data from 9 experiments similar to (a) plotting the stellate cell's mean voltage change from baseline as a function of fusiform cell spike frequency.

c) Positive current injection (+300 pA) in a fusiform cell causes high-frequency firing followed by a slow AHP upon stimulus offset (upper trace). A simultaneously recorded, postjunctional stellate cell (lower trace) is transiently depolarized above baseline (dotted gray line) during fusiform cell spiking and hyperpolarized by the AHP upon stimulus termination. Top trace is a single trial, bottom trace is an average of eight sweeps.

d) Activation of auditory nerve fibers elicits biphasic signals in stellate cells. Left panel: layout of experiment. A bipolar stimulation electrode was placed in the ventral cochlear nucleus (VCN) >600 mm from the recorded cell in DCN. Recording was made in the presence of 1 mM strychnine/10 mM SR95531. Right panel: Stellate cell recorded in current or voltage clamp (upper and lower traces, respectively) during stimulation of the VCN with 20 shocks at 5-ms intervals. The stellate cell was recorded with a K-gluconate-based pipette fill. In current clamp, negative bias current (-30 pA) was injected to prevent spike generation.

e) In a $CsMeSO_3$-filled stellate cell, VCN stimuli were delivered while the membrane potential was clamped at either -67 mV or 0 mV (reversal potential for glutamatergic

EPSCs). Stimulus was 10 shocks at 20-ms intervals. Little difference was seen in response amplitude at the two potentials, indicating it was generated by ionic currents in a prejunctional cell. Lower trace: AMPA and NMDA receptor blockers 10 mM NBQX and 5 mM CPP) eliminated the response, as expected for glutamatergic transmission from auditory nerve fibers. For panels d + e, gray traces are 5 consecutive trials, and black traces are an average of between 12-31 trials. Stimulus artifacts are blanked for clarity.

Figure 3.5

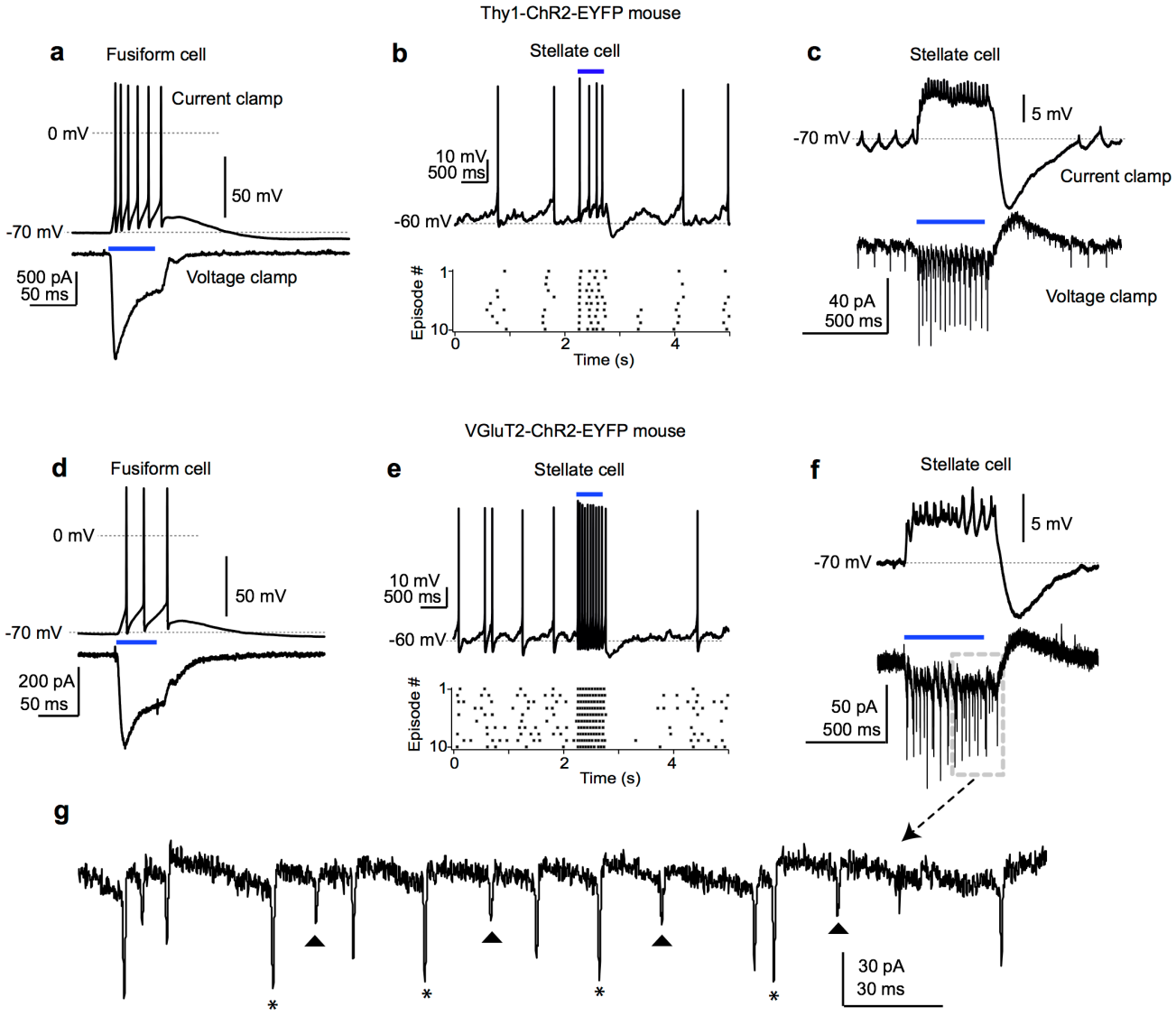
Thy1-ChR2-EYFP mouse
a
Fusiform cell
Current clamp
0 mV
50 mV
-70 mV
500 pA
50 ms
Voltage clamp
b
Stellate cell
10 mV
500 ms
-60 mV
Episode #
1
10
0
2
4
Time (s)
c
Stellate cell
5 mV
-70 mV
Current clamp
40 pA
500 ms
Voltage clamp
VGluT2-ChR2-EYFP mouse
d
Fusiform cell
0 mV
50 mV
-70 mV
200 pA
50 ms
e
Stellate cell
10 mV
500 ms
-60 mV
Episode #
1
10
0
2
4
Time (s)
f
Stellate cell
5 mV
-70 mV
50 pA
500 ms
g
30 pA
30 ms

Figure 3.5: Optogenetic activation of fusiform cells depolarizes stellate cells.

a) Example traces from a fusiform cell in a Thy1-ChR2-EYFP mouse. Blue light stimuli (50 ms; blue bar) generates action potentials in current-clamp (upper traces) and photocurrents in voltage clamp (lower traces). Top trace is a single trial, lower trace is an average of multiple trials.

b) Top: Example current-clamp recording from a stellate cell in a Thy1-ChR2-EYFP mouse (0 pA bias current). A 500 ms light stimulus denoted by the blue bar causes an immediate increase in spike frequency. Lower panel: A raster plot of ten sequential trials from this experiment, highlighting the increase in spike rate upon optogenetic stimulation of fusiform cells. Similar results were obtained in 18/19 attempted stellate cells.

c) Example from a stellate cell in the Thy1-ChR2-EYFP mouse (different cell as panel b). Top trace: In current clamp, -25 pA bias current is injected to hyperpolarize the cell and prevent action potential generation. A blue light flash (400 ms) causes spikelets riding atop a steady-state depolarization, followed by a postjunctional AHP upon light offset. Note the similarity to the traces in 4c. Lower trace: The same light stimulus delivered when the cell is voltage-clamped at -70 mV causes a barrage of fast inward spikelets, followed by a slow outward current upon stimulus offset. Traces are single trials.

d) Example traces from a fusiform cell in a VGluT2-ChR2-EYFP transgenic mouse. Similar to the Thy1-ChR2 mouse in panel (a), blue light (50 ms) drives spikes and induces photocurrents.

e) Example current-clamp recording from a single stellate cell in the VGluT2-ChR2-EYFP mouse. The experiment and panel layout is similar to that in (b).

f) Example recording from a stellate cell in the VGluT2-ChR2 mouse showing that blue light causes similar depolarizations and inward currents as in the Thy1-ChR2 mouse. Thus, spikelets and AHPs originate in prejunctional glutamatergic neurons.

g) Enlargement of the area denoted by the gray dashed rectangle in (f). Note the presence of spikelets with multiple distinct amplitudes (denoted by the triangle and asterisks), suggesting that this stellate cell is coupled to at least two separate fusiform cells with different coupling coefficients.

Figure 3.6

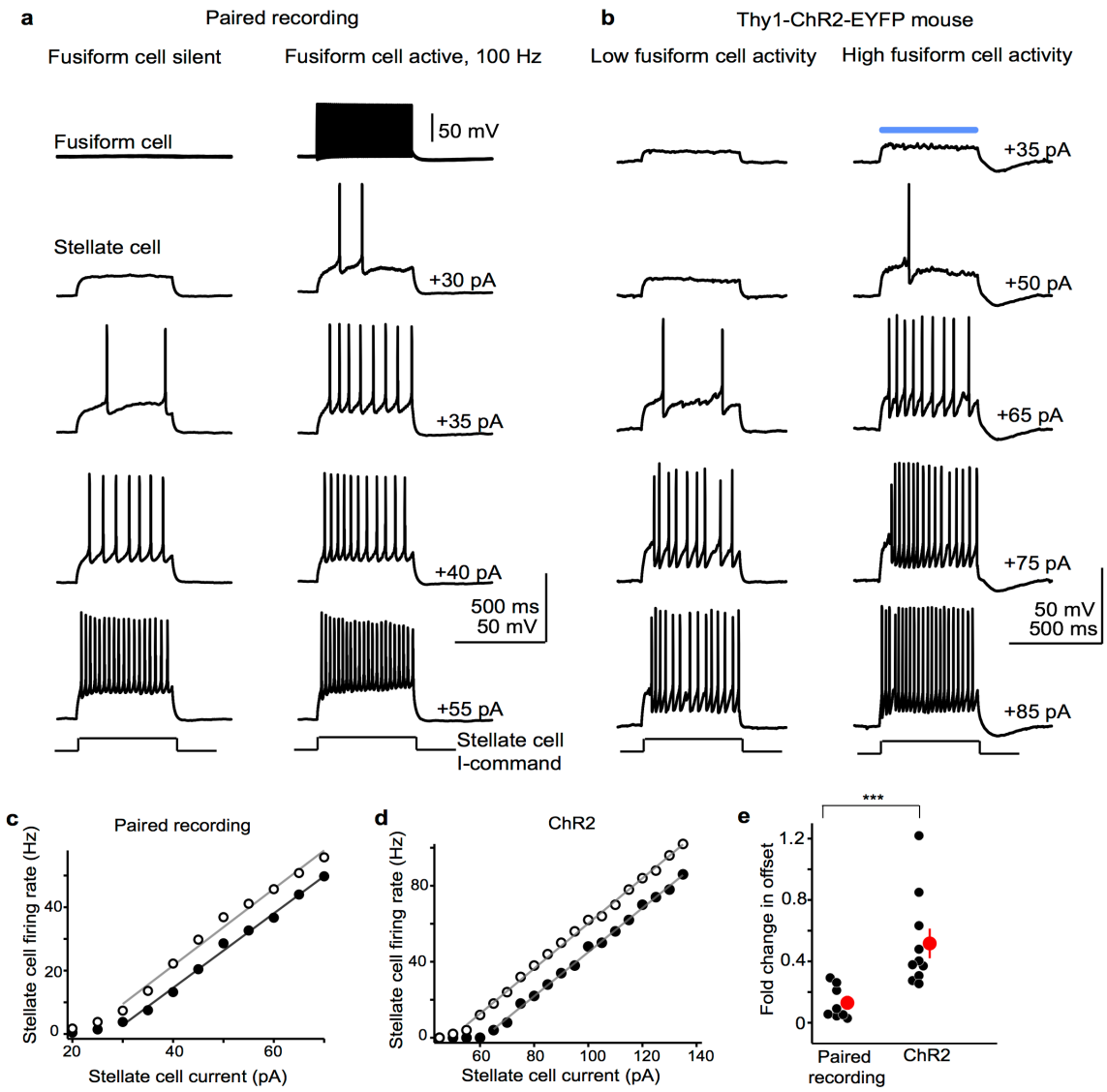
a
Paired recording
Fusiform cell silent
Fusiform cell active, 100 Hz
b
Thy1-ChR2-EYFP mouse
Low fusiform cell activity
High fusiform cell activity
Fusiform cell
Stellate cell
50 mV
+30 pA
+35 pA
+40 pA
+55 pA
+35 pA
+50 pA
+65 pA
+75 pA
+85 pA
500 ms
50 mV
50 mV
500 ms
Stellate cell
I-command
c
Paired recording
Stellate cell firing rate (Hz)
Stellate cell current (pA)
d
ChR2
Stellate cell firing rate (Hz)
Stellate cell current (pA)
e
***
Fold change in offset
Paired recording
ChR2

Figure 3.6: Fusiform cells control spike rate of stellate cells.

a) Single trials from an electrically-coupled fusiform-stellate cell pair. The stellate cell was depolarized with step pulses of increasing positive current (2.5-5 pA intervals; 500 ms duration) in absence or with simultaneous 100 Hz activity in the fusiform cell (left and right columns, respectively). Activity in the prejunctional fusiform cell increases the total number of spikes generated in the stellate cell with intermediate current steps.

b) Example single trials from a stellate cell in a Thy1-ChR2 mouse. Traces show stellate cell spiking evoked by positive current injection (500 ms) with (right) and without (left) concurrent blue light flashes (500 ms) to activate prejunctional fusiform cells.

c) Input/output curve for the pair in (a). Spike frequency (y-axis) is plotted as a function of current injection. Solid points represent values while the prejunctional cell was silent; open points are with simultaneous prejunctional fusiform cell activity. The gray lines are linear fits to the non-zero portions of the data.

d) Same as panel c, but for the ChR2 experiment. The open and filled circles represent the input-output curves of the example cell in (b) with and without simultaneous blue light flashes, respectively.

e) Summary graph plotting the normalized change in offset (x-intercept) due to fusiform cell activity in paired recordings and ChR2 experiments. Asterisks denote statistical significance. Optogenetic stimulation caused a 3.7-fold greater shift in offset compared to paired recordings ($p=0.004$, unpaired t-test).

Figure 3.7

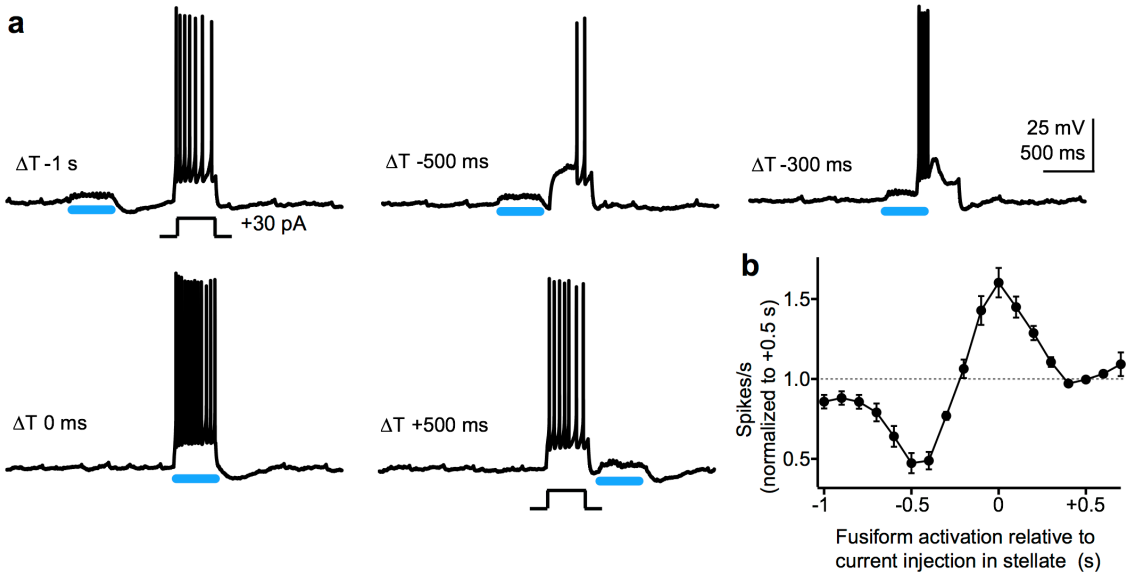

Figure 3.7: The timing of fusiform cell activity bi-directionally controls stellate cell spike output.

a) Single trials from a stellate cell in a VgluT2-ChR2 mouse where the cell was transiently driven to spike via positive current injection (400 ms). Prejunctional fusiform cells were activated by blue light (400 ms) at various times relative to the current step in the stellate cell. Negative bias current was used to prevent spontaneous firing.

b) Summary graph from 13 stellate cells in ChR2 mice plotting normalized spikes/s as a function of flash timing relative to stellate cell current injection. The data are normalized to the +500 ms data point, where the light flash (and thus, fusiform cell activation) occurred *after* the current step in the stellate cell.

Figure 3.8

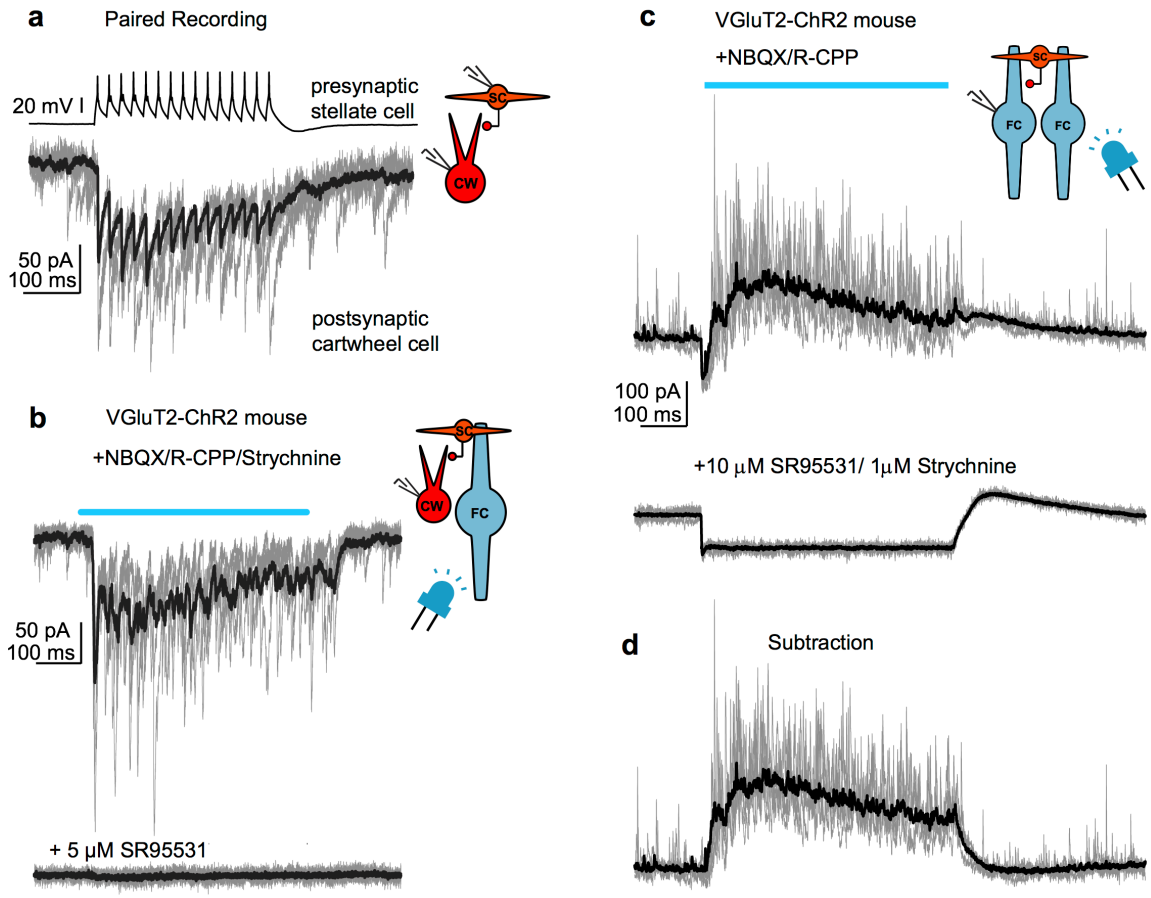

Figure 3.8: Fusiform cells generate inhibition in the DCN circuit.

a) Paired recording between a presynaptic stellate and postsynaptic cartwheel cell. GABAergic transmission was isolated with glutamate and glycinergic synaptic blockers. 15 action potentials were elicited at 50 Hz in the stellate cell, resulting in a time-locked series of IPSCs in the postsynaptic cartwheel cell. IPSCs are inward as the cartwheel cell is recorded with a Cl^- rich internal solution. Gray traces are 4 single sweeps, black is an average of 20 trials.

b) Example recording from a cartwheel cell in a VGluT2-ChR2 mouse. Top trace: Optogenetic stimulation of fusiform cells, denoted by the blue line, results in a barrage of IPSCs in the cartwheel cell. Lower trace: The $GABA_A$ receptor antagonist SR95531 blocks the optogenetically-evoked IPSCs. Gray traces are 4 single sweeps, black is an average of 10 trials in each condition.

c) Example recording from a fusiform cell in a VGluT2-ChR2 mouse. The cell is voltage-clamped at 0 mV, generating a net outward driving for Cl^- currents. Upper panel: Activating neighboring fusiform cells via blue light stimuli (500 ms) causes a powerful increase in IPSC frequency. Lower panel: IPSCs are blocked by the addition of $GABA_A$/glycine receptor blockers SR95531 and strychnine, revealing an inward photocurrent during the light stimulus. Gray traces are 5 consecutive trials. Black traces are an average of 20 to 23 trials.

d) Same example traces as those in the upper panel of (c), but with the average photocurrent digitally subtracted. Activation of neighboring fusiform cells causes an inhibitory outward current for the duration of the light stimulus.

Supplemental Figure 3.1

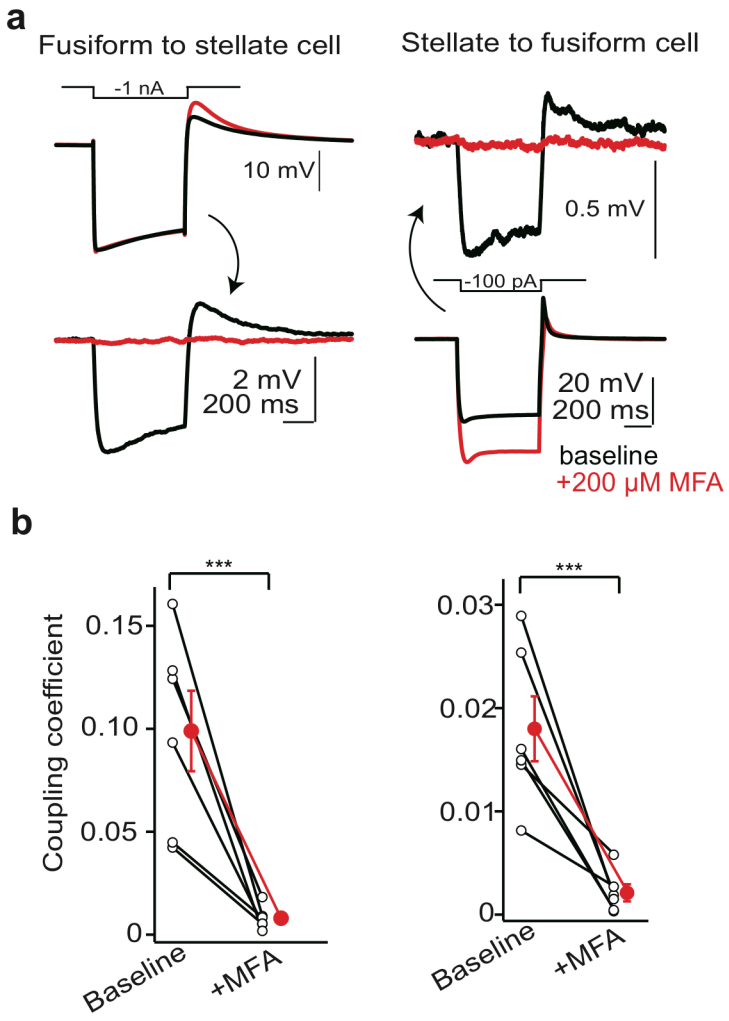

Supplemental Figure 3.1: The gap junction blocker MFA abolishes electrical coupling.

a) Average traces from a coupled fusiform-stellate cell pair (upper and lower traces, respectively). Black traces are the baseline period and red traces are after 15-30 min of incubation in the gap junction blocker MFA (100-200 µM). The increased amplitude in the stellate cell prejunctional waveform after MFA likely reflects a contribution of gap junction channels to the basal leak conductance (Vervaeke et al., 2012).

b) Summary of the coupling coefficients from six pairs before and after application of MFA. Open circles represent individual experiments, red points are mean ±SEM. Left and right panels represent fusiform-to-stellate and stellate-to-fusiform directions, respectively. MFA significantly reduced the coupling coefficient in the fusiform-to-stellate cell direction from 0.10 ±0.02 to 0.008 ± 0.002, whereas the stellate-to-fusiform coupling dropped from 0.018 ±0.003 to 0.002 ±0.001 ($p=0.005$ and 0.006, respectively, paired t-test).

Supplemental Figure 3.2

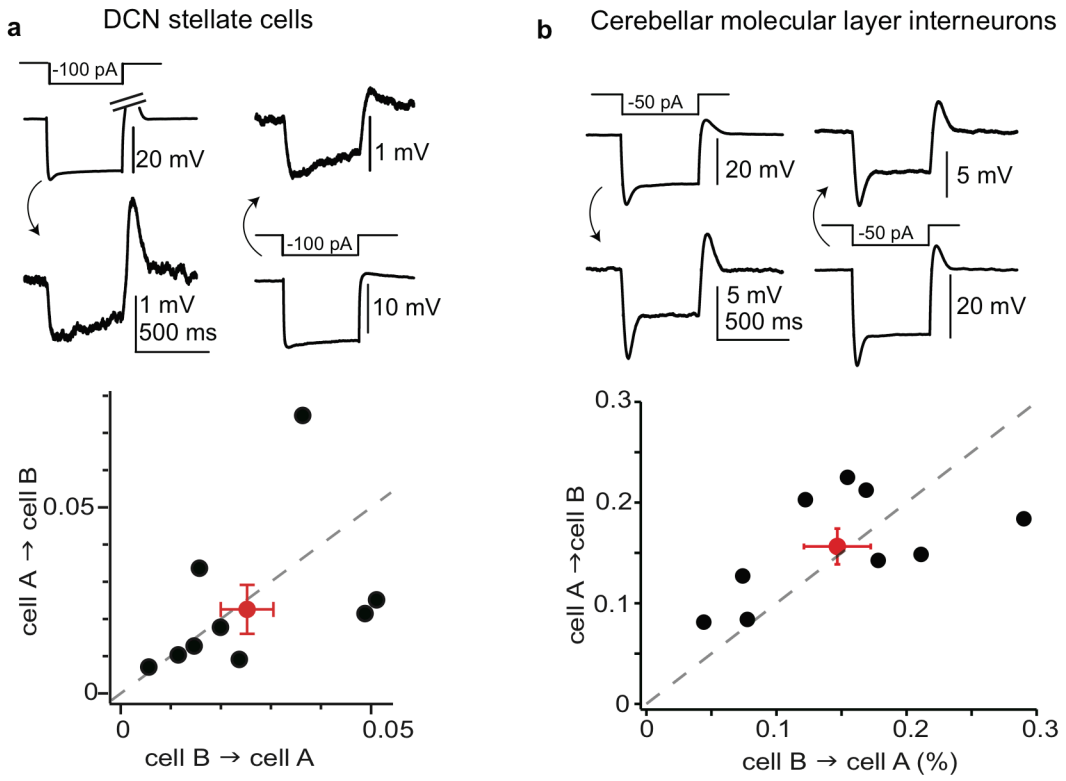

Supplemental Figure 3.2: DCN stellate cells are weakly electrically-coupled.

a) Top: Example average traces from an electrically-coupled pair of DCN stellate cells. Lower panel: Summary data plotting the coupling coefficients for 9 coupled pairs. The apparent directional asymmetry in some pairs is probably due to intrinsic variability in basal input resistance, as the group average (red point) falls on the unity line. The homologous coupling coefficient between DCN stellate cells (0.024 ±0.005, average of both directions) was significantly weaker than fusiform-to-stellate cell coupling but not significantly different from stellate-to-fusiform coupling (One way ANOVA + Tukey's

post-hoc tests). The calculated junctional conductance for homologous coupling between DCN stellate cells was 0.14±0.04 nS.

b) Top: Example average traces from a pair of cerebellar molecular layer interneurons. 9/18 pairs showed coupling, and the coupling coefficient (0.15 ±0.02) was significantly greater than in DCN stellate cells ($p<0.001$, unpaired t-test). These values are in line with previous reports(Mann-Metzer and Yarom, 1999). The junctional conductance for coupling between cerebellar stellate cells was 0.52 ± 0.07 nS.

Supplemental Figure 3.3

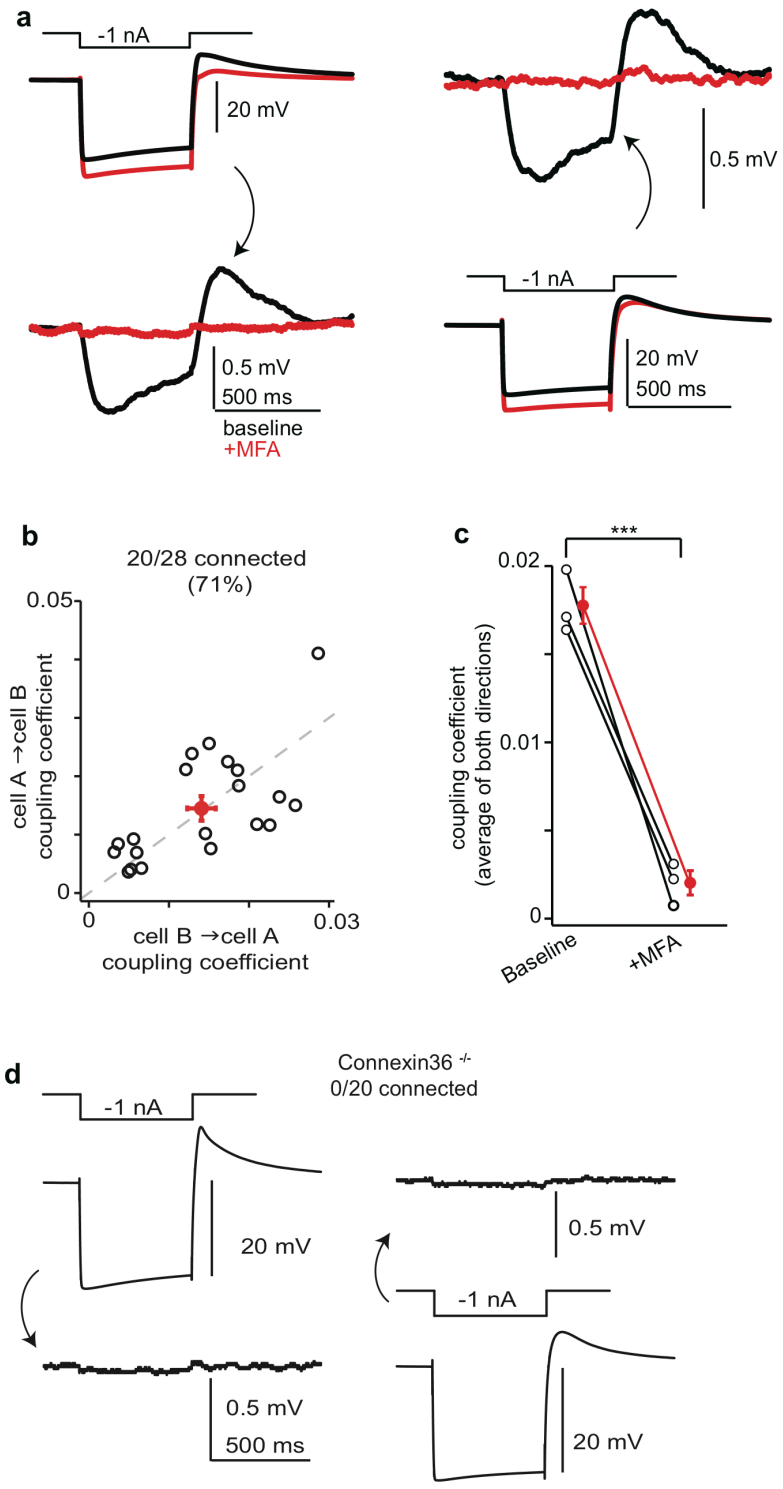

Supplemental Figure 3.3: Fusiform cells are weakly electrically coupled to one another.

a) Example average traces from a pair of fusiform cells. Current injection in one cell results in a small hyperpolarization of the other cell. Black and red traces are before and after addition of the gap junction blocker MFA, confirming that this effect is due to gap junction coupling.

b) Summary data showing the coupling coefficient of 20 similar pairs. Red symbol is mean ±SEM. Dotted gray line is unity. Homologous coupling between fusiform cells (0.014 ±0.001, average of both directions) was significantly weaker than fusiform-to-stellate cell coupling, but not significantly different than stellate-to-fusiform or stellate-to-stellate coupling (one way ANOVA and Tukey's tests). The junctional conductance for this data set was 0.50±0.07 nS.

c) Summary data showing that 100-200 μM MFA significantly reduced electrical coupling between fusiform cells (n=3 pairs; p=0.01, paired t-test.) Open symbols are individual experiments, red is mean±SEM. Asterisks denote statistical significance.

d) Average traces from a fusiform cell pair in a Cx36 -/- mouse. Electrical coupling was absent in fusiform cell pairs recorded in Cx36 -/- mice (0/20 connected; $p<0.0001$ compared to wild-type mice, chi-square test.).

Supplemental Figure 3.4

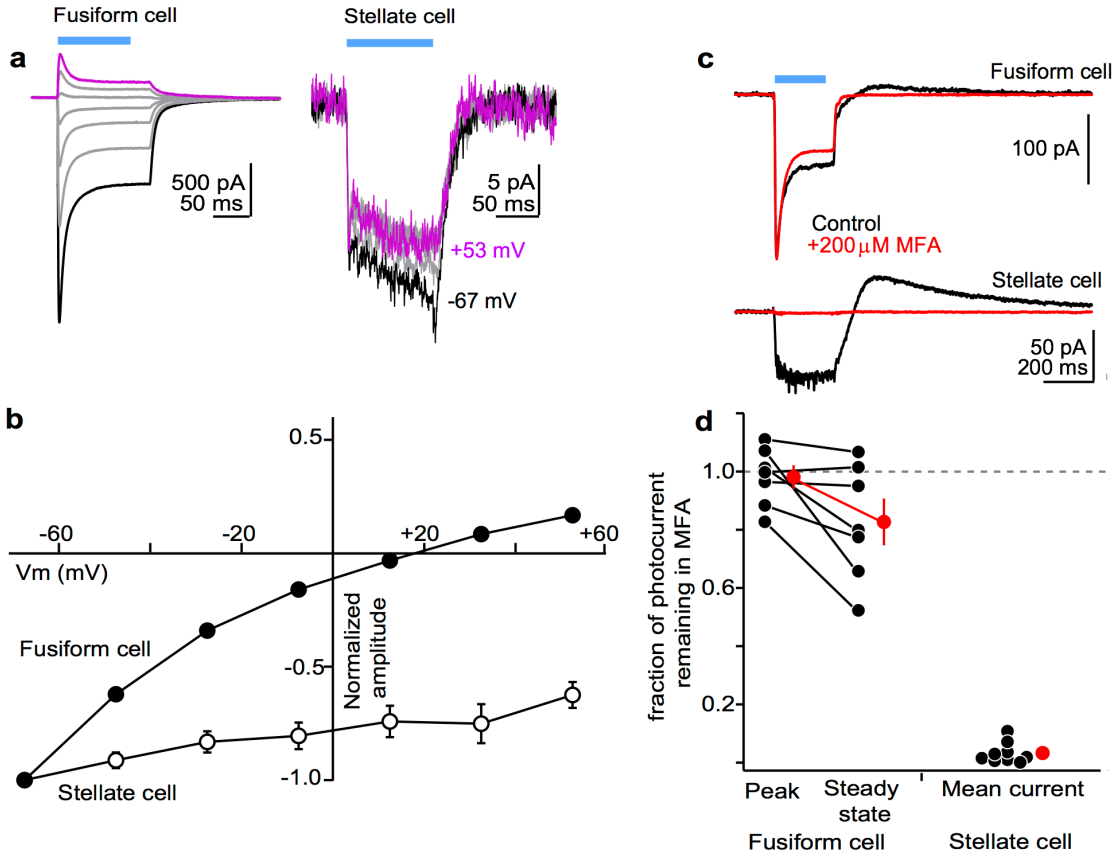

Supplemental Figure 3.4: Stellate cells do not express ChR2

a) Example average traces from a voltage-clamped fusiform (left) or stellate cell (right) at different membrane potentials. The -67 and +53 mV traces are highlighted for comparison in black and mauve, respectively. Note that the peak and steady-state photocurrents in fusiform cells are outward at +53 mV, whereas there is little change in the amplitude of the stellate cell response. Example traces are from a Thy1-ChR2 mouse, but similar results were observed in VGluT2-ChR2 mice.

b) Summary data of the IV relationship for photocurrent responses in fusiform and stellate cells from ChR2 mice (n=10 cells each, solid and open symbols, respectively) showing differential voltage-dependence of photocurrents. Stellate cell responses were persistently inward even at very positive membrane potentials, whereas fusiform cell photocurrents reversed direction. The positive reversal potential in fusiform cells may be due in part to the contribution of electrically-coupled fusiform cells that are simultaneously depolarized during the light stimulus (Supplemental Figure 3). Moreover, the dendritic arbor of fusiform cells (see example cell in Figure 3) may result in space-clamp limitations.

c) Differential block of fusiform and stellate cell light responses by the gap junction blocker MFA. Average photocurrent responses in a simultaneously recorded (uncoupled) fusiform/stellate cell pair from a Thy1-ChR2 mouse during baseline (black) and after 200 μM MFA (red). The peak photocurrent in the fusiform cell was unaffected, whereas the stellate cell response was entirely abolished. Note that MFA caused a small reduction in the steady-state fusiform cell response, and also blocked the small outward current upon light offset. This probably results from the electrical coupling of adjacent fusiform cells activated during the light stimulus.

d) Summary data showing the effects of 100-200 μM MFA on photocurrents in fusiform and stellate cells. The leftmost points show the fraction remaining in MFA (normalized to a pre-drug baseline) for the peak and steady-state amplitudes of the fusiform cell photocurrents. Black lines connect individual experiments, red points are mean±SEM. MFA had no effect on peak photocurrents (98 ± 4% remaining, n=7, p=0.7, paired t-test). MFA slightly reduced the steady state photocurrent in 4/7 experiments, although this

value was not statistically significant in grouped data (82 ± 8% remaining, p=0.08, paired t-test). The rightmost data points represent the fraction remaining of the steady-state postjunctional photocurrent in stellate cells. MFA completely abolished photocurrents in stellate cells (3 ± 1% remaining, n=9 cells, p=0.004, paired t-test).

CHAPTER 4: A SYNAPTIC EXCITATORY/INHIBITORY SEQUENCE MEDIATED BY VOLTAGE-GATED ION CHANNELS AND GAP JUNCTIONS.

Pierre F. Apostolides[1,2] & Laurence O. Trussell[2]

[1]Neuroscience Graduate Program

[2]Vollum Institute & Oregon Hearing Research Center, Oregon Health & Science University. Portland, Oregon, 97239, USA.

This chapter will be submitted as a Report to the journal *Neuron* in 2014.

Abstract

Voltage-gated ion channels act in a cell-autonomous manner to amplify, compartmentalize, and normalize synaptic signals. We show here that voltage-gated channels activated by subthreshold inputs generate an excitatory/inhibitory synaptic sequence that propagates through an electrically-coupled network. In the fusiform principal cells of the dorsal cochlear nucleus, excitatory synapses activate a persistent Na^+ current and deactivate a resting I_h conductance, leading to a striking reshaping of the synaptic potential. Voltage changes resulting from activation/deactivation of these channels subsequently propagate through gap junction channels to generate slow excitation followed by inhibition in interneurons that are electrically-coupled to fusiform cells. This gap junction-mediated transmission of voltage-gated signals from principal cells can account for the majority of glutamatergic input onto interneurons. Consequently, synaptic-like, subthreshold events from principal neurons are sufficient to drive spiking in local interneurons. Thus, the interaction between excitatory synapses and voltage-gated channels transmits a time-locked, biphasic synaptic sequence throughout an electrically-coupled network.

Introduction

Feedforward inhibition is a common phenomenon observed in diverse neuronal microcircuits, in which a group of presynaptic axons generates an excitatory postsynaptic potential (EPSP) onto principal cells and local inhibitory interneurons. If the EPSP onto the interneuron generates an action potential, GABA release from the interneuron onto its targets will cause an inhibitory postsynaptic potential (IPSP) that arrives shortly after the EPSP in principal cells (Andersen et al., 1963; Pouille and Scanziani, 2001; Kuo and Trussell, 2011). This rapid excitatory/inhibitory (E/I) synaptic sequence controls the temporal integration of subthreshold EPSPs, the timing of action potentials, and gain of single or groups of neurons (Isaacson and Scanziani, 2011). Thus, the biophysical mechanisms controlling the timing and magnitude of interneuron spiking are critical determinants of synaptic integration in principal cells.

Previous studies show that active conductances in principal cells control the timecourse of subthreshold EPSPs (Stuart and Sakmann, 1995; Magee, 1999; Carter et al., 2012) and IPSPs (Stuart, 1999), suggesting that voltage-gated channels can profoundly impact the temporal integration and relative duration of E/I sequences. Given that many types of neuron are electrically-coupled via gap junction channels (Bennett and Zukin, 2004), positive and negative voltage deflections can spread laterally from one neuron to multiple electrically-coupled partners. This implies that voltage-gated channels in single neurons can shape synaptic transmission in a cell-autonomous as well as network manner. However, previous studies investigating the of spread of signals through gap junctions have focused mostly on action potentials, and it remains unclear if

subthreshold events in one neuron can spread complex synaptic E/I sequences through electrically-coupled networks.

We recently showed that the inhibitory stellate interneurons of the dorsal cochlear nucleus (DCN) form an electrically-coupled network with the circuit's excitatory projection neurons (fusiform cells; Apostolides and Trussell, 2013). Given that fusiform cells express several types of voltage-gated ion channels (Molitor and Manis, 2003; Leao et al., 2012; Rusznák et al., 2013), we asked whether subthreshold activation of voltage-gated channels by synaptic stimuli in fusiform cells propagates to electrically-coupled interneurons. Using whole-cell patch clamp recordings in acute slices of mouse DCN, we show that a subthreshold Na^+ conductance controls the amplitude and width of EPSPs in fusiform cells, and propagation of this synaptic Na^+ current through gap junctions is a major determinant of the time course and amplitude of excitatory transmission onto stellate cells. Subthreshold events in fusiform cells subsequently deactivated HCN channels that control the resting membrane potential (Rusznák et al., 2013), thereby hyperpolarizing the fusiform cell following an EPSP and generating a net outward current in stellate cells following an EPSP. Consequently, synaptic-like events that were subthreshold in fusiform cells reliably generated action potentials in electrically-coupled stellate cells. Thus, subthreshold activation of a persistent Na^+ conductance and deactivation of HCN channels in principal cells generates a time-locked E/I sequence through an electrically-coupled network to control spiking of local interneurons.

Methods

Electrophysiology

All experiments were performed with prior approval from Oregon Health & Science University's IACUC. Briefly, 250-300 μm thick coronal sections of the DCN were prepared from p15-p25 mice of either sex from the following strains: C57/Bl6, Thy1-ChR2-YFP, VGluT2-ChR2-YFP, and connexin36 -/- mice (or their wild-type littermates). The brain was submerged and sliced in an ice-cold cutting solution containing (in mM): 87 NaCl, 25 $NaHCO_3$, 25 glucose, 75 sucrose, 2.5 KCl, 1.25 NaH_2PO_4, 0.5 $CaCl_2$, 7 $MgCl_2$, 0.05 R-CPP, and bubbled with 5% CO_2/95% O_2. Slices were subsequently transferred to a holding chamber and allowed to recover for 30-45 min at 34^o C in an artificial cerebrospinal fluid (ACSF) solution containing (in mM): 130 NaCl, 2.1 KCl, 1.7 $CaCl_2$, 1 $MgSO_4$, 1.2 KH_2PO_4, 20 $NaHCO_3$, 3 Na-HEPES, 10-12 glucose, 0.05 R-CPP, bubbled with 5% CO_2/95% O_2 (300-310 mOsm). After recovery, slices were stored at 22-24^o C until recording and experiments were performed within 5 hours of slice preparation.

Slices were placed in a recording chamber and continuously perfused with the ACSF solution described above, heated to 31-33^o C using an inline heater (3-5 ml/min). All experiments except for those in Figure 3A were performed in the presence of inhibitory synaptic blockers (10 μM SR95531 and 1-2 μM strychnine). Additionally, NMDA receptors were blocked in most experiments with 5 μM R-CPP. Stellate and fusiform cells were visually identified using previously established criteria (Apostolides and Trussell, 2013). The pipette internal solution for voltage-clamp experiments contained (in

mM) 64.5 $CsMeSO_3$, 30 CsFl, 5 TEA-Cl, 5 QX314-Cl, 5 Cs_4BAPTA, 4.8 $MgCl_2$, 4 ATP, 0.5 GTP, 10 Tris-phosphocreatine, 10 HEPES, pH 7.2-7.3 with CsOH. In some experiments, CsFl was replaced with 15 $CsMeSO_3$ and 15.5 CsCl. The internal solution for current clamp experiments in fusiform cells contained 113 K-gluconate (Or 113 $KMeSO_3$), 4.8 $MgCl_2$, 4 ATP, 0.5 Tris-GTP, 14 Tris-phosphocreatine, 0.1 EGTA, 10 HEPES, pH 7.2-7.3 with KOH, ~290 mOsm. In some experiments, 15.5 KCl was substituted for equimolar K-Gluconate or $KMeSO_3$. Optogenetic stimulation of fusiform cells was performed as described in (Apostolides and Trussell, 2013). Series resistance (<30 MOhm) was compensated in the majority of voltage-clamp experiments (60-80% correction, 90% prediction. Bandwith = 3 kHz). Data were not included if the series resistance varied >20-25% over the course of the recording. In current clamp , pipette capacitance was canceled and bridge balance was maintained.

Parallel Fiber stimulation

A bipolar metal electrode (FHC) or theta-glass stimulating electrode was placed in the DCN molecular layer >100 μm from the recorded cell. The distance between the two tips of the stimulating electrodes was ~20-50 μm for theta glass electrodes and 100 μm for the bipolar metal electrode. The size of the electrode and distance from the cell proved to be critical determinants for whether we recruited the gap junction mediated component of parallel fiber transmission. Indeed, our previous study characterizing chemical transmission onto DCN stellate cells did not report slow inward or outward components of parallel fiber transmission (Apostolides & Trussell, in revision). This discrepancy arises from the fact that the experiments in the previous study were performed using small theta glass stimulating electrodes (<10 μm distance between tips) placed in closer

proximity (20-40 μm) to the stellate cell. Those experiments therefore preferentially activated parallel fibers on the recorded stellate cells, with minimal contribution from synapses onto prejunctional fusiform cells. We explicitly tested this by varying the distance of the stimulating electrode from the recorded cell. EPSCs evoked when the electrode was 20-40 μm from the cell had significantly smaller half-widths than EPSCs evoked >100 μm away from the cell (n=5 cells. 20-40 μm half-width: 2.2±0.7 ms. 100-200 μm: 43.1±9.0 ms, p=0.01, paired t-test)

Data Acquisition and analysis

Data were acquired in PClamp9 using a multiclamp 700B amplifier and Digidata 1322A analog-digital converter. Traces were sampled at 50 kHz, online filtered at 10-20 kHz, and filtered at 1-10 kHz during offline analysis. All traces displayed as averages of multiple trials unless stated otherwise. EPSC were generated using Axograph X (rise: 0.2-0.7 ms, monoexponential decay: 3-7 ms). Statistical significance was set at $p<0.05$ and determined using methods listed in the main text.

Reagents

R-CPP, SR95531, NBQX, and TTX were purchased from Abcam. Strychnine was from Sigma-Aldrich.

Results

Glutamate release generates a non-canonical excitatory/inhibitory sequence in DCN stellate cells.

DCN stellate and fusiform cells receive excitatory synapses from granule cell parallel fibers that course through the molecular layer (Figure 1A; (Wouterlood et al., 1984). In voltage-clamped stellate cells, stimulating parallel fibers with a single shock from a bipolar electrode (see Methods) caused a multiphasic, inward excitatory postsynaptic current (EPSC) consistently followed by an outward current (Figure 1B). All experiments were performed in the presence of strychnine and SR95531, indicating that the outward component was not due to glycine or $GABA_A$ receptors. Furthermore, stellate cells in these experiments were recorded with a Cs-based internal solution that should block GIRK channels and establish a net inward K^+ driving force, arguing that the slow outward current is not due to $GABA_B$ receptor activation. Interestingly, the AMPA receptor antagonist NBQX (10 μM) abolished the inward and outward components (n=7), indicating that glutamate transmission generates both excitatory and inhibitory responses in stellate cells (Figure 1B, red trace).

Close inspection of the voltage-clamp traces revealed that from trial-to-trial, parallel fibers variably generated two similar, but non-identical inward current responses. Some events had an initial rapidly rising component, typical of AMPA receptor-mediated transmission, followed by the slow inward and outward phases. Other events lacked the initial fast phase and thus had much slower rise times, but the slow decay of the inward component and subsequent outward components were similar (n=11; Figure 1B, right.

Black and gray traces, respectively). The stimulation intensity in these experiments was adjusted to evoke initial fast-rising inward currents in approximately half of the trials; we thus interpret the variable appearance of the fast inward component as reflecting quantal fluctuation of release from single parallel fiber synapses on the recorded stellate cells. Given that AMPA EPSCs in stellate cells display rapid rise and decay kinetics (Carter and Regehr, 2002; Apostolides & Trussell, 2014, ms in revision), the drastically slower kinetics and comparatively invariant nature of the later synaptic components shown in Figure 1B suggest that they reflect signals transmitted through gap junctions and mediated by a larger population of synapses on fusiform cells.

The slow rising EPSCs had smaller absolute peak amplitudes compared to events containing the initial fast phase. However, the slow component accounted for 75±7% of the total inward charge transfer of the total compound EPSC (calculated as the ratio of the inward charge in the gray trace to that of the black trace), suggesting that propagation of parallel fiber inputs from fusiform cells represents the majority of synaptic excitation for stellate cells. In agreement with this interpretation, the same experiment performed in DCN slices from mutant mice lacking electrical coupling in the DCN (connexin36 -/- mice; cx36 -/-) revealed that EPSCs from stellate cells fluctuated between a purely fast inward current or no current at all (n=12 cells; Figure 1C). Interestingly, the slow outward component was also absent in cx36 -/- mice, indicating that it was similarly mediated by synaptic activity in prejunctional fusiform cells.

The inward charge transfer of compound EPSCs from cx36 -/- mice was significantly smaller compared to EPSCs from WT mice (Figure 1D, left panel). However, the total charge and peak amplitude of the fast AMPA component (representing parallel fiber

transmission onto the voltage-clamped stellate cell) was similar in WT and cx36 -/- mice, arguing that these differences were not due to general deficits in parallel fiber transmission in mutant mice (Figure 1D, middle and right panels). In summary, our data show that glutamate synapses directly onto stellate cells account for only a quarter of the excitatory charge from sparse parallel fiber activity. Instead, the majority of excitatory transmission is generated by AMPA receptors located on prejunctional fusiform cells.

A subthreshold Na^+ conductance shapes the kinetics and controls the gain of subthreshold EPSPs in fusiform cells.

Fusiform cells express a persistent Na^+ current that is activated at subthreshold voltages (Leao et al., 2012), and previous studies have shown that subthreshold EPSPs can activate Na^+ channels in other neurons (Stuart and Sakmann, 1995; Carter et al., 2012). If subthreshold EPSPs in fusiform cells activate the persistent Na^+ conductance, then the slow inward component of parallel fiber transmission observed in stellate cells (Figure 1B) would not merely represent a passive depolarization of fusiform cell dendrites during EPSPs. Instead, a significant fraction of this slow synaptic excitation might be due to the subthreshold Na^+ current in prejunctional fusiform cells.

We tested whether subthreshold EPSPs in fusiform cells activate Na^+ channels by injecting EPSC-like waveforms through the patch pipette and quantifying the effect of the Na^+ channel blocker tetrodotoxin (TTX, 1 μM) on the resulting artificial EPSPs (aEPSPs). As expected, increasing the amplitude of the EPSC waveform generated progressively larger subthreshold aEPSPs (n=7 cells, Figure 2A,B) and eventually led to

spike generation (not shown). Interestingly, a small afterhyperpolarization (AHP) often followed the aEPSPs (Figure 2A), suggesting that the slow outward current observed in stellate cells during the experiments of Figure 1 could in principle be generated by subthreshold events from prejunctional fusiform cells.

In agreement with a major role for subthreshold Na^+ currents in shaping excitatory transmission in fusiform cells, aEPSP half-widths were markedly dependent on the EPSC waveform amplitude: aEPSPs evoked with 100-200 pA waveforms had significantly briefer half-widths than aEPSPs evoked with 250-700 pA waveforms (Figure 2A,B. 44±8 vs. 77±14 ms, p=0.003, paired t-test). Blocking Na^+ channels with TTX significantly reduced only the half-width of the larger aEPSPs, thereby abolishing the amplitude-dependence of aEPSP half-width (Figure 2B, left panel. 100-200 pA in TTX: 33±7 ms; 250-700 pA in TTX: 30±5 ms, p=0.16 and p=0.0002 compared to baseline, respectively. Two-way repeated measures ANOVA + Sidak's post-hoc test). Furthermore, linear fits to the aEPSP peak amplitude values revealed that Na^+ channels control the amplitude gain of subthreshold events, as the slope of the input/output function was significantly reduced in TTX (Figure 2B, right panel). Thus, Na^+ currents in fusiform cells are activated by subthreshold depolarizations to control the amplitude and temporal integration properties of excitatory signals. These data predict that voltage-gated Na^+ channels in prejunctional fusiform cells should play a major role in shaping parallel fiber transmission onto electrically-coupled stellate cells.

If Na^+ channels have such a profound effect on the shape of aEPSPs, subthreshold events in fusiform cells might transmit a TTX-sensitive current to electrically-coupled stellate cells. We explicitly tested this possibility by recording from coupled fusiform-

stellate cell pairs and driving aEPSPs in the fusiform cell while voltage-clamping the stellate cell (Figure 2C). The aEPSPs generated time-locked postjunctional inward currents in stellate cells, showing that subthreshold synaptic-like events in fusiform cells are reliably transmitted through gap junction channels (n=6 pairs. Figure 2C, black trace). As expected from the results of Figure 2 A and B, TTX significantly reduced the peak amplitude and half-width of aEPSPs in the prejunctional fusiform cells (to 73±3% and 32±5% of baseline, respectively). This was mirrored by a prominent reduction in the peak amplitude and charge transfer of the postjunctional inward currents in voltage-clamped stellate cells (Figure 2C,D). This effect was not mediated by the activation of Na^+ channels on stellate cells due to voltage-clamp errors, as Na^+ channels were pre-blocked in all experiments by the addition of QX314 (5 mM) specifically to the stellate cell internal solution. These data show that sub-threshold activation of voltage-gated Na^+ channels in single neurons shapes the amplitude and time course of excitatory transmission in a cell-autonomous and network-wide fashion.

AHPs following sub- and supra-threshold responses in fusiform cells are mediated by the deactivation of I_h.

The AHP following subthreshold excitatory events in fusiform cells (Figure 2A) is interesting as it represents "feedfoward" off-response that could potentially generate the slow outward current seen in stellate cells (Figure 1B). Notably, the half-width of the subthreshold AHPs following aEPSPs (352±24 ms, n=19 cells) resembled that of the suprathreshold fusiform cell post-spike burst AHP reported in our previous study

(406±58 ms; (Apostolides and Trussell, 2013). Furthermore, the gap junction-mediated slow outward current following EPSCs in stellate cells (Figure 1B) closely resembles the current mediated by gap junction propagation of the aforementioned fusiform cell post-spike burst AHP (Apostolides and Trussell, 2013). Together, these observations suggest that the same biophysical mechanism underlies sub and supra-threshold AHPs in fusiform cells, and that the resulting voltage deflection generates the inhibitory off-response in electrically-coupled interneurons.

Given a recent study showing that HCN (I_h) channels control the resting membrane potential of fusiform cells (Rusznák et al., 2013), we hypothesized that the AHP represents the deactivation of HCN channels. Because HCN channels activate upon hyperpolarization and deactivate during depolarization, action potential trains or slow depolarizations will deactivate the HCN channels that are open at rest and transiently hyperpolarize below the resting potential at the end of an excitatory event. The decay kinetics of the AHP would therefore represent the re-activation of HCN channels upon a transient hyperpolarization. We first tested whether the HCN channel blocker CsCl (2-3 mM) had a significant effect on spike-driven AHPs in fusiform cells. Bath application of CsCl hyperpolarized fusiform cells, in agreement with Rusznák et al. (2013). We injected positive bias current in the presence of CsCl to maintain the cell's membrane potential near its baseline value (n=6 cells. Pre-CsCl: -73.1±1.8 mV; post CsCl: -73.5±1.0 mV. p=0.63, paired t-test), but the AHP was reversibly reduced to 53±5% of baseline (Figure 3A, n=6 cells). Thus, hyperpolarizations following the deactivation of HCN channels mediates approximately half of the suprathreshold AHP in fusiform cells.

Can subthreshold events also deactivate HCN channels to generate AHPs in fusiform cells? We next tested the effect of CsCl on the AHP following subthreshold aEPSPs (e.g., Figure 2A). As expected, CsCl application led to a hyperpolarization of fusiform cells in these experiments (n=7 cells. Baseline: -70.3±1.4 mV. CsCl: -76±3.4 mV). Surprisingly, we also noticed that CsCl also caused a concomitant decrease in the fusiform cell's input resistance, which was largely reversed by injecting positive bias current to return the membrane potential near its baseline level (baseline: 93.2±10.8 MOhm, CsCl: 57.2±6.8 MOhm, CsCl + bias current: 88.3±13 MOhm. p=0.002, one-way repeated measures ANOVA + Bonferroni test comparing baseline and CsCl; n.s. comparing baseline and CsCl + bias current. Membrane potential in CsCl + bias current condition: -70.0±1.4 mV). This voltage-dependent drop in membrane resistance is probably due to an increased conductance through inward rectifier K^+ channels, as described previously (Leao et al., 2012).

A decrease in membrane resistance in tandem with a hyperpolarization away from the activation range for Na^+ currents that shape subthreshold events (Figure 2) is expected to alter the timecourse of aEPSPs. In agreement, CsCl significantly reduced the amplitude and half-width of aEPSPs, and returning the membrane potential to near baseline values with positive bias current largely reversed the effects of CsCl (n=7, Figure 3B). However, CsCl almost completely abolished the subthreshold AHP, and this effect was not reversed by injecting positive bias current (Figure 3B + inset).

We next tested whether fusiform cell AHPs generate HCN-mediated outward currents in voltage-clamped stellate cells by recording from mice expressing channelrhodopsin2 specifically in fusiform cells (see Methods). In these mice, blue light stimuli generate

biphasic postjunctional photocurrents in stellate cells that are due to spike trains in prejunctional fusiform cells (Apostolides and Trussell, 2013). These photocurrents are characterized by a steady state inward component followed by a slow outward current upon light termination. CsCl reversibly reduced the peak amplitude of the outward component (n=7, Figure 3C), confirming that HCN-mediated currents are reliably transmitted to stellate cells.

Altogether, the results of panels A-C show that sub- and supra-threshold AHPs in fusiform cells are due to a transient hyperpolarization following the deactivation of HCN channels during depolarizing events, and this HCN-mediated inhibition propagates to electrically-coupled interneurons. Furthermore, the unusual voltage-dependence of the aEPSP half-width (Figure 3B) highlights a novel role for HCN channels in determining the integration properties of subthreshold events by setting the resting membrane potential near the activation range for a persistent Na^+ current. Thus, HCN channels in fusiform cells might shape EPSCs in electrically-coupled stellate cells in two ways: Tonic HCN channel activity would determine the half-width of the slow parallel fiber EPSC in stellate cells by controlling whether parallel fibers onto fusiform cells activate a subthreshold Na^+ conductance, whereas transient deactivation of these channels following fusiform cell EPSPs would generate the slow outward current (Figure 1B).

In agreement with a permissive role for HCN channels in controlling the activation of a subthreshold Na^+ current during synaptic events, CsCl reduced the duration and total charge transfer of parallel fiber-evoked inward currents in stellate cells (Figure 3D). A similar reduction was observed with another HCN channel blocker (ZD7288, 20 μM. 29±2% of baseline remaining, n=4, $p<0.0001$, one sample t-test. Data not shown). CsCl

also blocked the delayed outward current (Figure 3D, n=8 cells), indicating that this delayed inhibition following parallel fiber EPSPs is mediated by fusiform cell HCN channels. A similar block of the outward current was also observed with ZD7288 (n=4; p=0.004, one sample t-test). Thus, the interplay between subthreshold Na^+ currents, I_h, and gap junction coupling generates a synaptic E/I sequence in local interneurons that persists for several hundred milliseconds.

Subthreshold events in fusiform cells drive stellate cell spiking

The lowpass filter properties of gap junction channels predict that slow events such as subthreshold EPSPs might be significantly more potent than action potentials in regulating the membrane potential of postjunctional neurons. In agreement, paired current-clamp recordings revealed that subthreshold aEPSPs evoked in fusiform cells caused significantly larger depolarizations than action potentials in electrically-coupled stellate cells, even though the peak amplitude of the prejunctional spike was >8 fold larger than the prejunctional aEPSP (n=7 pairs, data not shown. Postjunctional/prejunctional aEPSP coefficient: 0.228±0.052. Postjunctional spikelet/prejunctional spike coefficient: 0.009±0.002, p=0.004, paired t-test. Absolute aEPSP amplitude in fusiform cell: 9.2±0.7 mV, spike: 75.3±2.1 mV).

These observations suggest that synaptic stimuli that do not drive spikes in fusiform cells may nevertheless bring the membrane potential of electrically-coupled stellate cells above spike threshold. We tested this idea by recording from electrically-coupled pairs, evoking aEPSPs in prejunctional fusiform cells, and quantifying the number of spikes per

50 ms bin in postjunctional stellate cells. As predicted, subthreshold aEPSPs in fusiform cells resulted in time-locked spikes in stellate cells (n=7 pairs, Figures 4A-D). In some pairs we noticed a reduction in spike rate during the ~200-400 ms following the aEPSP, corresponding to the timing of the subthreshold AHP. However, this reduction was not statistically significant in grouped data. These data show that subthreshold synaptic events in a single principal neuron are sufficient to drive spiking in electrically-coupled interneurons, thereby increasing the dynamic range over which presynaptic parallel fibers recruit local inhibition. Furthermore, these data suggest that although the depolarizing phase of EPSPs from single fusiform cells can drive spiking, subthreshold AHPs are less able to block spiking. Instead, a significant reduction in stellate cell spike rate may only occur after spike-driven AHPs, or may require simultaneous subthreshold EPSPs in multiple prejunctional fusiform cells.

Discussion

We have shown that the strength and kinetics of parallel fiber transmission onto DCN stellate cells are determined in a cell-autonomous as well as network manner. Specifically, we find that parallel fiber activity generates an excitatory/inhibitory synaptic sequence in stellate interneurons that is mediated by the passive spreading of synaptically-triggered, voltage-gated events from prejunctional fusiform cells.

Stellate cells express fast-gating, Ca^{2+}-permeable AMPA receptors (Apostolides & Trussell, in revision), but the shape of EPSCs can be surprisingly slow (Figure 1). We find that a Na^{+} current activated by subthreshold EPSPs in fusiform cells accounts for this

paradox. This is evidenced by the fact that >70% of the EPSC charge transfer in stellate cells is mediated by subthreshold activation of Na^+ channels in fusiform cells. Our experiments establish that voltage-gated channels on neighboring neurons are a major source of excitation in electrically-coupled networks, and that subthreshold activity in single prejunctional neurons is sufficient to drive the postjunctional membrane potential above spike threshold. Thus, the lateral spread of subthreshold events from fusiform cells may be the main source of excitation for stellate cells *in vivo*. Furthermore, deactivation of the resting HCN conductance in fusiform cells caused a net outward current in stellate cells, highlighting a novel biophysical mechanism by which excitatory synapses generate complex synaptic sequences of excitation/inhibition.

What is the function of the much briefer, direct parallel fiber synaptic responses in stellate cells? We found that these are more prominent under conditions in which small numbers of fibers are activated: careful, local placement of stimulus electrodes exclusively activates fast EPSCs in stellate cells (see Methods). Weak and strong activation of parallel fibers may result in very different types of postsynaptic responses in stellate cells. However, in a previous study it was observed that individual parallel fibers only rarely contacted both the cartwheel interneurons and their synaptically-coupled, feed forward target fusiform cell (Roberts and Trussell, 2010). If this is also true of stellate and fusiform cells it would suggest that stellate cells may receive profoundly different synaptic signals depending on the population, not just number, of parallel fibers that are active.

Electrical coupling, HCN channels, and subthreshold activation of TTX-sensitive Na^+ channels are all common features of neurons found in diverse brain regions such as the

thalamus (Parri and Crunelli, 1998), olfactory bulb (Balu et al., 2004), and locus coeruleus (Christie et al., 1989; de Oliveira et al., 2010). Together with our current results, these findings imply that the interplay between cell-autonomous activation of voltage-gated channels and network-wide gap junction coupling may shape synaptic transmission in diverse neuronal microcircuits.

Acknowledgements:

We thank Michael Bateschell and Ruby Larisch for help with mouse colony management, and all members of the Trussell lab for helpful discussions during the course of these experiments. Funding was provided by NIH grants R01DC004450 and R01NS28901 (L.O.T.) and 1F31DC012222 (P.F.A.)

Author contributions:

P.F.A. performed the experiments. P.F.A. and L.O.T. designed the study, analyzed and interpreted the results, and wrote the paper.

Figure 4.1

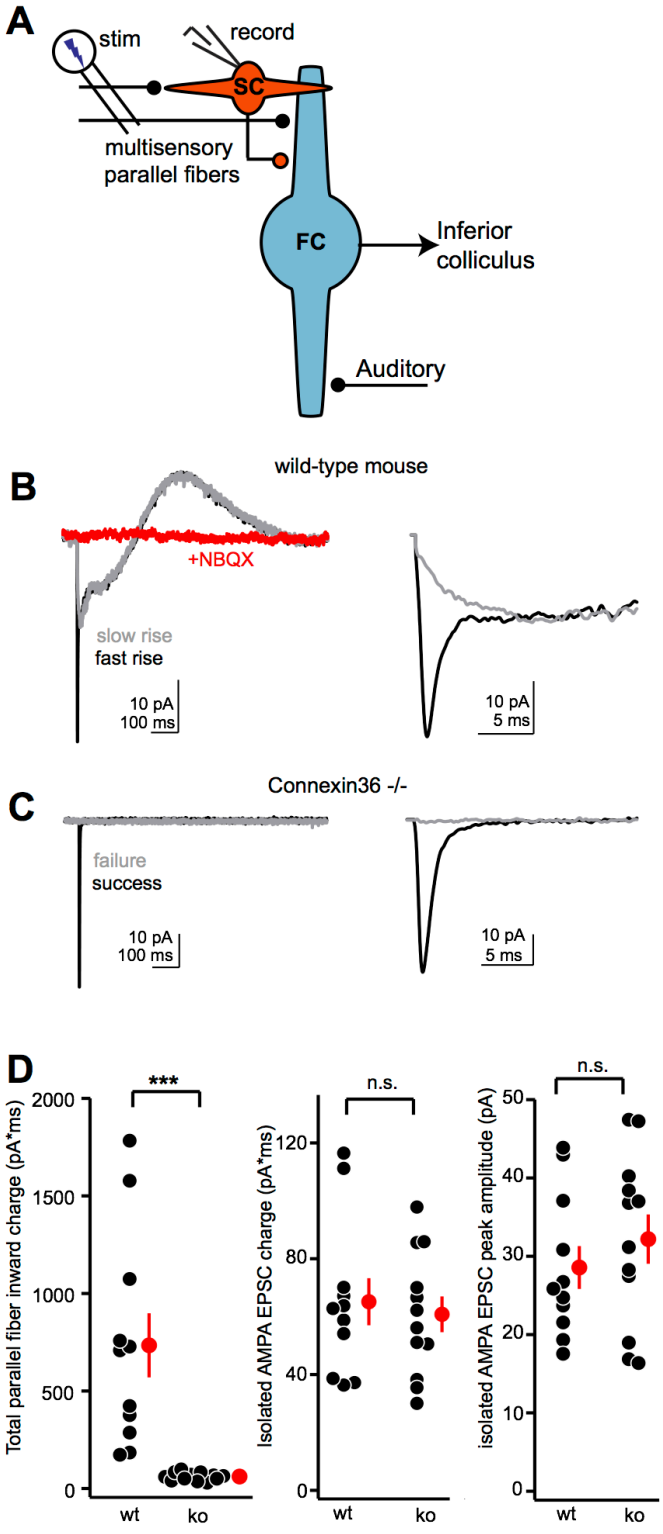
A
stim
record
SC
multisensory
parallel fibers
FC
Inferior
colliculus
Auditory
B
wild-type mouse
+NBQX
slow rise
fast rise
10 pA
100 ms
10 pA
5 ms
C
Connexin36 -/-
failure
success
10 pA
100 ms
10 pA
5 ms
D
***
n.s.
n.s.
Total parallel fiber inward charge (pA*ms)
Isolated AMPA EPSC charge (pA*ms)
isolated AMPA EPSC peak amplitude (pA)
2000
1500
1000
500
0
120
80
40
0
50
40
30
20
10
0
wt
ko
wt
ko
wt
ko

Figure 4.1: Parallel Fiber transmission generates an E/I sequence mediated by AMPA receptors.

A) Diagram of the DCN circuit and experimental set-up. The projection neurons integrate excitatory synapses from the auditory nerve and cerebellum-like granule cell parallel fibers. The latter pathway also contacts GABAergic stellate cells that are electrically-coupled to fusiform cells. A bipolar stimulating electrode is placed in the molecular layer to activate parallel fibers synapses.

B) A single parallel fiber shock generates an E/I sequence in stellate cells that is entirely blocked by bath application of the AMPA receptor antagonist NBQX (10 μM). Black trace is an average of events that had an initial rapidly rising component, whereas the gray trace is an average of events lacking the fast component. The right panel shows the two types of events on a faster time base to highlight the drastic difference in rise times.

C) Parallel fiber EPSCs in connexin36 -/- mice lack the slow inward and outward components. Black and gray traces represent averages of trials in which the fast component either succeeded or failed, respectively.

D) Quantification of EPSCs from wild-type and connexin36 -/- mice. Left panel: The total inward charge transfer of parallel fiber EPSCs in wild-type mice was on average -734±164 pA*ms (n=11), whereas it was only -62±6 pA*ms in the KO mice (n=12). Middle and right panels: The inward charge transfer and peak amplitude of the fast rising AMPA EPSC from parallel fiber synapses directly on stellate cells was not significantly different between wild-type and KO mice (WT charge and peak amplitude: -65±8 pA*ms, -29±3 pA. KO charge and peak amplitude: -60±6 pA*ms, -32±3 pA. p=0.67 and

0.39, respectively. unpaired t-test). The fast rising AMPA EPSC was isolated by subtracting the average of slowly-rising events from the average of fast rising events (e.g., black trace minus gray trace).

Figure 4.2

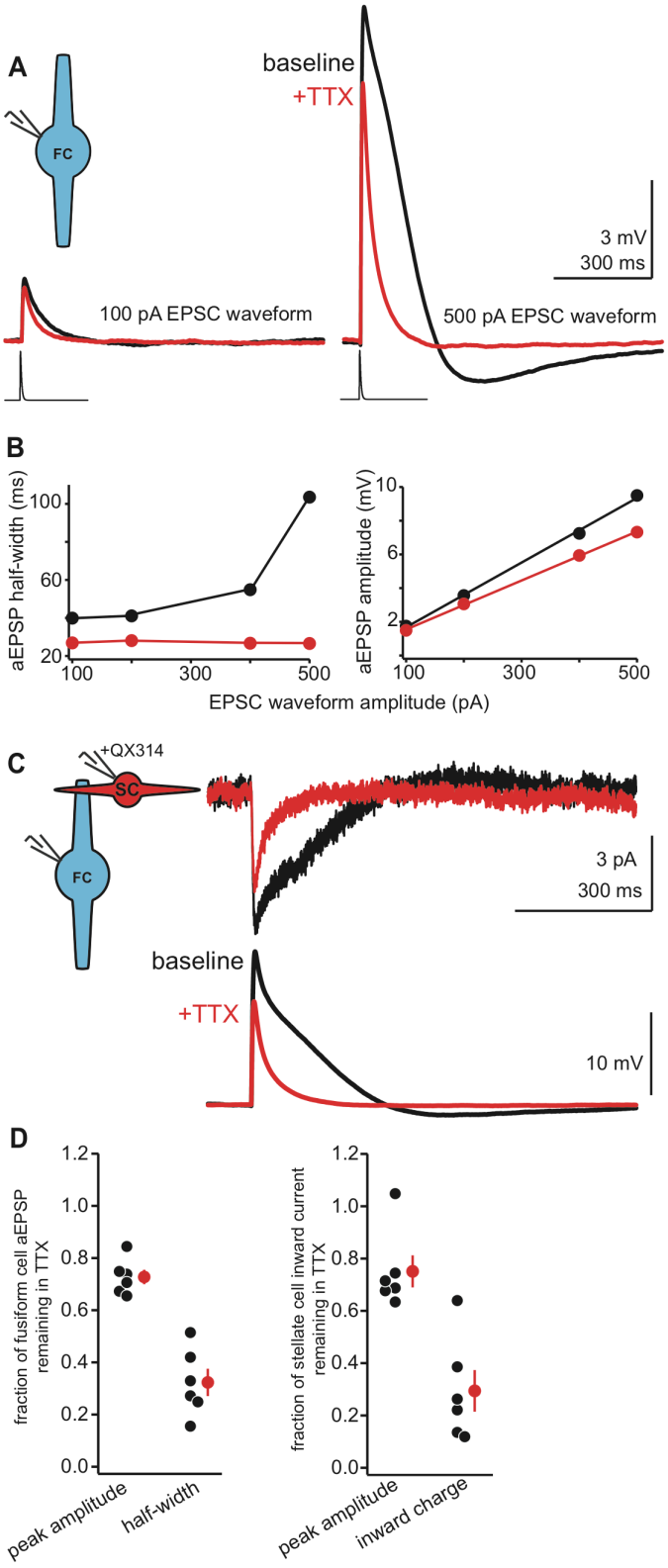
A
FC
baseline
+TTX
3 mV
300 ms
100 pA EPSC waveform
500 pA EPSC waveform
B
aEPSP half-width (ms)
100
60
20
100
300
500
aEPSP amplitude (mV)
10
6
2
100
300
500
EPSC waveform amplitude (pA)
C
+QX314
SC
FC
3 pA
300 ms
baseline
+TTX
10 mV
D
fraction of fusiform cell aEPSP remaining in TTX
1.2
1.0
0.8
0.6
0.4
0.2
0.0
peak amplitude
half-width
fraction of stellate cell inward current remaining in TTX
1.2
1.0
0.8
0.6
0.4
0.2
0.0
peak amplitude
inward charge

Figure 4.2: Subthreshold activation of Na^+ channels in fusiform cells shapes excitatory transmission in electrically-coupled interneurons.

A) Example traces from a fusiform cell recorded in current-clamp. An EPSC waveform is injected at two different amplitudes (100 and 500 pA) before and after bath application of TTX (black and red traces, respectively). The differential kinetics of the black traces highlights the role of Na^+ channels in shaping the aEPSP half-width. TTX application reduced the aEPSP half-width and peak amplitude, showing that subthreshold depolarizations activate Na^+ channels. Of note is the noticeable AHP following the aEPSP evoked with a 500 pA waveform. This AHP was reduced to 39±8% of baseline by TTX (n=7 cells), and is likely due to an effect of TTX on the aEPSP half-width: In n=3 cells tested, increasing the decay time of the EPSC command waveform from 3 to 10 ms following TTX application rescued the original AHP amplitude (baseline amplitude with 3 ms decay: -1.4±0.3 mV, in TTX with 3 ms decay: -0.8±0.2 mV, in TTX with 10 ms decay: -1.6±0.3 mV).

B) Example input/output curves for the recording in panel (A). Left Panel: aEPSP half-widths as a function of EPSC waveform amplitude before and after TTX (black and red points, respectively). TTX abrogated the amplitude dependence of aEPSP half-width. In n=7 cells, aEPSP half-widths evoked with the largest EPSC waveform amplitude (mean: 471±58 pA, range: 250-700 pA) were on average 2.4±0.4 times larger than aEPSP half-widths evoked with the smallest amplitude waveform (mean: 114±24 pA, range: 50-200 pA). This ratio was reduced to 1.0±0.1 in TTX ($p=0.007$, paired t-test), showing that Na^+ channels powerfully control the kinetics of subthreshold events. Right panel: aEPSP peak amplitudes are plotted as a function of EPSC command waveform in baseline and after

TTX. Color scheme is the same as left panel. The lines are linear fits to the data points to calculate the slope of the input/output function. On average, TTX reduced the slope of the aEPSP peak amplitude function to 77±3% of baseline (baseline: 0.027±0.004 mV/pA, TTX: 0.020±0.003 mV/pA, n=7, p=0.007, paired t-test).

C) Left: diagram of paired recording experiment. Na^+ channels are blocked specifically in the stellate cell by adding QX314 to the stellate cell pipette internal solution. Right: Average traces showing a subthreshold aEPSP in a fusiform cell (lower panel) and the resulting inward current in the stellate cell (upper panel) before and after TTX (black and red traces, respectively). TTX significantly reduced the amplitude and half-width of aEPSPs in the fusiform cell, as expected from the data (A). Additionally, TTX caused a major reduction in the amplitude and charge transfer of the gap junction-mediated inward current in the stellate cell, showing that subthreshold Na^+ currents in fusiform cells are a significant source of excitation for electrically-coupled interneurons.

D) Summary data from 6 pairs similar to panel C. Left panel: TTX reduced the amplitude and half-width of fusiform cell aEPSPs to 73±3% and 32±5% of baseline (p=0.0002 and p<0.0001, respectively, one sample t-test). Right panel: TTX also significantly reduced the amplitude and inward charge transfer of postjunctional currents in stellate cells to 75±6% and 29±8% of baseline (p=0.0097 and p=0.0003, respectively, one sample t-test).

Figure 4.3

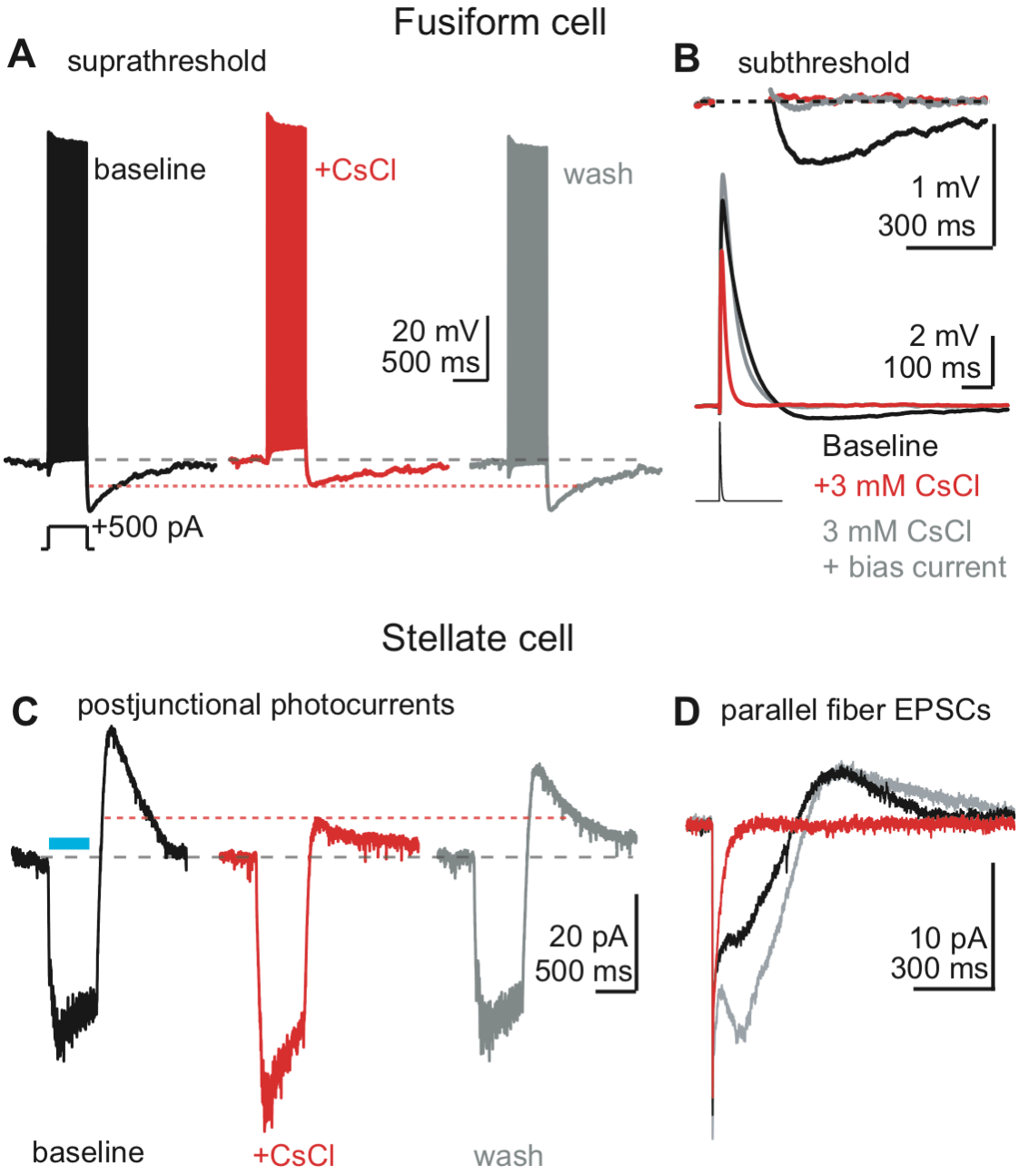
Fusiform cell
A
suprathreshold
baseline
+CsCl
wash
20 mV
500 ms
+500 pA
B
subthreshold
1 mV
300 ms
2 mV
100 ms
Baseline
+3 mM CsCl
3 mM CsCl
+ bias current
Stellate cell
C
postjunctional photocurrents
20 pA
500 ms
baseline
+CsCl
wash
D
parallel fiber EPSCs
10 pA
300 ms

Figure 4.3: Fusiform cell AHPs and stellate cell off-responses are mediated by deactivation of HCN channels.

A) A fusiform cell recorded in current clamp is driven to spike with positive current injection. Bath application of CsCl (3 mM, middle red panel) significantly reduced the amplitude of the AHP to 54±5% of baseline (n=6. p=0.0002, one sample t-test), and the AHP returned to 92±4% of baseline upon CsCl washout.

B) An EPSC-like command waveform (500 pA, lower trace) is injected in a fusiform cell recorded in current clamp. CsCl (red trace) hyperpolarized the cell (see main text), significantly shortened the half-width and reduced the peak amplitude of aEPSPs. These effects were largely reversed when the cell's membrane potential was returned to near baseline values with positive current injection (gray trace), showing that HCN channels control EPSP kinetics by setting the resting membrane potential near the activation range for subthreshold Na^+ currents (n=7 cells. Peak amplitude baseline: 7.8±0.6 mV; CsCl 6.0±0.5 mV; CsCl + bias current: 8.8±0.6 mV. p=0.0007 and p=0.13 comparing baseline to CsCl and CsCl + Bias conditions, respectively. Repeated measures ANOVA + Dunnett's test. Half-width baseline: 47±6 ms; CsCl: 15±1 ms; CsCl + bias: 36±3 ms; Baseline vs. CsCl: p=0.002 and p=0.076 comparing baseline to CsCl and CsCl+Bias, respectively. Repeated measures ANOVA + Dunnett's test). Blocking HCN channels also reduced the AHP following the depolarizing phase of the aEPSP, but adding bias current failed to recover the inhibitory off-response following the aEPSP (baseline: -0.39±0.08 mV; CsCl: -0.05 ±0.02 mV; CsCl + Bias current -0.03±0.01 mV, p= 0.014 and p=0.001 comparing baseline to CsCl and CsCl + Bias, respectively. Repeated measures ANOVA

+ Dunnett's test). Thus, the inhibitory off-response is mediated by cell-autonomous deactivation of HCN channels following an EPSP.

C) Example from a voltage-clamped stellate cell in a VGluT2-ChR2 mouse. Prejunctional fusiform cells are driven to spike with blue light flashes (blue bar), thereby generating a biphasic postjunctional response. The outward component of the photoresponse, which represents the fusiform cell membrane potential returning towards baseline during the AHP, was reversibly reduced by CsCl to 40±12% of baseline (n=7, $p<0.0001$. One sample t-test).

D) A stellate cell is recorded in voltage clamp. Parallel fibers are stimulated with a single shock, generating the biphasic E/I sequence shown in Figure 1B. CsCl significantly reduced the slow outward current to 1±2% of baseline (n=8. $p<0.0001$, one-sample t-test). Additionally CsCl hastened the timecourse of the inward component, quantified as a reduction of the EPSC inward charge transfer (n=8. 26±3% of baseline remaining, $p=0.01$, one sample t-test).

Figure 4.4

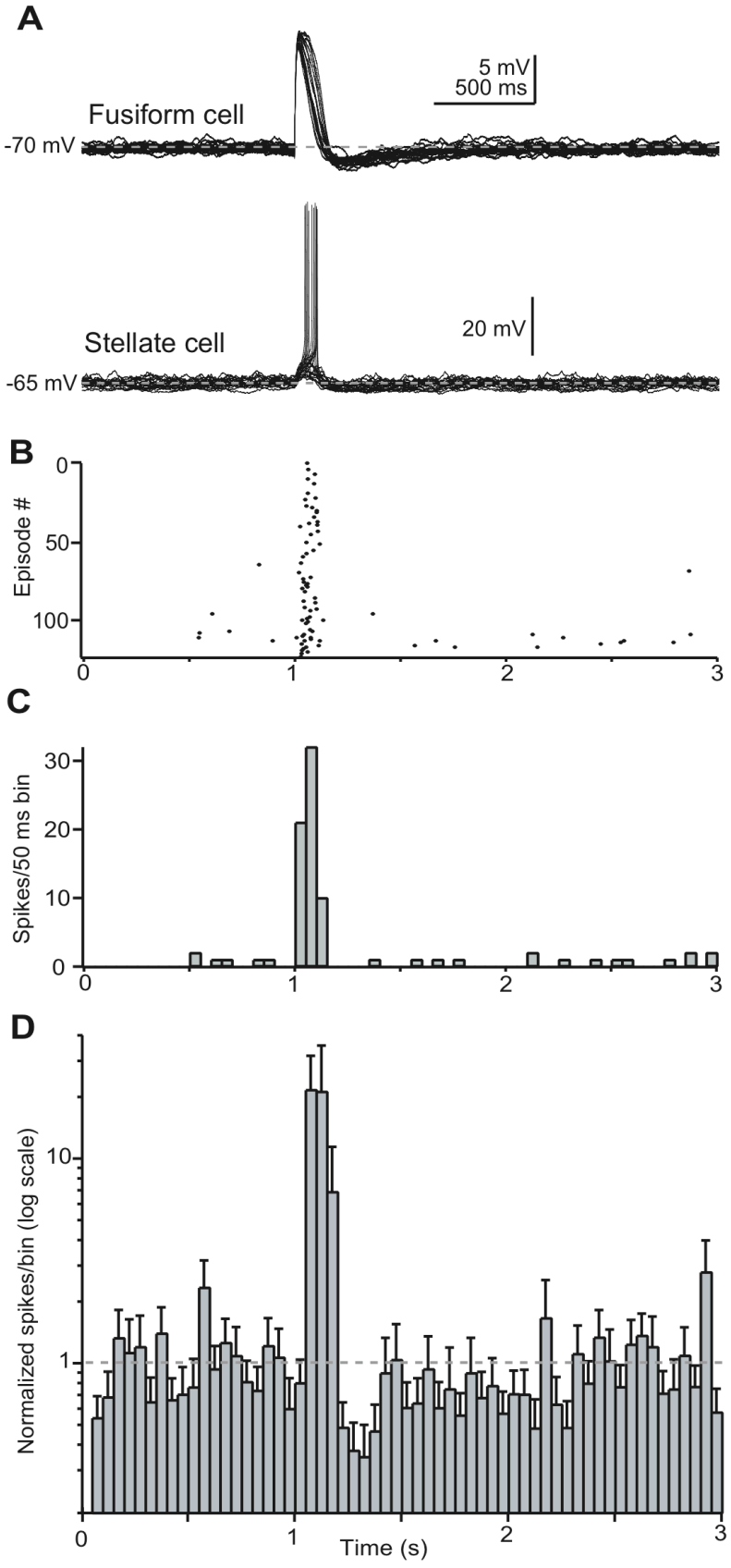
A
5 mV
500 ms
Fusiform cell
-70 mV
20 mV
Stellate cell
-65 mV
B
Episode #
0
50
100
0
1
2
3
C
Spikes/50 ms bin
30
20
10
0
0
1
2
3
D
Normalized spikes/bin (log scale)
10
1
0
1
2
3
Time (s)

Figure 4.4: Subthreshold events in fusiform cells drive spikes in stellate cells.

A) Example recording (20 single trials) from a coupled fusiform-stellate cell pair (upper and lower panels, respectively). A subthreshold aEPSP is produced with an EPSC waveform in the fusiform cell at ΔT=1 s (peak amplitude: 350 pA). Of note is the clustering of spikes in the stellate cell specifically during the prejunctional aEPSP.

B) Raster plot showing 123 trials from the pair in A, highlighting that subthreshold events in fusiform cell aEPSPs cause time-locked spikes in the stellate cell.

C) Histogram (50 ms bins) from the same pair as panels A and B.

D) Summary histogram (50 ms bins) from 7 pairs similar to A-C. The data are normalized to the number of spikes/bin during the 1 s prior to EPSC injection in the fusiform cell. Subthreshold events in fusiform cells caused a 21±12 fold increase in the number of stellate cell spikes/bin at ΔT=1.05-1.1 s, followed by a non-significant reduction in spike count at ΔT=1.2-1.4 s (baseline: 7.4±3.9 spikes/bin; ΔT=1.05-1.1 s: 34.9±9.0 spikes/bin; ΔT=1.2-1.4 s: 0.5±0.1 spikes/bin, p=0.01 and 0.2 compared to baseline, respectively. One-way repeated measures ANOVA + Dunnett's test). Of note is that the y-axis is plotted on a logarithmic scale.

SUMMARY AND CONCLUSIONS

By combining patch-clamp electrophysiology, 2-photon imaging, transgenic manipulations, and optogenetics, the experiments in Chapters 1-4 tested hypotheses regarding the molecular and circuit-level mechanisms that control synaptic inhibition at the early stages of central auditory processing.

Chapter 1 employed paired recordings between synaptically coupled pairs of glycine/GABA co-releasing cartwheel cells. I tested whether synaptic vesicles in intact neurons retained their contents once filled, or if synaptic vesicles "leaked" neurotransmitter. The data support a model whereby inhibitory synaptic vesicles require constant refilling in absence of release. Furthermore, these experiments provide the first quantitative estimate of cytosolic neurotransmitter concentrations at an inhibitory nerve terminal. This has important consequences for our understanding of inhibitory synaptic strength. Foremost, the basal concentration of cytosolic transmitter available for uptake into release-ready vesicles does not saturate vesicular transporters, implying that up- or down-regulation of cytosolic transmitter availability will potently control inhibitory synaptic strength. In agreement, instantaneously increasing GABA synthesis by uncaging glutamate inside presynaptic cells caused a rapid and potent increase in synaptic strength lasting several minutes. Given that the molecular mechanisms supplying glycine and GABA to inhibitory nerve terminals are subject to regulation by synaptic activity and neuromodulators (Wei and Wu, 2008; Jiménez et al., 2011), cytosolic transmitter availability may be regulated on a minutes time scale in the intact brain. However, further studies are required to determine the extent to which endogenous mechanisms such as

neuromodulators can regulate cytosolic transmitter availability, and thus exert a presynaptic control over inhibitory synaptic strength.

Chapter 2 focused on the chemical synaptic inputs to a previously uncharacterized DCN interneuron, the superficial stellate cell. Given the DCN's homology to the cerebellum and cerebellum-like circuits (Oertel and Young, 2004; Bell et al., 2008; Requarth and Sawtell, 2011), DCN stellate cells were hypothesized to play a similar role as the GABAergic stellate/basket cells of the cerebellar cortex (Wouterlood et al., 1984; Mugnaini, 1985). Indeed, previous *in vivo* studies suggested that GABAergic inhibition controls the response properties of excitatory fusiform cells and the inhibitory Purkinje-like cartwheel cells (Davis and Young, 2000), suggesting that the role of stellate cells in auditory processing potentially involves a disinhibitory function via stellate->cartwheel cell inhibition. Furthermore, a recent study suggested that GABAergic inhibition controls the spread of parallel fiber activity through the DCN (Middleton et al., 2011). This GABAergic inhibition is compromised in mice that show behavioral signs of tinnitus, suggesting that pathological downregulation of GABAergic inhibition in the DCN may partially underlie tinnitus percepts. Understanding how sensory inputs to the DCN drive stellate cell activity may provide insight as to the pathology of tinnitus and other hearing disorders. Thus, I set out to investigate the synaptic inputs to DCN stellate cells, and compare them with known features of cerebellar stellate cells.

Prior to these experiments, there had been only two published recordings from DCN stellate cells in slices (Zhang and Oertel, 1993; Golding and Oertel, 1997). This is likely due to their small size, which makes it difficult to record extracellularly during *in vivo* experiments. Moreover, the location of stellate cells at the ependymal edge of the

brainstem provides difficult access for whole-cell patch clamping, particularly for paired recordings. With practice, I managed to routinely record from sub-ependymal stellate cells and examine their properties. Similar to results from cerebellar stellate cells, I find that parallel fiber synapses onto DCN stellate cells have Ca^{2+}-permeable AMPA receptors with sub-millisecond decay kinetics. However, single parallel fibers also activated NMDA receptors, which contrasts with several reports from the stellate cells of the cerebellum (Glitsch and Marty, 1999; Carter and Regehr, 2000; Clark and Cull-Candy, 2002; Nahir and Jahr, 2013). Another major divergence from the cerebellum is that DCN stellate cells co-released glycine and GABA. This result was surprising and contrasts with previously held assumptions regarding the transmitter phenotype of DCN interneurons (Mugnaini, 1985; Doiron et al., 2011). Future studies are required to better understand how the different time courses and voltage-dependences of AMPA and NMDA receptors control stellate cell firing during sensory experience in intact animals. Furthermore, the functional implication of glycine/GABA co-release from stellate cells is unclear. Does co-release enable target-dependent kinetics of inhibitory transmission, as previously reported for Golgi cells of the cerebellum (Dugué et al., 2005)? Or perhaps co-release fine tunes the decay kinetics of postsynaptic glycine receptors (Lu et al., 2008)? Given that glycine is a co-agonist at NMDA receptors (Johnson and Ascher, 1987), another intriguing possibility is that glycine co-released from stellate cells might enhance NMDA receptor activity on neighboring neurons, thereby controlling the threshold for inducing synaptic plasticity at parallel fiber synapses.

While performing the experiments in Chapter 2, I found that stellate cells were electrically coupled to fusiform cells. This was surprising, as electrical coupling in the

brain is typically observed between GABAergic interneurons belonging to the same functional and anatomical family (Hestrin and Galarreta, 2005). Furthermore, heterologous coupling between principal cells and interneurons was not predicted by previous anatomy studies, and thus represents a significant revision of the canonical DCN circuit. The experiments in Chapter 3 characterized this electrical network and examined the functional implications of this novel circuit motif. Electrical coupling was >4-fold stronger in the fusiform to stellate direction than vice versa, thereby preferentially allowing fusiform cells to control the stellate cell membrane potential. This is likely due to the fact that the stellate cell membrane resistance is ~10-fold greater than that of fusiform cells. Furthermore, the data show that stellate cells are electrically coupled to multiple prejunctional fusiform cells, but activity in even a single fusiform cell is sufficient to alter the firing pattern of stellate cells. Perhaps the most surprising result was that activating fusiform cells sufficed to generate robust inhibition in neighboring neurons by driving the stellate cell network. This "surround inhibition" was entirely mediated by gap junction coupling, as it persisted in the presence of drugs that block excitatory glutamatergic transmission.

Although these experiments revise our understanding of the DCN microcircuit, further studies will be required to elucidate the functional connectivity in the DCN "electrome". For example, do stellate cells receive electrical inputs from isofrequency fusiform cells, or from fusiform cells that respond to different frequencies? This will likely be an important determinant of stellate cell response characteristics in an awake, behaving animal. Furthermore, it is unclear whether the weak homologous electrical coupling reported in pairs of stellate cells occurs between stellate cells that receive common or

divergent electrical inputs from fusiform cells. These experiments will require major studies using cutting-edge functional anatomy and imaging techniques.

An interesting consequence of electrical coupling is that sub-threshold activity as well as action potentials can propagate through electrical networks. Furthermore, gap junctions allow for excitatory and inhibitory signals to transmit from one neuron to the next, permitting a bidirectional control of neighboring neurons. The experiments in Chapter 4 tested whether sub-threshold synaptic activity onto fusiform cells generates signals in stellate cells through gap junction coupling. In agreement, I find that even mild stimulation to parallel fibers (e.g., single shocks) generates a slow excitatory/inhibitory response sequence in stellate cells that is mediated by ion channel activity in fusiform cells. This occurs because fusiform cell EPSPs are shaped by subthreshold activation of a persistent Na^+ current and HCN channel deactivation. Subthreshold activation of the fusiform cell Na^+ current generated slow excitation in stellate cells. However, EPSPs in fusiform cells were followed by a transient hyperpolarization that was due to the deactivation of the resting I_h conductance during the EPSP; this hyperpolarization causes an inhibitory postjunctional current in electrically-coupled stellate cells. Thus, excitatory transmission in fusiform cells generates both cell-autonomous and network-wide excitatory/inhibitory sequences through gap junction coupling.

Given that fusiform cells receive a much larger total number of parallel fibers than stellate cells, I suggest that gap junction-mediated transmission in stellate cells accounts for the majority of the excitatory drive to these neurons during *in vivo* activity. A direct test of this hypothesis will however require recording from stellate cells in awake, behaving animals. If this model is correct, stellate cells recorded from mice lacking gap

junction coupling in the DCN (connexin36 knockout mice) should show far less excitatory drive than wild-type littermates during sensory stimulation.

While these experiments were performed in the auditory brainstem, the mechanisms involved in packaging and release of inhibitory neurotransmitters are remarkably similar across different brain areas (Edwards, 2007). Furthermore, the biophysical mechanisms that control the activity of DCN stellate cells, e.g., electrical coupling, Ca^{2+}-permeable AMPA receptors, and subthreshold Na^{+} channel activation, are common features found in diverse cell types (Bennett and Zukin, 2004; Isaac et al., 2007; Yamada-Hanff and Bean, 2013). It is my hope that the experiments from this thesis shed light upon certain general principles that govern how inhibitory neurons function to control the output of neuronal microcircuits.

REFERENCES

Agoston DV, Kosh JW, Lisziewicz J, Whittaker VP (1985) Separation of recycling and reserve synaptic vesicles from cholinergic nerve terminals of the myenteric plexus of guinea pig ileum. Journal of Neurochemistry 44:299–305.

Alvarez VA, Chow CC, Van Bockstaele EJ, Williams JT (2002) Frequency-dependent synchrony in locus ceruleus: role of electrotonic coupling. Proc Natl Acad Sci USA 99:4032–4036.

Andersen P, Eccles JC, Loyning Y (1963) Recurrent inhibition in the hippocampus with identification of the inhibitory cell and its synapses. Nature 198:540–542.

Apostolides PF, Trussell LO (2013a) Rapid, Activity-Independent Turnover of Vesicular Transmitter Content at a Mixed Glycine/GABA Synapse. J Neurosci 33:4768–4781.

Apostolides PF, Trussell LO (2013b) Regulation of interneuron excitability by gap junction coupling with principal cells. Nat Neurosci.

Arenkiel BR, Peca J, Davison IG, Feliciano C, Deisseroth K, Augustine GJ, Ehlers MD, Feng G (2007) In vivo light-induced activation of neural circuitry in transgenic mice expressing channelrhodopsin-2. Neuron 54:205–218.

Awatramani GB, Turecek R, Trussell LO (2005) Staggered development of GABAergic and glycinergic transmission in the MNTB. J Neurophysiol 93:819–828.

Axmacher N, Stemmler M, Engel D, Draguhn A, Ritz R (2004) Transmitter metabolism as a mechanism of synaptic plasticity: a modeling study. J Neurophysiol 91:25–39.

Bagley EE, Hacker J, Chefer VI, Mallet C, McNally GP, Chieng BCH, Perroud J, Shippenberg TS, Christie MJ (2011) Drug-induced GABA transporter currents enhance GABA release to induce opioid withdrawal behaviors. Nat Neurosci 14:1548–1554.

Bal T, McCormick DA (1997) Synchronized oscillations in the inferior olive are controlled by the hyperpolarization-activated cation current I(h). J Neurophysiol 77:3145–3156.

Balu R, Larimer P, Strowbridge BW (2004) Phasic stimuli evoke precisely timed spikes in intermittently discharging mitral cells. J Neurophysiol 92:743–753.

Barbuti A, DiFrancesco D (2008) Control of cardiac rate by “funny” channels in health and disease. Ann N Y Acad Sci 1123:213–223.

Barmack NH, Yakhnitsa V (2008) Functions of interneurons in mouse cerebellum. J Neurosci 28:1140–1152.

Beato M (2008) The time course of transmitter at glycinergic synapses onto

motoneurons. J Neurosci 28:7412–7425.

Beato M, Burzomato V, Sivilotti LG (2007) The kinetics of inhibition of rat recombinant heteromeric alpha1beta glycine receptors by the low-affinity antagonist SR-95531. J Physiol (Lond) 580:171–179.

Bell CC, Caputi A, Grant K (1997a) Physiology and plasticity of morphologically identified cells in the mormyrid electrosensory lobe. J Neurosci 17:6409–6423.

Bell CC, Han V, Sawtell NB (2008) Cerebellum-like structures and their implications for cerebellar function. Annu Rev Neurosci 31:1–24.

Bell CC, Han VZ, Sugawara Y, Grant K (1997b) Synaptic plasticity in a cerebellum-like structure depends on temporal order. Nature 387:278–281.

Bell MR, Belarde JA, Johnson HF, Aizenman CD (2011) A neuroprotective role for polyamines in a Xenopus tadpole model of epilepsy. Nat Neurosci 14:505–512.

Bender KJ, Ford CP, Trussell LO (2010) Dopaminergic modulation of axon initial segment calcium channels regulates action potential initiation. Neuron 68:500–511.

Bender KJ, Trussell LO (2009) Axon initial segment Ca2+ channels influence action potential generation and timing. Neuron 61:259–271.

Bennett MV (1966) Physiology of electrotonic junctions. Ann N Y Acad Sci 137:509–539.

Bennett MVL, Zukin RS (2004) Electrical coupling and neuronal synchronization in the Mammalian brain. Neuron 41:495–511.

Berliner KI, Shelton C, Hitselberger WE, Luxford WM (1992) Acoustic tumors: effect of surgical removal on tinnitus. Am J Otol 13:13–17.

Bittner KC, Andrasfalvy BK, Magee JC (2012) Ion channel gradients in the apical tuft region of CA1 pyramidal neurons. PLoS ONE 7:e46652.

Bradaïa A, Schlichter R, Trouslard J (2004) Role of glial and neuronal glycine transporters in the control of glycinergic and glutamatergic synaptic transmission in lamina X of the rat spinal cord. J Physiol (Lond) 559:169–186.

Brozoski TJ, Bauer CA, Caspary DM (2002) Elevated fusiform cell activity in the dorsal cochlear nucleus of chinchillas with psychophysical evidence of tinnitus. J Neurosci 22:2383–2390.

Burger PM, Hell J, Mehl E, Krasel C, Lottspeich F, Jahn R (1991) GABA and glycine in synaptic vesicles: storage and transport characteristics. Neuron 7:287–293.

Cabeza R, Collier B (1988) Acetylcholine mobilization in a sympathetic ganglion in the

presence and absence of 2-(4-phenylpiperidino)cyclohexanol (AH5183). Journal of Neurochemistry 50:112–121.

Callaway JC, Lasser-Ross N, Ross WN (1995) IPSPs strongly inhibit climbing fiber-activated [Ca2+]i increases in the dendrites of cerebellar Purkinje neurons. J Neurosci 15:2777–2787.

Carter AG, Regehr WG (2000) Prolonged synaptic currents and glutamate spillover at the parallel fiber to stellate cell synapse. J Neurosci 20:4423–4434.

Carter AG, Regehr WG (2002) Quantal events shape cerebellar interneuron firing. Nat Neurosci 5:1309–1318.

Carter BC, Giessel AJ, Sabatini BL, Bean BP (2012) Transient sodium current at subthreshold voltages: activation by EPSP waveforms. Neuron 75:1081–1093.

Chang Y, Xie Y, Weiss DS (2001) Positive allosteric modulation by ultraviolet irradiation on GABA(A), but not GABA(C), receptors expressed in Xenopus oocytes. J Physiol (Lond) 536:471–478.

Cherian K, Cherian N, Cook C, Kaltenbach JA (2013) Improving tinnitus with mechanical treatment of the cervical spine and jaw. J Am Acad Audiol 24:544–555.

Chéry N, de Koninck Y (1999) Junctional versus extrajunctional glycine and GABA(A) receptor-mediated IPSCs in identified lamina I neurons of the adult rat spinal cord. J Neurosci 19:7342–7355.

Christensen H, Fykse EM, Fonnum F (1990) Uptake of glycine into synaptic vesicles isolated from rat spinal cord. Journal of Neurochemistry 54:1142–1147.

Christie MJ, Williams JT, North RA (1989) Electrical coupling synchronizes subthreshold activity in locus coeruleus neurons in vitro from neonatal rats. J Neurosci 9:3584–3589.

Clark BA, Cull-Candy SG (2002) Activity-dependent recruitment of extrasynaptic NMDA receptor activation at an AMPA receptor-only synapse. J Neurosci 22:4428–4436.

Coddington LT, Rudolph S, Vande Lune P, Overstreet-Wadiche L, Wadiche JI (2013) Spillover-mediated feedforward inhibition functionally segregates interneuron activity. Neuron 78:1050–1062.

Crowley JJ, Carter AG, Regehr WG (2007) Fast vesicle replenishment and rapid recovery from desensitization at a single synaptic release site. J Neurosci 27:5448–5460.

Davis KA, Miller RL, Young ED (1996) Effects of somatosensory and parallel-fiber stimulation on neurons in dorsal cochlear nucleus. J Neurophysiol 76:3012–3024.

Davis KA, Young ED (1997) Granule cell activation of complex-spiking neurons in dorsal cochlear nucleus. J Neurosci 17:6798–6806.

Davis KA, Young ED (2000) Pharmacological evidence of inhibitory and disinhibitory neuronal circuits in dorsal cochlear nucleus. J Neurophysiol 83:926–940.

de Oliveira RB, Howlett MCH, Gravina FS, Imtiaz MS, Callister RJ, Brichta AM, van Helden DF (2010) Pacemaker currents in mouse locus coeruleus neurons. Neuroscience 170:166–177.

Dean P, Porrill J, Ekerot C-F, Jörntell H (2010) The cerebellar microcircuit as an adaptive filter: experimental and computational evidence. Nat Rev Neurosci 11:30–43.

Dericioglu N, Garganta CL, Petroff OA, Mendelsohn D, Williamson A (2008) Blockade of GABA synthesis only affects neural excitability under activated conditions in rat hippocampal slices. Neurochem Int 53:22–32.

Devor A, Yarom Y (2002) Electrotonic coupling in the inferior olivary nucleus revealed by simultaneous double patch recordings. J Neurophysiol 87:3048–3058.

Diana MA, Marty A (2003) Characterization of depolarization-induced suppression of inhibition using paired interneuron--Purkinje cell recordings. J Neurosci 23:5906–5918.

Doiron B, Zhao Y, Tzounopoulos T (2011) Combined LTP and LTD of modulatory inputs controls neuronal processing of primary sensory inputs. J Neurosci 31:10579–10592.

Dugué GP, Brunel N, Hakim V, Schwartz E, Chat M, Lévesque M, Courtemanche R, Léna C, Dieudonné S (2009) Electrical coupling mediates tunable low-frequency oscillations and resonance in the cerebellar Golgi cell network. Neuron 61:126–139.

Dugué GP, Dumoulin A, Triller A, Dieudonné S (2005) Target-dependent use of co-released inhibitory transmitters at central synapses. J Neurosci 25:6490–6498.

Edwards RH (2007) The neurotransmitter cycle and quantal size. Neuron 55:835–858.

Engel D, Pahner I, Schulze K, Frahm C, Jarry H, Ahnert-Hilger G, Draguhn A (2001) Plasticity of rat central inhibitory synapses through GABA metabolism. J Physiol (Lond) 535:473–482.

Efron B, Tibshirani R (1986) Bootstrap methods for standard errors, confidence intervals, and other measures of statistical accuracy. Statistical Science 1:54-77.

Floor E, Leventhal PS, Wang Y, Meng L, Chen W (1995) Dynamic storage of dopamine in rat brain synaptic vesicles in vitro. Journal of Neurochemistry 64:689–699.

Fonnum F, Walberg F (1973) The concentration of GABA within inhibitory nerve terminals. Brain Res 62:577–579.

Fornés A, Núñez E, Alonso-Torres P, Aragón C, López-Corcuera B (2008) Trafficking properties and activity regulation of the neuronal glycine transporter GLYT2 by protein kinase C. Biochem J 412:495–506.

Gardner SM, Trussell LO, Oertel D (1999) Time course and permeation of synaptic AMPA receptors in cochlear nuclear neurons correlate with input. J Neurosci 19:8721–8729.

Gardner SM, Trussell LO, Oertel D (2001) Correlation of AMPA receptor subunit composition with synaptic input in the mammalian cochlear nuclei. J Neurosci 21:7428–7437.

Geerlings A, Núñez E, López-Corcuera B, Aragón C (2001) Calcium- and syntaxin 1-mediated trafficking of the neuronal glycine transporter GLYT2. J Biol Chem 276:17584–17590.

Gibson JR, Beierlein M, Connors BW (1999) Two networks of electrically coupled inhibitory neurons in neocortex. Nature 402:75–79.

Gibson JR, Beierlein M, Connors BW (2005) Functional properties of electrical synapses between inhibitory interneurons of neocortical layer 4. J Neurophysiol 93:467–480.

Gillespie PG, Müller U (2009) Mechanotransduction by hair cells: models, molecules, and mechanisms. Cell 139:33–44.

Glitsch M, Marty A (1999) Presynaptic effects of NMDA in cerebellar Purkinje cells and interneurons. J Neurosci 19:511–519.

Glowatzki E, Grant L, Fuchs P (2008) Hair cell afferent synapses. Curr Opin Neurobiol 18:389–395.

Golding NL, Oertel D (1997) Physiological identification of the targets of cartwheel cells in the dorsal cochlear nucleus. J Neurophysiol 78:248–260.

Gomeza J, Ohno K, Hülsmann S, Armsen W, Eulenburg V, Richter DW, Laube B, Betz H (2003) Deletion of the mouse glycine transporter 2 results in a hyperekplexia phenotype and postnatal lethality. Neuron 40:797–806.

Han VZ, Grant K, Bell CC (2000) Reversible associative depression and nonassociative potentiation at a parallel fiber synapse. Neuron 27:611–622.

Hancock KE, Voigt HF (2002) Intracellularly labeled fusiform cells in dorsal cochlear nucleus of the gerbil. I. Physiological response properties. J Neurophysiol 87:2505–2519.

Hansel C, de Jeu M, Belmeguenai A, Houtman SH, Buitendijk GHS, Andreev D, De Zeeuw CI, Elgersma Y (2006) alphaCaMKII Is essential for cerebellar LTD and motor learning. Neuron 51:835–843.

Harnett MT, Xu N-L, Magee JC, Williams SR (2013) Potassium channels control the interaction between active dendritic integration compartments in layer 5 cortical pyramidal neurons. Neuron 79:516–529.

Hägglund M, Borgius L, Dougherty KJ, Kiehn O (2010) Activation of groups of excitatory neurons in the mammalian spinal cord or hindbrain evokes locomotion. Nat Neurosci 13:246–252.

Hebrank J, Wright D (1974) Spectral cues used in the localization of sound sources on the median plane. J Acoust Soc Am 56:1829–1834.

Hestrin S, Galarreta M (2005) Electrical synapses define networks of neocortical GABAergic neurons. Trends Neurosci 28:304–309.

Hoffman DA, Magee JC, Colbert CM, Johnston D (1997) K+ channel regulation of signal propagation in dendrites of hippocampal pyramidal neurons. Nature 387:869–875.

Hori T, Takahashi T (2012) Kinetics of synaptic vesicle refilling with neurotransmitter glutamate. Neuron 76:511–517.

Hughes DI, Mackie M, Nagy GG, Riddell JS, Maxwell DJ, Szabó G, Erdélyi F, Veress G, Szucs P, Antal M, Todd AJ (2005) P boutons in lamina IX of the rodent spinal cord express high levels of glutamic acid decarboxylase-65 and originate from cells in deep medial dorsal horn. Proc Natl Acad Sci USA 102:9038–9043.

Isaac JTR, Ashby MC, McBain CJ (2007) The role of the GluR2 subunit in AMPA receptor function and synaptic plasticity. Neuron 54:859–871.

Isaacson JS, Scanziani M (2011) How inhibition shapes cortical activity. Neuron 72:231–243.

Ishikawa T, Sahara Y, Takahashi T (2002) A single packet of transmitter does not saturate postsynaptic glutamate receptors. Neuron 34:613–621.

Isope P, Franconville R, Barbour B, Ascher P (2004) Repetitive firing of rat cerebellar parallel fibres after a single stimulation. J Physiol (Lond) 554:829–839.

Ito T, Oliver DL (2010) Origins of Glutamatergic Terminals in the Inferior Colliculus Identified by Retrograde Transport and Expression of VGLUT1 and VGLUT2 Genes. Front Neuroanat 4:135.

Jackson AC, Nicoll RA (2011) Stargazin (TARP gamma-2) is required for compartment-specific AMPA receptor trafficking and synaptic plasticity in cerebellar stellate cells.

J Neurosci 31:3939–3952.

Ji F, Kanbara N, Obata K (1999) GABA and histogenesis in fetal and neonatal mouse brain lacking both the isoforms of glutamic acid decarboxylase. Neurosci Res 33:187–194.

Jiménez E, Zafra F, Pérez-Sen R, Delicado EG, Miras-Portugal MT, Aragón C, López-Corcuera B (2011) P2Y purinergic regulation of the glycine neurotransmitter transporters. J Biol Chem 286:10712–10724.

Jin H, Wu H, Osterhaus G, Wei J, Davis K, Sha D, Floor E, Hsu C-C, Kopke RD, Wu J-Y (2003) Demonstration of functional coupling between gamma -aminobutyric acid (GABA) synthesis and vesicular GABA transport into synaptic vesicles. Proc Natl Acad Sci USA 100:4293–4298.

Johnson JW, Ascher P (1987) Glycine potentiates the NMDA response in cultured mouse brain neurons. Nature 325:529–531.

Jonas P, Bischofberger J, Sandkühler J (1998) Corelease of two fast neurotransmitters at a central synapse. Science 281:419–424.

Kaltenbach JA (2006a) The dorsal cochlear nucleus as a participant in the auditory, attentional and emotional components of tinnitus. Hear Res 216-217:224–234.

Kaltenbach JA (2006b) Summary of evidence pointing to a role of the dorsal cochlear nucleus in the etiology of tinnitus. Acta Otolaryngol Suppl:20–26.

Kamboj SK, Swanson GT, Cull-Candy SG (1995) Intracellular spermine confers rectification on rat calcium-permeable AMPA and kainate receptors. J Physiol (Lond) 486 (Pt 2):297–303.

Kanaani J, el-Husseini AE-D, Aguilera-Moreno A, Diacovo JM, Bredt DS, Baekkeskov S (2002) A combination of three distinct trafficking signals mediates axonal targeting and presynaptic clustering of GAD65. J Cell Biol 158:1229–1238.

Kandler K, Clause A, Noh J (2009) Tonotopic reorganization of developing auditory brainstem circuits. Nat Neurosci 12:711–717.

Kanold PO, Young ED (2001) Proprioceptive information from the pinna provides somatosensory input to cat dorsal cochlear nucleus. J Neurosci 21:7848–7858.

Kirmse K, Kirischuk S (2006) Ambient GABA constrains the strength of GABAergic synapses at Cajal-Retzius cells in the developing visual cortex. J Neurosci 26:4216–4227.

Koehler SD, Pradhan S, Manis PB, Shore SE (2011) Somatosensory inputs modify auditory spike timing in dorsal cochlear nucleus principal cells. Eur J Neurosci 33:409–420.

Kondo S, Marty A (1998) Synaptic currents at individual connections among stellate cells in rat cerebellar slices. J Physiol (Lond) 509 (Pt 1):221–232.

Kopp-Scheinpflug C, Tozer AJB, Robinson SW, Tempel BL, Hennig MH, Forsythe ID (2011) The sound of silence: ionic mechanisms encoding sound termination. Neuron 71:911–925.

Kuo SP, Trussell LO (2011) Spontaneous spiking and synaptic depression underlie noradrenergic control of feed-forward inhibition. Neuron 71:306–318.

L Palay S, Chan-Palay V (1974) Cerebellar cortex: cytology and organization‽ :348.

Lamsa KP, Heeroma JH, Somogyi P, Rusakov DA, Kullmann DM (2007) Anti-Hebbian long-term potentiation in the hippocampal feedback inhibitory circuit. Science 315:1262–1266.

Latal AT, Kremer T, Gomeza J, Eulenburg V, Hülsmann S (2010) Development of synaptic inhibition in glycine transporter 2 deficient mice. Mol Cell Neurosci 44:342–352.

Leao RM, Li S, Doiron B, Tzounopoulos T (2012) Diverse levels of an inwardly rectifying potassium conductance generate heterogeneous neuronal behavior in a population of dorsal cochlear nucleus pyramidal neurons. J Neurophysiol 107:3008–3019.

Liang S-L, Carlson GC, Coulter DA (2006) Dynamic regulation of synaptic GABA release by the glutamate-glutamine cycle in hippocampal area CA1. J Neurosci 26:8537–8548.

Liu SQ, Cull-Candy SG (2000) Synaptic activity at calcium-permeable AMPA receptors induces a switch in receptor subtype. Nature 405:454–458.

Losonczy A, Makara JK, Magee JC (2008) Compartmentalized dendritic plasticity and input feature storage in neurons. Nature 452:436–441.

Lu T, Rubio ME, Trussell LO (2008) Glycinergic transmission shaped by the corelease of GABA in a mammalian auditory synapse. Neuron 57:524–535.

Ma W-LD, Brenowitz SD (2012) Single-neuron recordings from unanesthetized mouse dorsal cochlear nucleus. J Neurophysiol 107:824–835.

Magee J (1999) Dendritic Ih normalizes temporal summation in hippocampal CA1 neurons. Nat Neurosci 2:848.

Maher BJ, McGinley MJ, Westbrook GL (2009) Experience-dependent maturation of the glomerular microcircuit. Proc Natl Acad Sci USA 106:16865–16870.

Mancilla JG, Manis PB (2009) Two distinct types of inhibition mediated by cartwheel

cells in the dorsal cochlear nucleus. J Neurophysiol 102:1287–1295.

Manis PB, Spirou GA, Wright DD, Paydar S, Ryugo DK (1994) Physiology and morphology of complex spiking neurons in the guinea pig dorsal cochlear nucleus. J Comp Neurol 348:261–276.

Mann-Metzer P, Yarom Y (1999) Electrotonic coupling interacts with intrinsic properties to generate synchronized activity in cerebellar networks of inhibitory interneurons. J Neurosci 19:3298–3306.

Mathews GC, Diamond JS (2003) Neuronal glutamate uptake Contributes to GABA synthesis and inhibitory synaptic strength. J Neurosci 23:2040–2048.

Mathews PJ, Lee KH, Peng Z, Houser CR, Otis TS (2012) Effects of climbing fiber driven inhibition on Purkinje neuron spiking. J Neurosci 32:17988–17997.

May BJ (2000) Role of the dorsal cochlear nucleus in the sound localization behavior of cats. Hear Res 148:74–87.

McIntire SL, Reimer RJ, Schuske K, Edwards RH, Jorgensen EM (1997) Identification and characterization of the vesicular GABA transporter. Nature 389:870–876.

Merchan MA, Collia FP, Merchan JA, Saldana E (1985) Distribution of primary afferent fibres in the cochlear nuclei. A silver and horseradish peroxidase (HRP) study. J Anat 141:121–130.

Middlebrooks JC (1992) Narrow-band sound localization related to external ear acoustics. J Acoust Soc Am 92:2607–2624.

Middleton JW, Kiritani T, Pedersen C, Turner JG, Shepherd GMG, Tzounopoulos T (2011) Mice with behavioral evidence of tinnitus exhibit dorsal cochlear nucleus hyperactivity because of decreased GABAergic inhibition. Proc Natl Acad Sci USA 108:7601–7606.

Mitchell SJ, Silver RA (2003) Shunting inhibition modulates neuronal gain during synaptic excitation. Neuron 38:433–445.

Molitor SC, Manis PB (2003) Dendritic Ca2+ transients evoked by action potentials in rat dorsal cochlear nucleus pyramidal and cartwheel neurons. J Neurophysiol 89:2225–2237.

Mosharov EV, Gong L-W, Khanna B, Sulzer D, Lindau M (2003) Intracellular patch electrochemistry: regulation of cytosolic catecholamines in chromaffin cells. J Neurosci 23:5835–5845.

Mugnaini E (1985) GABA neurons in the superficial layers of the rat dorsal cochlear nucleus: light and electron microscopic immunocytochemistry. J Comp Neurol 235:61–81.

Mugnaini E, Berrebi AS, Dahl AL, Morgan JI (1987) The polypeptide PEP-19 is a marker for Purkinje neurons in cerebellar cortex and cartwheel neurons in the dorsal cochlear nucleus. Arch Ital Biol 126:41–67.

Myoga MH, Beierlein M, Regehr WG (2009) Somatic spikes regulate dendritic signaling in small neurons in the absence of backpropagating action potentials. J Neurosci 29:7803–7814.

Nabekura J, Katsurabayashi S, Kakazu Y, Shibata S, Matsubara A, Jinno S, Mizoguchi Y, Sasaki A, Ishibashi H (2004) Developmental switch from GABA to glycine release in single central synaptic terminals. Nat Neurosci 7:17–23.

Nagel G, Szellas T, Huhn W, Kateriya S, Adeishvili N, Berthold P, Ollig D, Hegemann P, Bamberg E (2003) Channelrhodopsin-2, a directly light-gated cation-selective membrane channel. Proc Natl Acad Sci USA 100:13940–13945.

Nahir B, Jahr CE (2013) Activation of Extrasynaptic NMDARs at Individual Parallel Fiber-Molecular Layer Interneuron Synapses in Cerebellum. J Neurosci 33:16323–16333.

Obata K, Otsuka M, Tanaka Y (1970) Determination of gamma-aminobutyric acid in single nerve cells of cat central nervous system. Journal of Neurochemistry 17:697–698.

Oertel D, Young ED (2004) What's a cerebellar circuit doing in the auditory system? Trends Neurosci 27:104–110.

Oldfield CS, Marty A, Stell BM (2010) Interneurons of the cerebellar cortex toggle Purkinje cells between up and down states. Proc Natl Acad Sci USA 107:13153–13158.

Osen KK, Mugnaini E (1981) Neuronal circuits in the dorsal cochlear nucleus. Neuronal mechanisms of hearing.

Osen KK, Ottersen OP, Storm-Mathisen J (1990) Osen: Colocalization of glycine-like and GABA-like... - Google Scholar. Glycine neurotransmission.

Otis TS, Wu YC, Trussell LO (1996) Delayed clearance of transmitter and the role of glutamate transporters at synapses with multiple release sites. J Neurosci 16:1634–1644.

Otsuka M, Obata K, Miyata Y, Tanaka Y (1971) Measurement of gamma-aminobutyric acid in isolated nerve cells of cat central nervous system. Journal of Neurochemistry 18:287–295.

Parri HR, Crunelli V (1998) Sodium current in rat and cat thalamocortical neurons: role of a non-inactivating component in tonic and burst firing. J Neurosci 18:854–867.

Porter TG, Martin DL (1985) Chelidonic acid and other conformationally restricted substrate analogues as inhibitors of rat brain glutamate decarboxylase. Biochem Pharmacol 34:4145–4150.

Portfors CV, Roberts PD (2007) Temporal and frequency characteristics of cartwheel cells in the dorsal cochlear nucleus of the awake mouse. J Neurophysiol 98:744–756.

Potter LT (1970) Synthesis, storage and release of [14C]acetylcholine in isolated rat diaphragm muscles. J Physiol (Lond) 206:145–166.

Pouille F, Scanziani M (2001) Enforcement of temporal fidelity in pyramidal cells by somatic feed-forward inhibition. Science 293:1159–1163.

Pouzat C, Marty A (1998) Autaptic inhibitory currents recorded from interneurones in rat cerebellar slices. J Physiol (Lond) 509 (Pt 3):777–783.

Reiss LAJ, Young ED (2005) Spectral edge sensitivity in neural circuits of the dorsal cochlear nucleus. J Neurosci 25:3680–3691.

Requarth T, Sawtell NB (2011) Neural mechanisms for filtering self-generated sensory signals in cerebellum-like circuits. Curr Opin Neurobiol 21:602–608.

Rhode WS, Smith PH, Oertel D (1983) Physiological response properties of cells labeled intracellularly with horseradish peroxidase in cat dorsal cochlear nucleus. J Comp Neurol 213:426–447.

Roberts LE, Eggermont JJ, Caspary DM, Shore SE, Melcher JR, Kaltenbach JA (2010) Ringing ears: the neuroscience of tinnitus. J Neurosci 30:14972–14979.

Roberts MT, Bender KJ, Trussell LO (2008) Fidelity of complex spike-mediated synaptic transmission between inhibitory interneurons. J Neurosci 28:9440–9450.

Roberts MT, Trussell LO (2010) Molecular layer inhibitory interneurons provide feedforward and lateral inhibition in the dorsal cochlear nucleus. J Neurophysiol 104:2462–2473.

Rousseau F, Aubrey KR, Supplisson S (2008) The glycine transporter GlyT2 controls the dynamics of synaptic vesicle refilling in inhibitory spinal cord neurons. J Neurosci 28:9755–9768.

Rozov A, Burnashev N (1999) Polyamine-dependent facilitation of postsynaptic AMPA receptors counteracts paired-pulse depression. Nature 401:594–598.

Rubio ME, Juiz JM (2004) Differential distribution of synaptic endings containing glutamate, glycine, and GABA in the rat dorsal cochlear nucleus. J Comp Neurol 477:253–272.

Rusznák Z, Pál B, Kőszeghy A, Fu Y, Szücs G, Paxinos G (2013) The hyperpolarization-

activated non-specific cation current (In) adjusts the membrane properties, excitability, and activity pattern of the giant cells in the rat dorsal cochlear nucleus. Eur J Neurosci 37:876–890.

Sawtell NB, Williams A (2008) Transformations of electrosensory encoding associated with an adaptive filter. J Neurosci 28:1598–1612.

Searl T, Prior C, Marshall IG (1991) Acetylcholine recycling and release at rat motor nerve terminals studied using (-)-vesamicol and troxpyrrolium. J Physiol (Lond) 444:99–116.

Shore SE (2005) Multisensory integration in the dorsal cochlear nucleus: unit responses to acoustic and trigeminal ganglion stimulation. European Journal of Neuroscience 21:3334–3348.

Shore SE, Zhou J (2006) Somatosensory influence on the cochlear nucleus and beyond. Hear Res 216-217:90–99.

Smith SM, Zorec R, McBurney RN (1989) Conductance states activated by glycine and GABA in rat cultured spinal neurones. J Membr Biol 108:45–52.

Smith TC, Jahr CE (2002) Self-inhibition of olfactory bulb neurons. Nat Neurosci 5:760–766.

Soto D, Coombs ID, Kelly L, Farrant M, Cull-Candy SG (2007) Stargazin attenuates intracellular polyamine block of calcium-permeable AMPA receptors. Nat Neurosci 10:1260–1267.

Spirou GA, Young ED (1991) Organization of dorsal cochlear nucleus type IV unit response maps and their relationship to activation by bandlimited noise. J Neurophysiol 66:1750–1768.

Stuart G (1999) Voltage-activated sodium channels amplify inhibition in neocortical pyramidal neurons. Nat Neurosci 2:144–150.

Stuart G, Sakmann B (1995) Amplification of EPSPs by axosomatic sodium channels in neocortical pyramidal neurons. Neuron 15:1065–1076.

Supplisson S, Roux MJ (2002) Why glycine transporters have different stoichiometries. FEBS Lett 529:93–101.

Szapiro G, Barbour B (2007) Multiple climbing fibers signal to molecular layer interneurons exclusively via glutamate spillover. Nat Neurosci 10:735–742.

Trigo FF, Sakaba T, Ogden D, Marty A (2012) Readily releasable pool of synaptic vesicles measured at single synaptic contacts. Proc Natl Acad Sci USA 109:18138–18143.

Tzounopoulos T, Kim Y, Oertel D, Trussell LO (2004) Cell-specific, spike timing-dependent plasticities in the dorsal cochlear nucleus. Nat Neurosci 7:719–725.

Tzounopoulos T, Rubio ME, Keen JE, Trussell LO (2007) Coactivation of pre- and postsynaptic signaling mechanisms determines cell-specific spike-timing-dependent plasticity. Neuron 54:291–301.

Van der Kloot W (2003) Loading and recycling of synaptic vesicles in the Torpedo electric organ and the vertebrate neuromuscular junction. Prog Neurobiol 71:269–303.

Vervaeke K, Lorincz A, Gleeson P, Farinella M, Nusser Z, Silver RA (2010) Rapid desynchronization of an electrically coupled interneuron network with sparse excitatory synaptic input. Neuron 67:435–451.

Vervaeke K, Lorincz A, Nusser Z, Silver RA (2012) Gap junctions compensate for sublinear dendritic integration in an inhibitory network. Science 335:1624–1628.

Vincent P, Marty A (1996) Fluctuations of inhibitory postsynaptic currents in Purkinje cells from rat cerebellar slices. J Physiol (Lond) 494 (Pt 1):183–199.

Wang H, Brozoski TJ, Caspary DM (2011) Inhibitory neurotransmission in animal models of tinnitus: maladaptive plasticity. Hear Res 279:111–117.

Wang L, Jiang H, Brigande JV (2012) Gene transfer to the developing mouse inner ear by in vivo electroporation. J Vis Exp.

Wei J, Wu J-Y (2008) Post-translational regulation of L-glutamic acid decarboxylase in the brain. Neurochem Res 33:1459–1465.

Wenthold RJ, Huie D, Altschuler RA, Reeks KA (1987) Glycine immunoreactivity localized in the cochlear nucleus and superior olivary complex. Neuroscience 22:897–912.

Whittaker VP (1987) Cholinergic synaptic vesicles from the electromotor nerve terminals of Torpedo. Composition and life cycle. Ann N Y Acad Sci 493:77–91.

Williams J (1997) How does a vesicle know it is full? Neuron 18:683–686.

Wojcik SM, Katsurabayashi S, Guillemin I, Friauf E, Rosenmund C, Brose N, Rhee J-S (2006) A shared vesicular carrier allows synaptic corelease of GABA and glycine. Neuron 50:575–587.

Wouterlood FG, Mugnaini E, Osen KK, Dahl AL (1984) Stellate neurons in rat dorsal cochlear nucleus studies with combined Golgi impregnation and electron microscopy: synaptic connections and mutual coupling by gap junctions. J Neurocytol 13:639–664.

Xu T-X, Gong N, Xu T-L (2005) Inhibitors of GlyT1 and GlyT2 differentially modulate inhibitory transmission. Neuroreport 16:1227–1231.

Yamada-Hanff J, Bean BP (2013) Persistent sodium current drives conditional pacemaking in CA1 pyramidal neurons under muscarinic stimulation. J Neurosci 33:15011–15021.

Young ED, Nelken I, Conley RA (1995) Somatosensory effects on neurons in dorsal cochlear nucleus. J Neurophysiol 73:743–765.

Zafra F, Aragón C, Olivares L, Danbolt NC, Giménez C, Storm-Mathisen J (1995) Glycine transporters are differentially expressed among CNS cells. J Neurosci 15:3952–3969.

Zeilhofer HU, Studler B, Arabadzisz D, Schweizer C, Ahmadi S, Layh B, Bösl MR, Fritschy J-M (2005) Glycinergic neurons expressing enhanced green fluorescent protein in bacterial artificial chromosome transgenic mice. J Comp Neurol 482:123–141.

Zhang S, Oertel D (1993) Cartwheel and superficial stellate cells of the dorsal cochlear nucleus of mice: intracellular recordings in slices. J Neurophysiol 69:1384–1397.

Zhang S, Oertel D (1994) Neuronal circuits associated with the output of the dorsal cochlear nucleus through fusiform cells. J Neurophysiol 71:914–930.

Zhao S, Ting JT, Atallah HE, Qiu L, Tan J, Gloss B, Augustine GJ, Deisseroth K, Luo M, Graybiel AM, Feng G (2011) Cell type–specific channelrhodopsin-2 transgenic mice for optogenetic dissection of neural circuitry function. Nat Methods 8:745–752.